Erosion and Transport of Sediments and Pollutants in the Benthic Boundary Layer on the San Pedro Shelf, Southern California

by

Herman A. Karl
David A. Cacchione
David E. Drake

United States Department of Interior
Geological Survey
OPEN-FILE REPORT 80-386

TABLE OF CONTENTS

TABLE ES-I

Summary of processes active during experimental period (SPEX-1) at Geoprobe sites

	Typical period	Typical max. speed	Remarks
Surface waves (swell)	12-14 sec.	10-20 cm/s	Wave stress forms ripples on inner shelf. Occur in packets of 1-3 days duration during fair weather.
Internal waves	15 min - 8 hrs.	10 cm/s	Present throughout experiment. Effect important in combination with tide.
Tides	12, 24 hr.	15 cm/s	Low to moderate stress.
Mean Flow	-	1-3 cm/s	Southeastward and offshore transport of bottom water during spring 1978.

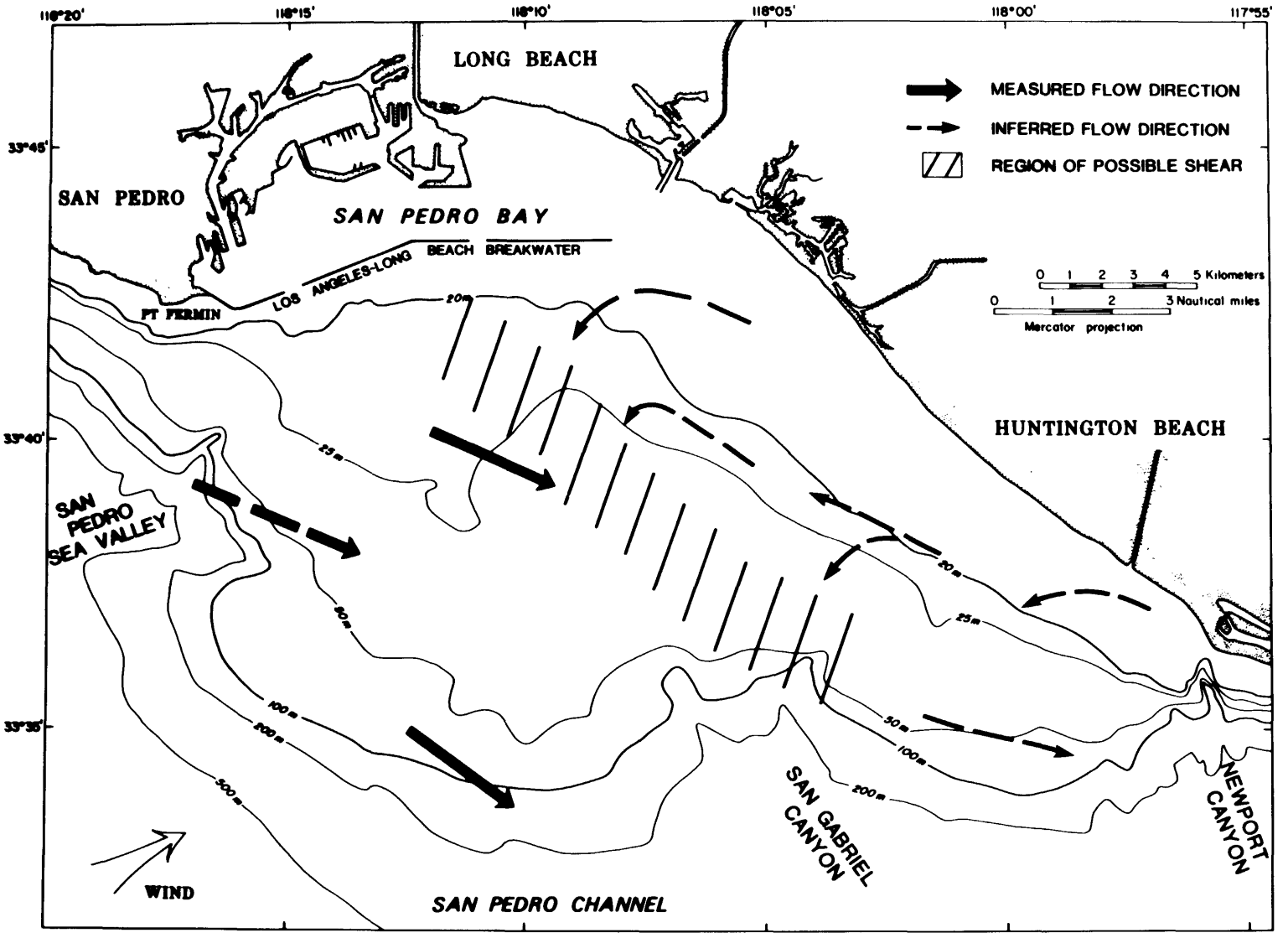

Figure ES-1. Near-bottom current directions during an upwelling event. Length of arrows does not indicate relative current speed.

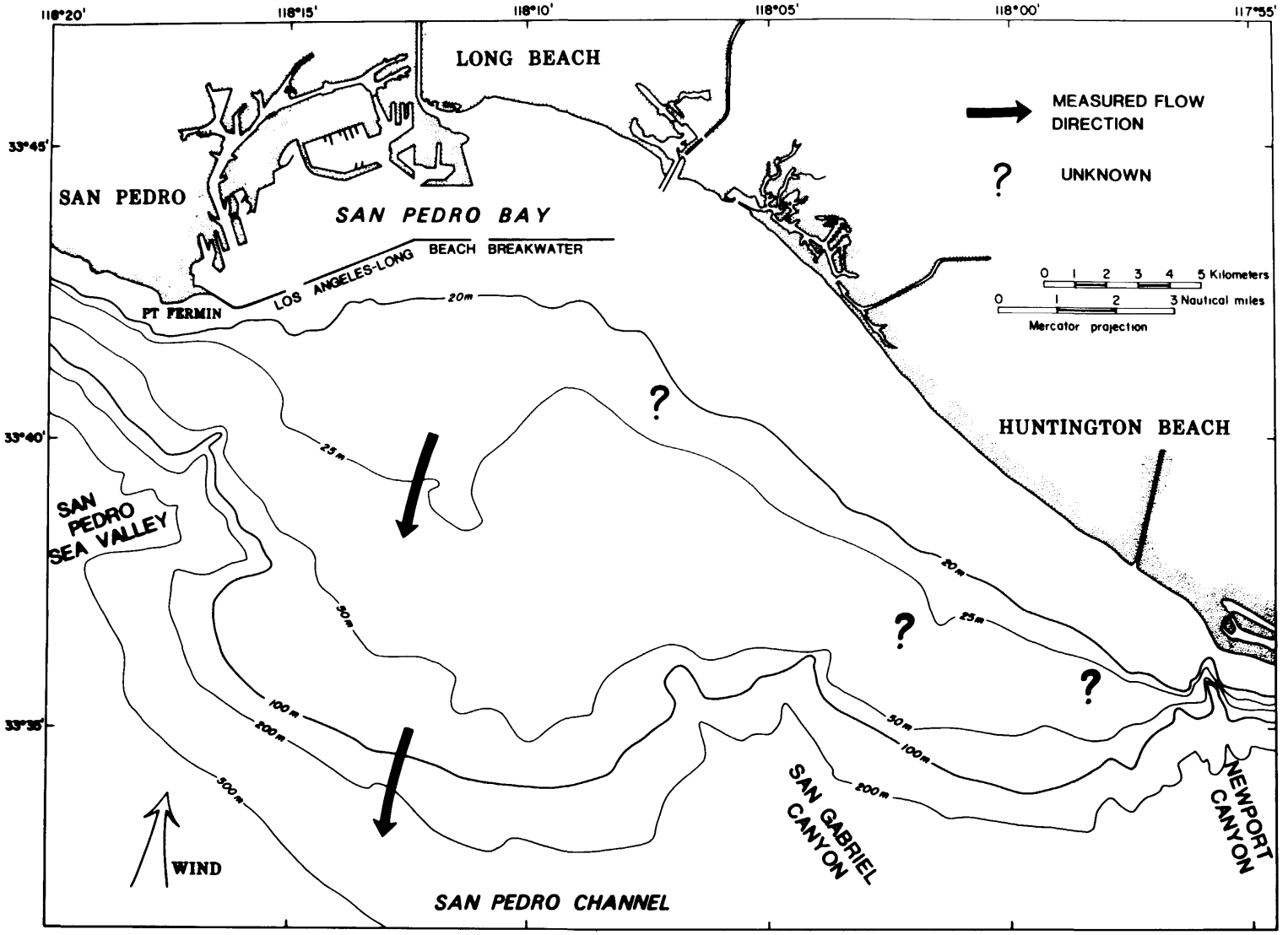

Figure ES-2. Near-bottom current directions during a non-upwelling situation. Length of arrows does not indicate relative current speed.

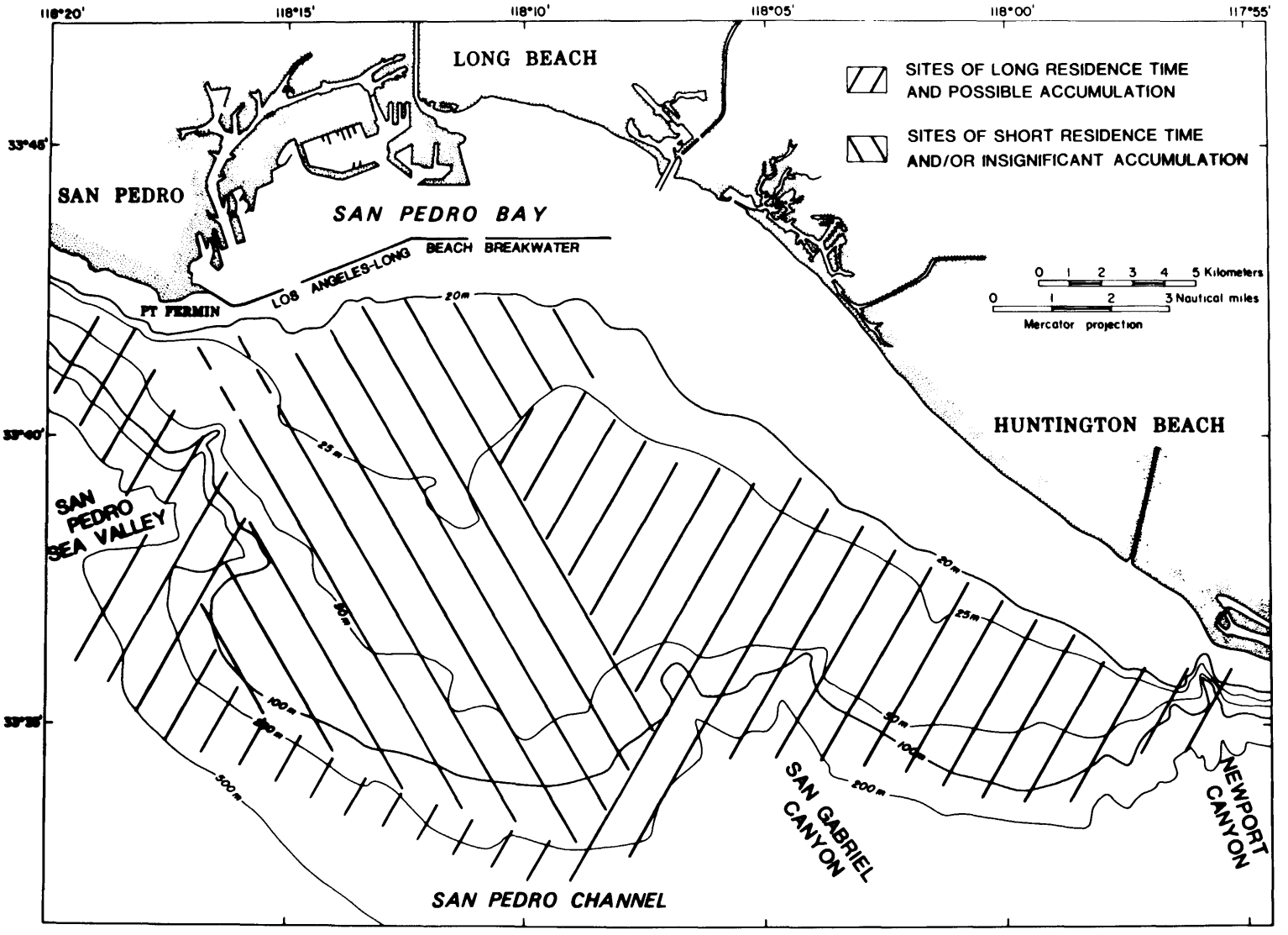

Figure ES-3. Areas where pollutants will accumulate.

Erosion and transport of sediments and pollutants in the benthic boundary layer on the San Pedro shelf, southern California

by

H. A. Karl, D. A. Cacchione, and D. E. Drake

INTRODUCTION

This report describes the results of the San Pedro Shelf Experiment (SPEX-1), a research project funded jointly by Bureau of Land Management-U.S. Geological Survey under Memorandum of Understanding AA551-MU-8-10. The proposal entitled "Erosion and transport of sediments and pollutants in the benthic boundary layer on the San Pedro shelf, southern California "submitted by the principal investigators details the specific terms and objectives of this research investigation. The basic goals of the experiment are to identify: 1) transport vectors of pollutants and sediments in the benthic boundary layer (BBL) at specific sites on the San Pedro continental shelf; 2) the major transport mechanisms operating in this region and to evaluate their relative importance; 3) areas of excessive erosion or deposition that could affect sea-floor pipelines or drilling structures constructed on tracks developed in Lease Sale No. 35.

Data necessary to accomplish these objectives were collected during two cruises in Spring, 1978. The first cruise, 17-29 April, used the USGS research vessel SEA SOUNDER to deploy instruments and to conduct specific site and regional hydrographic, geologic and geophysical surveys. The second cruise, 5-9 June, used the University of Southern California's research vessel VELERO IV to retrieve moored and bottom instruments, and to collect some limited regional transmission and suspended sediment data. Figure 1 shows the study area; Figure 2 shows station locations, and Figure 3 shows geophysical survey lines.

STUDY AREA AND PREVIOUS WORK

The continental shelf off southern California consists of a series of littoral transport cells bounded on their downdrift ends by submarine canyons (Emery, 1960; Inman and Frautschy, 1966). San Pedro Bay, the region of study, encompasses the cell which begins just east of Palos Verdes Peninsula and terminates where Newport Submarine Canyon incises the shelf at the east end (Fig. 1).

San Pedro shelf is a broad, gently sloping platform extending, at its widest point, about 20 km from shore to the shelf break (75-90 m isobath) and narrowing to about 3 km at its east and west boundaries. In addition to Newport Canyon, which heads close to shore, two canyons, San Pedro Sea Valley and San Gabriel Canyon, indent the outer portion of the shelf.

Most previous studies of San Pedro Bay and environs emphasize descriptions of geology, surficial sediment distribution and the general circulation patterns of surface waters (Moore, 1951, 1954; Emery, 1960; Bunnell, 1969; Pirie et al., 1975). A few investigators described the hydrodynamic climate in more detail and speculated on processes and routes of sediment transport (Horrer, 1950; O'Brien, 1950; Caldwell, 1956; Vernon, 1966; Felix and Gorsline, 1971; Gorsline and Grant, 1972; Hendrichs, 1976a,b). A BLM base-line study of the southern California borderland included portions of San Pedro shelf (Fischer et al., 1976; Douglas et al., 1979). Recently, Karl (1976) completed a 4 year study of sediment dynamics on southern California shelves with particular focus on San Pedro shelf. Karl (1976; in press a,b) found evidence of significant sediment transport both at the bottom and throughout the water column.

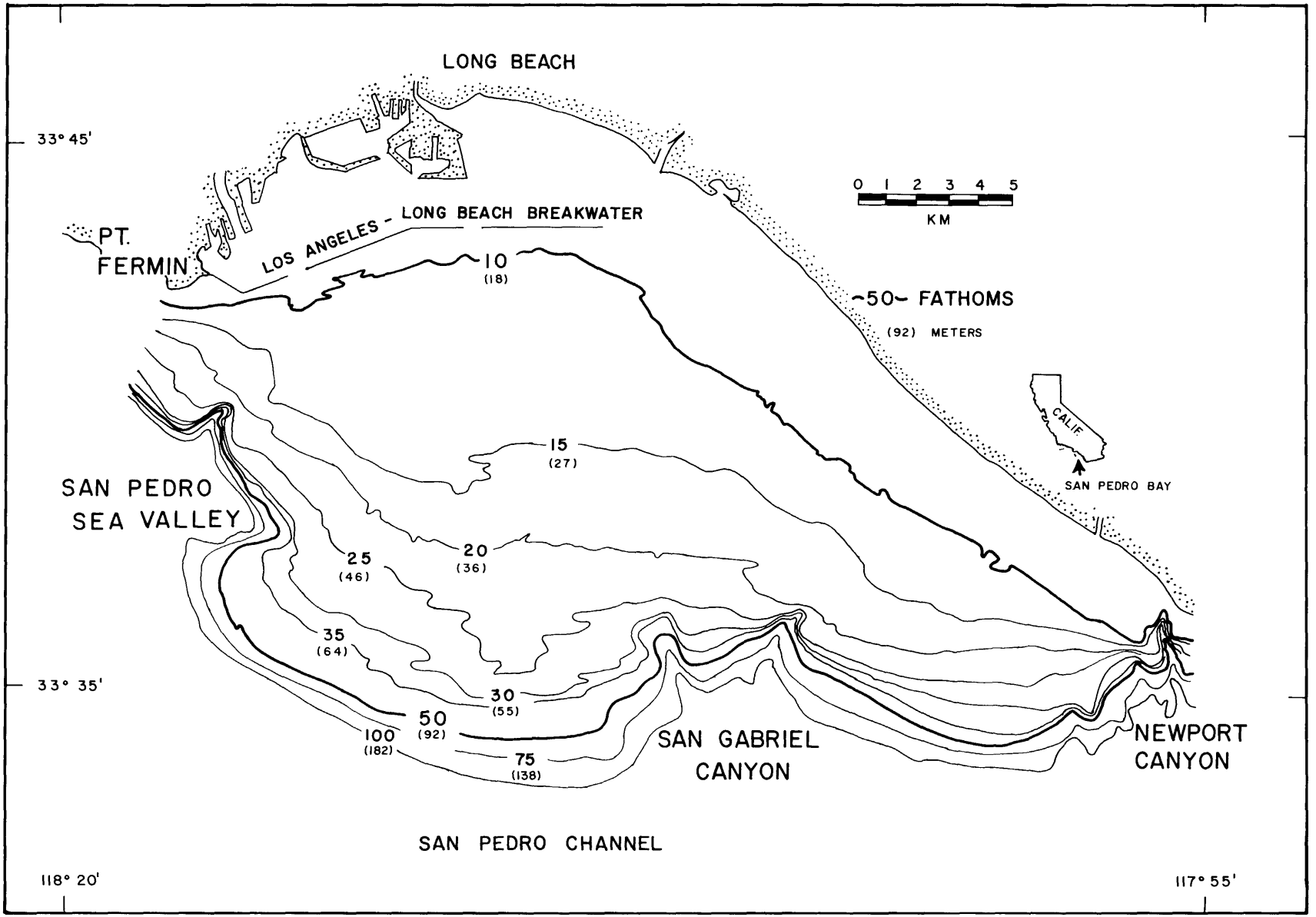

Figure 1. General bathymetry and geography of the study area, San Pedro shelf.

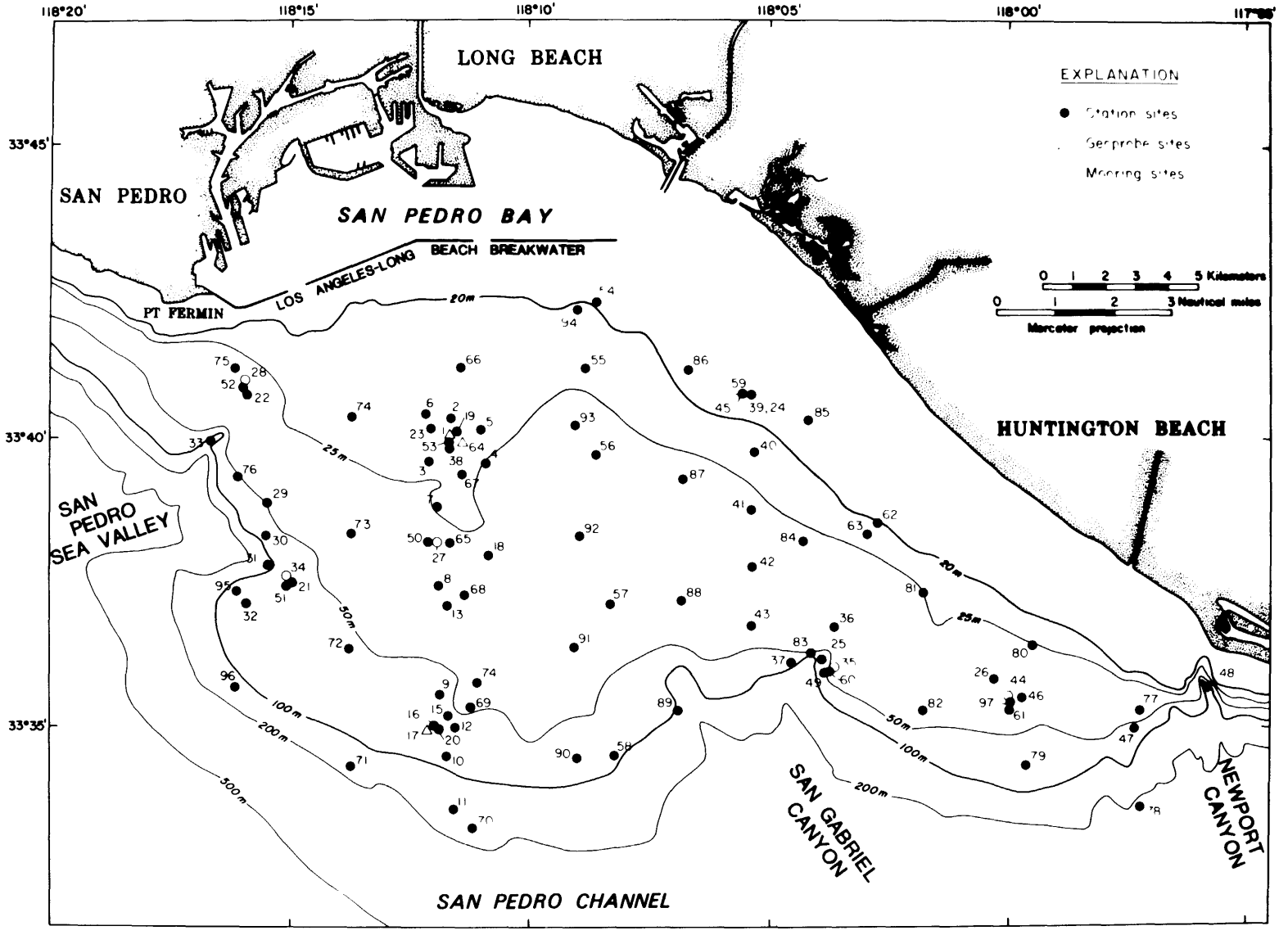

Figure 2. Station locations.

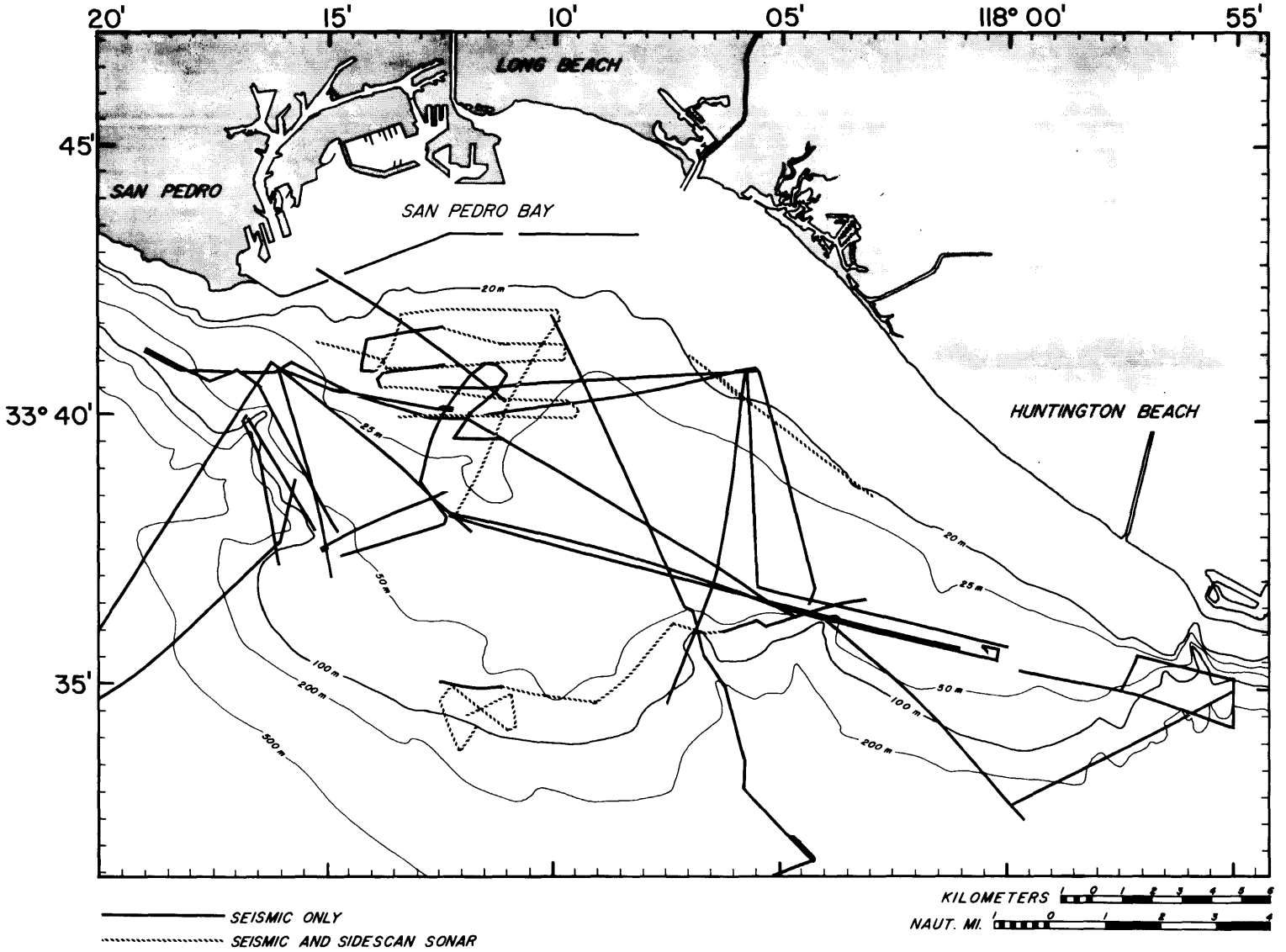

Figure 3. Geophysical survey tracks.

METHODS

In this experimental program, we undertook regional geologic sampling, geophysical surveys and oceanographic measurements to establish the spatial variability of the sea-floor and near-bottom water properties of San Pedro shelf. Time series data derived from moored instruments illustrated the temporal variability of several physical oceanographic parameters and processes, and water borne sediments. In addition to regional sampling during the April cruise, a single station was occupied for 24 hours during which time discrete measurements of several parameters were made at hourly intervals. Table I summarizes the operations performed at each regional station and Table II lists each operation performed during each hour at the 24-hour anchor station.

Substrate

An NEL box corer and Soutar Van Veen were used to collect samples of the substrate in order to characterize sediment size distributions at each of the moored instrument sites. Size distributions were determined in the laboratory by standard pipette techniques for the fine (<62 μm) fraction and by settling tube techniques for the coarse ($\geq$ 62 μm) fractions.

A TV/70 mm camera system was used to identify and map the distribution of small-scale bedforms and other features on the sea-floor. The TV monitor onboard enabled real-time viewing of the sea-floor as the ship drifted for several minutes over a station. TV images and verbal descriptions made by the viewing scientists were recorded on video tape. The 70 mm camera could be triggered remotely to photograph features of particular interest viewed on the TV monitor. The 70 mm film was developed onboard ship. Printed enlargements have been made to analyze bedforms and other features.

Geophysical data consisted of: 1) bathymetric profiling using a 12 kHz system; 2) high-resolution sub-bottom profiling using 800 Hz and 3.5 kHz systems; and 3) side-scan sonar profiling.

Water Column

A profiling CTD was used to obtain a nearly continuous vertical profile of temperature and conductivity. The CTD data were displayed in analog form graphically on board ship, and recorded digitally on magnetic tape. The digital data were corrected for instrument calibration and replotted as depth profiles of temperature, salinity, and density (sigma $_t$). Turbidity of the water column was measured with a profiling light-beam transmissometer; increasing percent transmission indicates decreasing turbidity (less suspended matter in the water column). Absolute concentrations of total suspended matter (TSM) was determined by conventional methods. Water at the surface was sampled with a bucket; water 1 m above bottom was sampled using a 5-liter Niskin bottle modified to close when a weighted line contacted the seabed, and 5-liter Van Dorn bottles were used to sample water at intervals between the surface and the bottom. Sampling intervals were chosen by inspecting the transmission record for that station. At sea, aliquots of water from these samples were passed through preweighed Nuclepore* filters (nominal pore size, 0.4 μm); the filters were rinsed with distilled water and placed in covered petri dishes. Onshore the filters were dried and weighed, and the concentration of TSM calculated as milligrams of suspensate per liter of seawater. In addition, a portion of each filter from two transects was combusted to determine the percent non-combustible residue and the percent organic matter. At selected anchor stations a profiling current meter was used to measure current speed and direction.

TABLE I

Operations at each station

Station Number	Operations
1	1D,3,4,5,6,7,8,9
2-11	3,4,5
12	6,7
13	3,4,5,6
14	6
15	4,6
16	6
17	1D,3,4,5,7,8
18-26	3,4,5
27-28	2D,3,4,5,7
29-33	3,4,5,6
34	2D
35	2D,3,4,5,6
36	4,5,6
37	3,4,5,6
38	3,4,5,7
39-43	6
44	2D
45	2D,3,4,5,8
46	3,4,5,6,7,8
47	3,4,5,6
48	6
49-51	3,4,5,8
52	3,4,5,6,8
53	See table 2, also 1R
54-62	3,4,5,6
63	6
64	1D
65	2R
66-96	3,4,5

Explanation:

1D	GEOPROBE Deployment
1R	GEOPROBE Recovery
2D	Current Meter Mooring Deployment
2R	Current Meter Mooring Recovery
3	Water Sample(s)
4	Transmissometer Profile
5	CTD Profile
6	TV and Bottom Camera
7	Current Meter Profile
8	Box Core Sample
9	Soutar-Van Veen Sample

TABLE II

Operations each hour at 24 hour anchor stations

Julian Day	Time (GMT)*	Operations
114	1630	3,4,5,7
	1730	4
	1830	4,5
	1930	4
	2030	3,4,5,7
	2130	4
	2230	4,5
	2330	4
115	0030	3,4,5,7
	0130	4
	0230	4,5
	0330	4
	0430	3,4,5,7
	0530	4
	0630	3,4,5
	0730	4
	0830	3,4,5,7
	0930	4
	1030	4,5
	1130	4
	1230	3,4,5,7
	1330	4
	1430	4,5
	1530	4
	1630	3,4,5,7
	1730	6
	1830	6
	1900	1R

*Times are nominal; see station logs on file with USGS for specific time and sequence of each operation.
**Refer to Table I for explanation.

Moored instruments

Three GEOPROBES and 6 Supplemental Mooring Systems (SMS) were deployed and recovered (see Fig. 2 for locations) during the April 1979 cruise. The GEOPROBE is a tripod-mounted system of instruments (Fig. 4); it is described in detail by Cacchione and Drake (1979). A SMS (Fig. 5) consists of a torsionally-rigid spar buoy string with a Davis-Weller current meter (VMCM) (Davis and Weller, preprint) on each mooring and an Oregon State University L.E.D. transmissometer (Bartz et al., preprint) on 4 of the 5 moorings.

RESULTS

Geologic Sampling Surficial Sediment

Figure 6 illustrates the areal distribution of mean grain size of surficial sediment on San Pedro shelf. Data presented in Figure 6 are derived from an earlier study of San Pedro shelf sediment (Karl, 1976). Surficial sediment consists mainly of a thin blanket of modern very fine sands and coarse silts interrupted by patches of relict medium and coarse sands. Basically textural isopleths tend to parallel isobaths. In the area near the head of San Gabriel Canyon, however, textural isopleths deviate from this pattern and cut across isobaths.

Bedforms

Figure 7 shows the location of TV stations and bottom photographs. By matching the bedforms illustrated in Figures 8 and 9 with the respective station locations in Figure 7, it is seen that there is a progressive change seaward from well-developed ripples nearshore to biogenically reworked sediment in deeper water. The change from physically generated bedforms to biogenic structures occurs between the 40 and 45 m isobaths. Other areas of the shelf, notably the area around the shelf break, are distinguished by rocky bottom and coarse sediment. Two morphological types of ripples were observed during the cruise. One type, designated Type A (Fig. 8a,b), which occurs shallower than about 25 m on a substrate of fine and medium sand, consists of double sets of ripples of unequal wave length with orthogonally intersecting crests. The longer wave length (15-20 cm) ripples strike approximately east-west to east-southeast and the shorter wavelength (5-10 cm) ripples approximately north-south to north-northeast. Bifurcating, symmetrical ripples (eg., Fig. 8c), striking approximately east-west to east-southeast, were observed in deeper water.

Geophysical Surveys

Geophysical surveys were primarily designed to establish the morphological character of the seabed at the moored instrument sites. Consequently, line placement and density does not provide good systematic coverage of the shelf. In Figure 10 we show an example of the morphology across the shelf break in to Newport submarine canyon. Since the SPEX project deals mainly with sediment dynamics, we do not present additional geophysical records here. Detailed geophysics of the area can be found in the report by Greene et al. (in press) on the seismic structure of the southern California region.

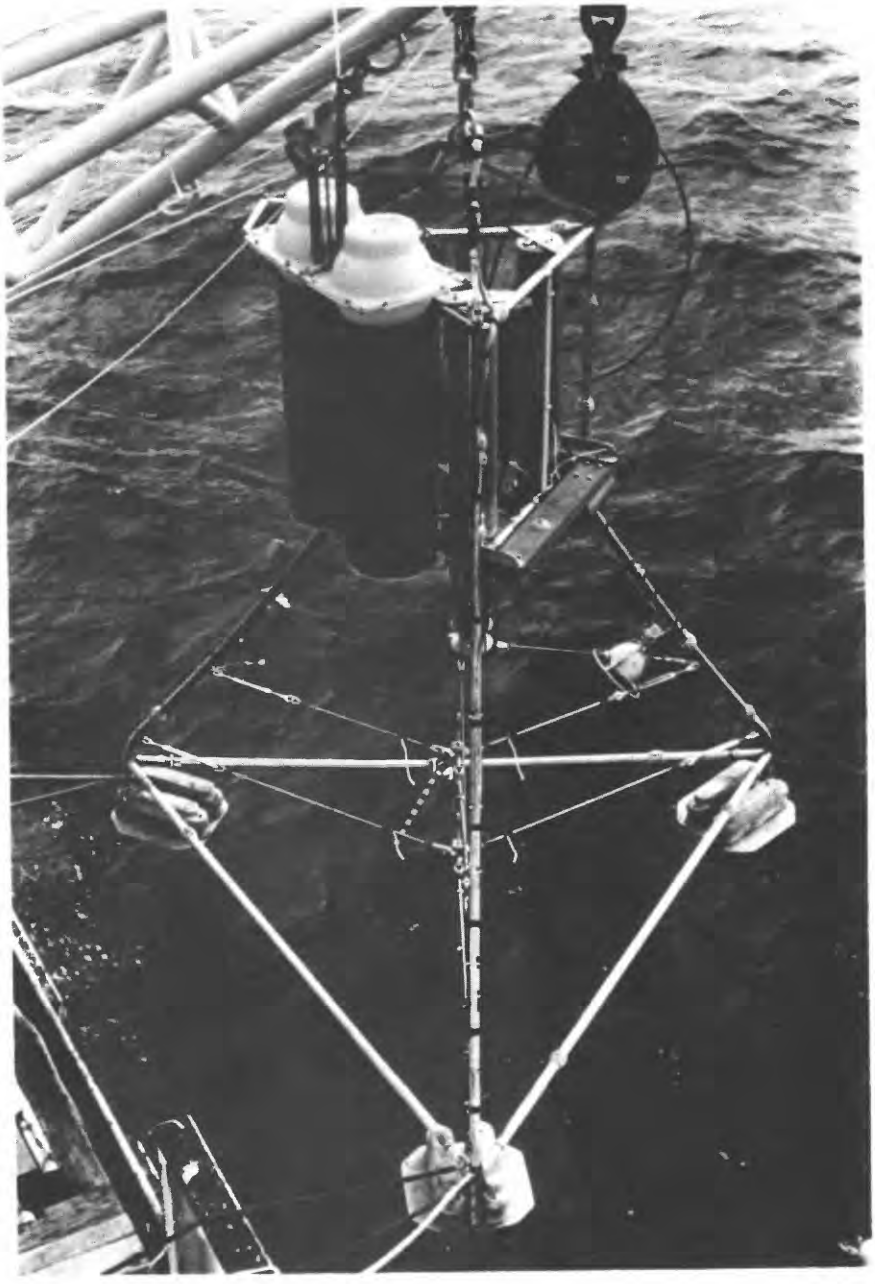

Figure 4. Geoprobe instrument system

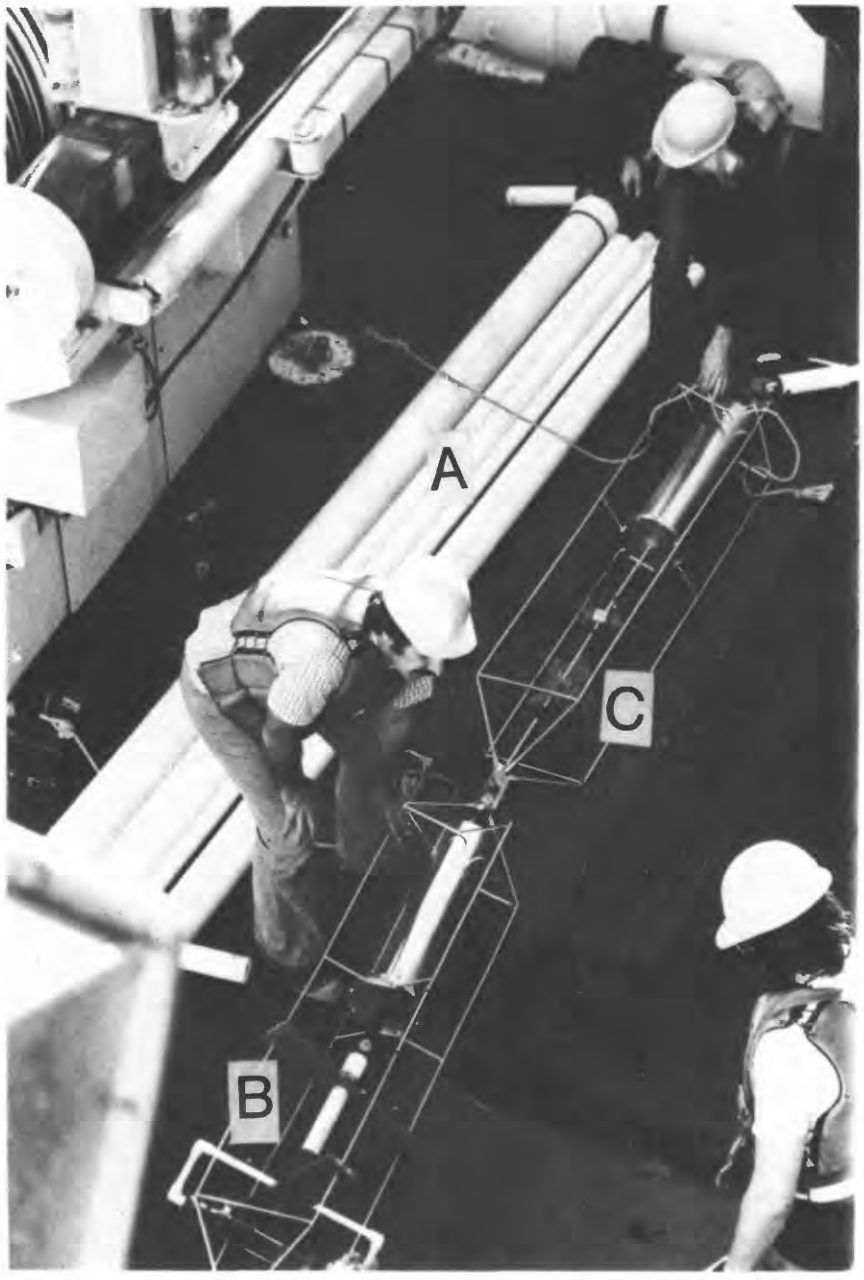

Figure 5. Components of supplemental mooring system, consisting of (A) "Shelton" spars for flotation; (B) Oregon State University L.E.D. transmissometer, and (C) Davis-Weller current meters (VMCM).

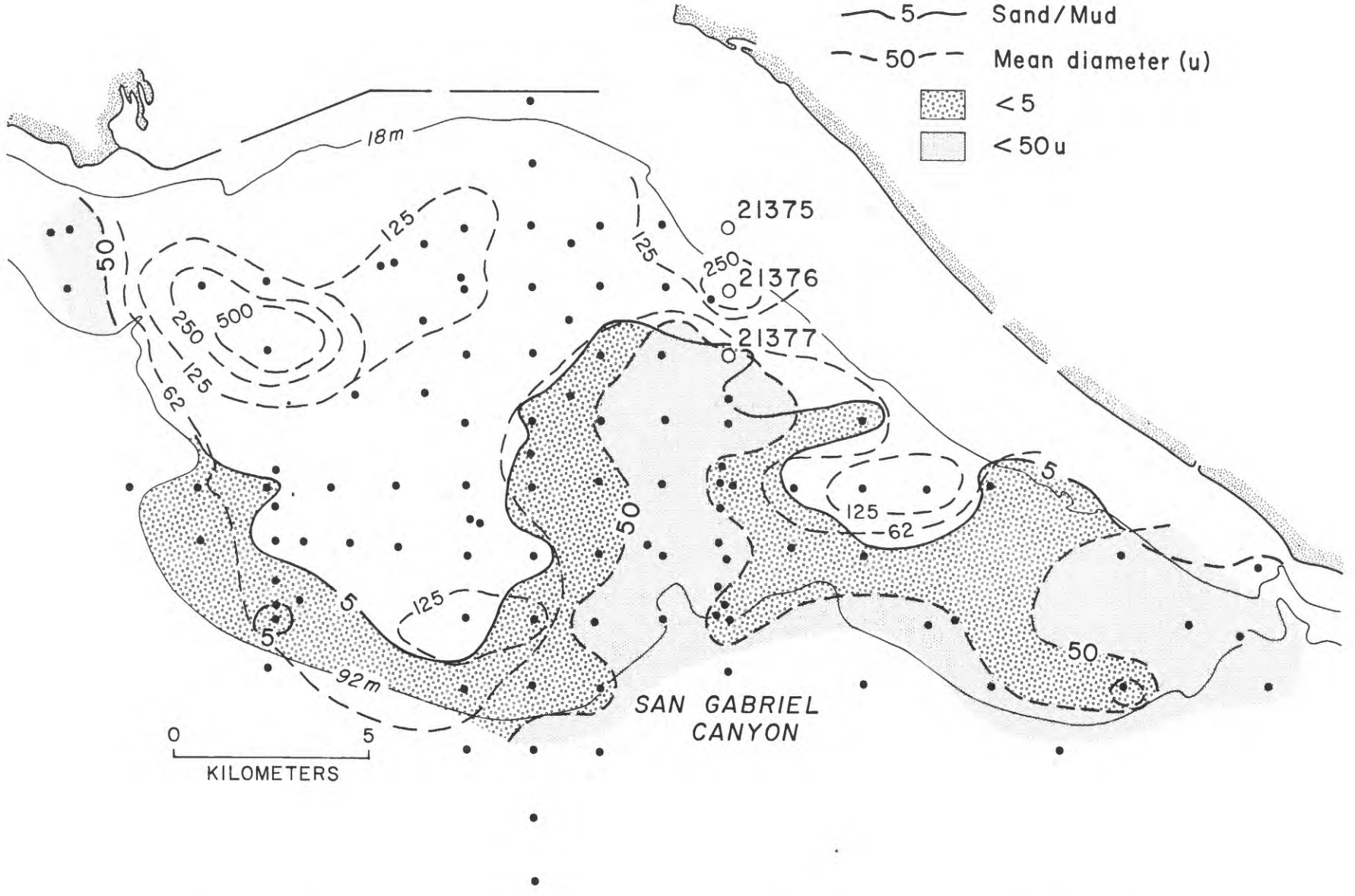

Figure 6. Areal distribution of sand-to-mud ratio and mean grain-size for samples of substrate from box cores (after Karl, in press a).

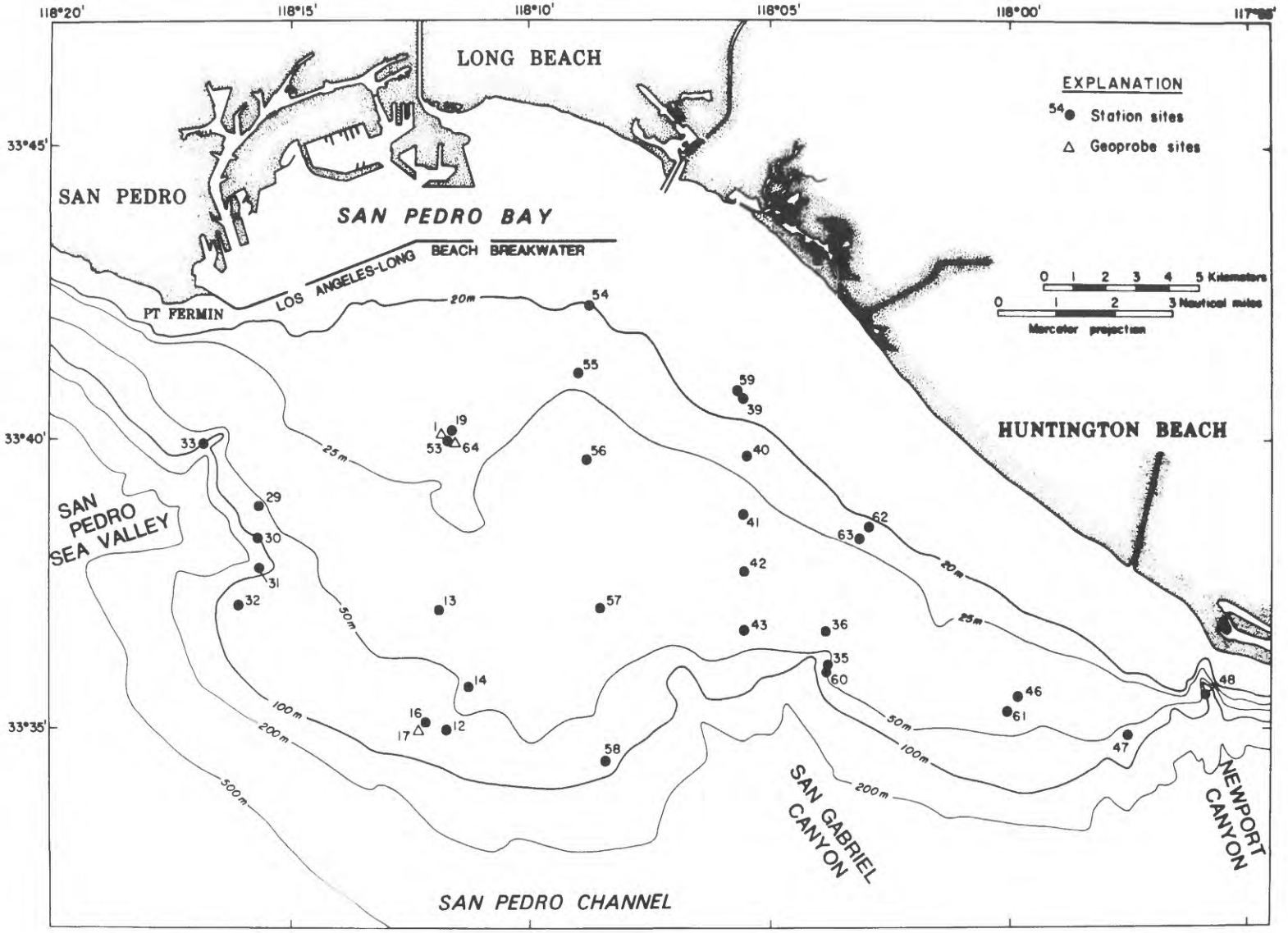

Figure 7. Large dots mark locations of TV stations and bottom photographs.

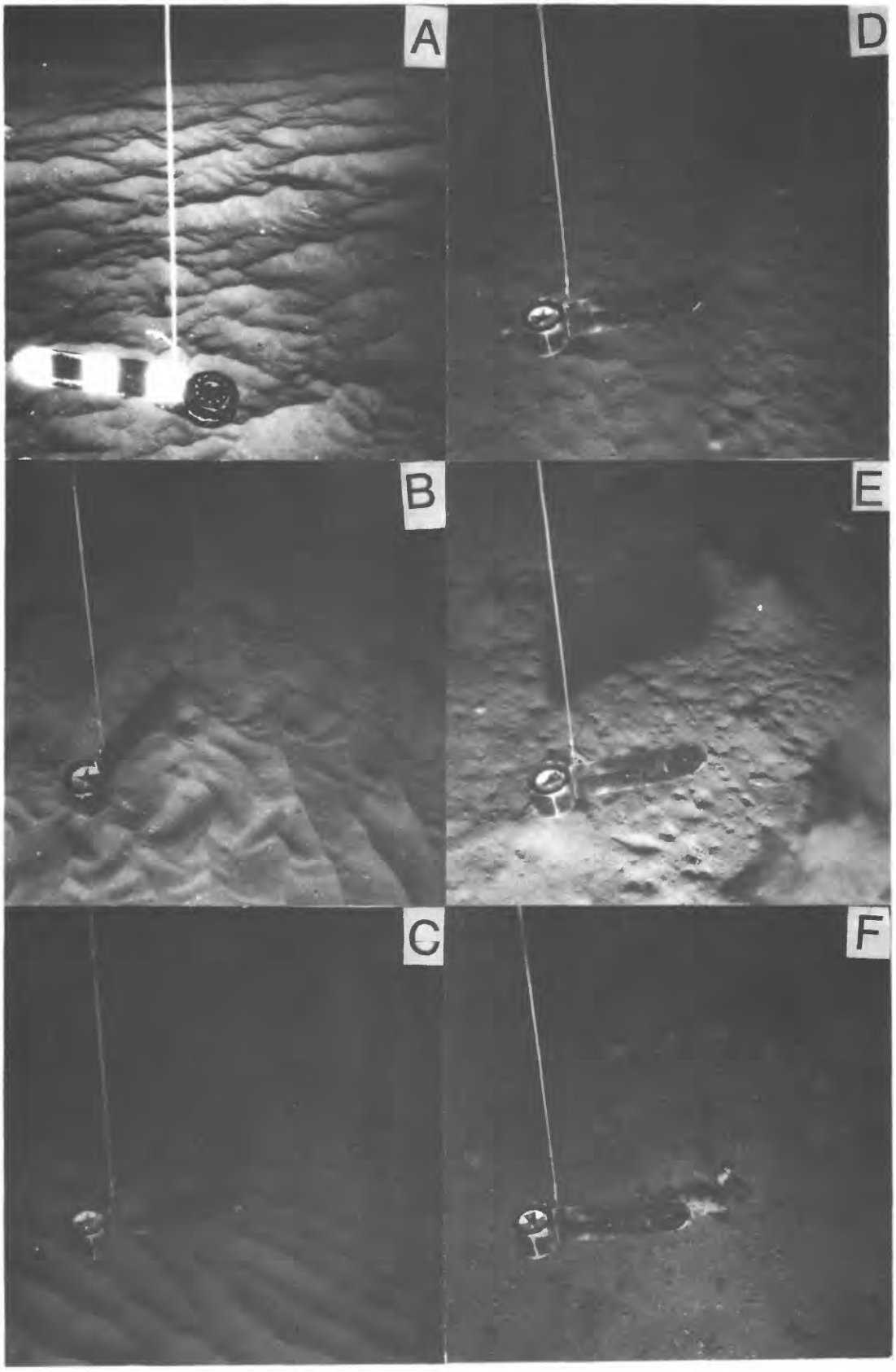

Figure 8. Representative bottom photographs illustrating the variations of bedforms and substrate on San Pedro shelf. (A = Sta 53, G1; B = Sta 53; C = Sta 56; D = Sta 57; E = Sta 60; F = Sta 58).

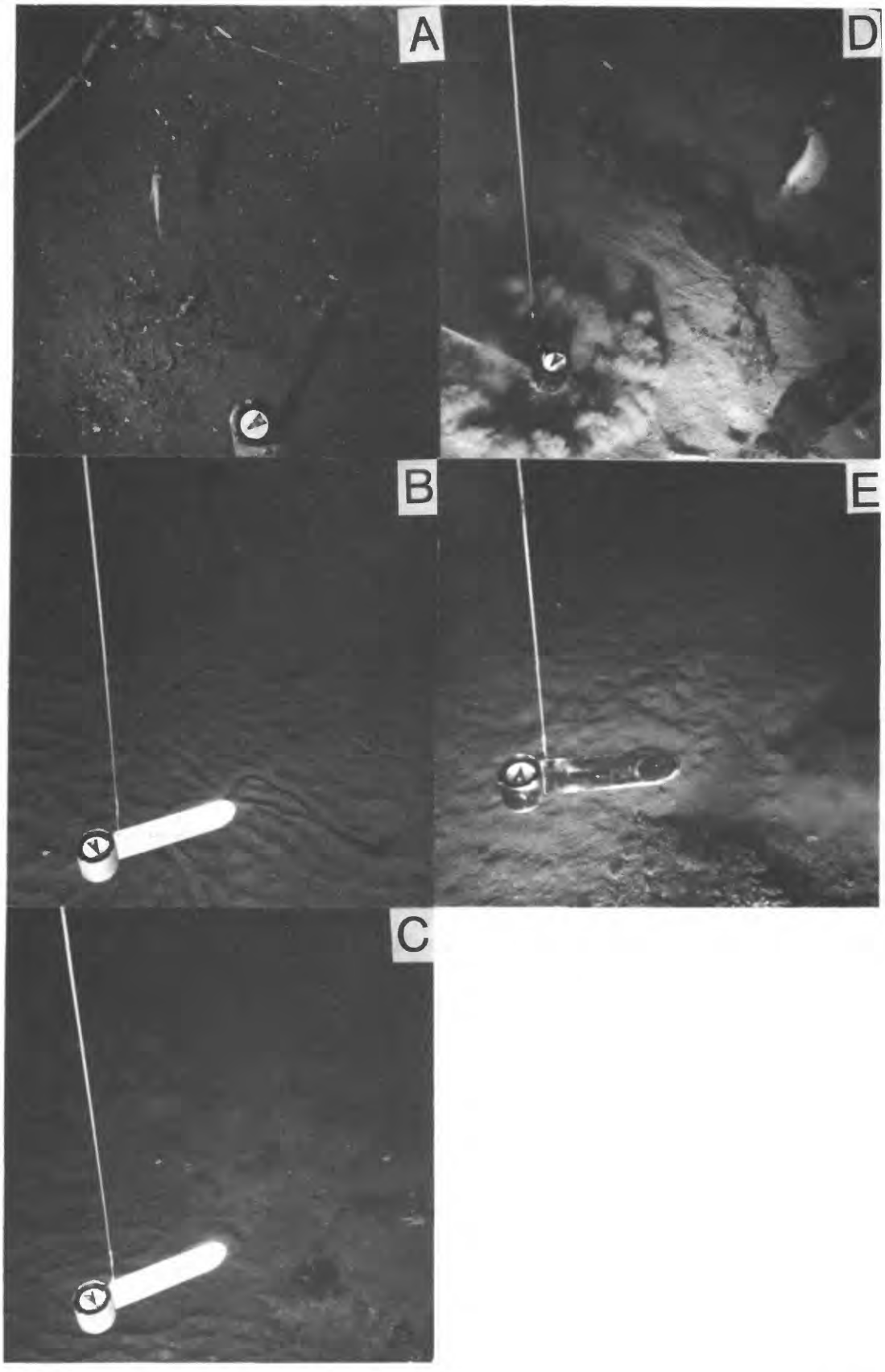

Figure 9. Representative bottom photographs illustrating the variation of bedforms and substate on San Pedro shelf. (A = G2; B = Sta 13; C = Sta 13; D = Sta 30; E = Sta 52).

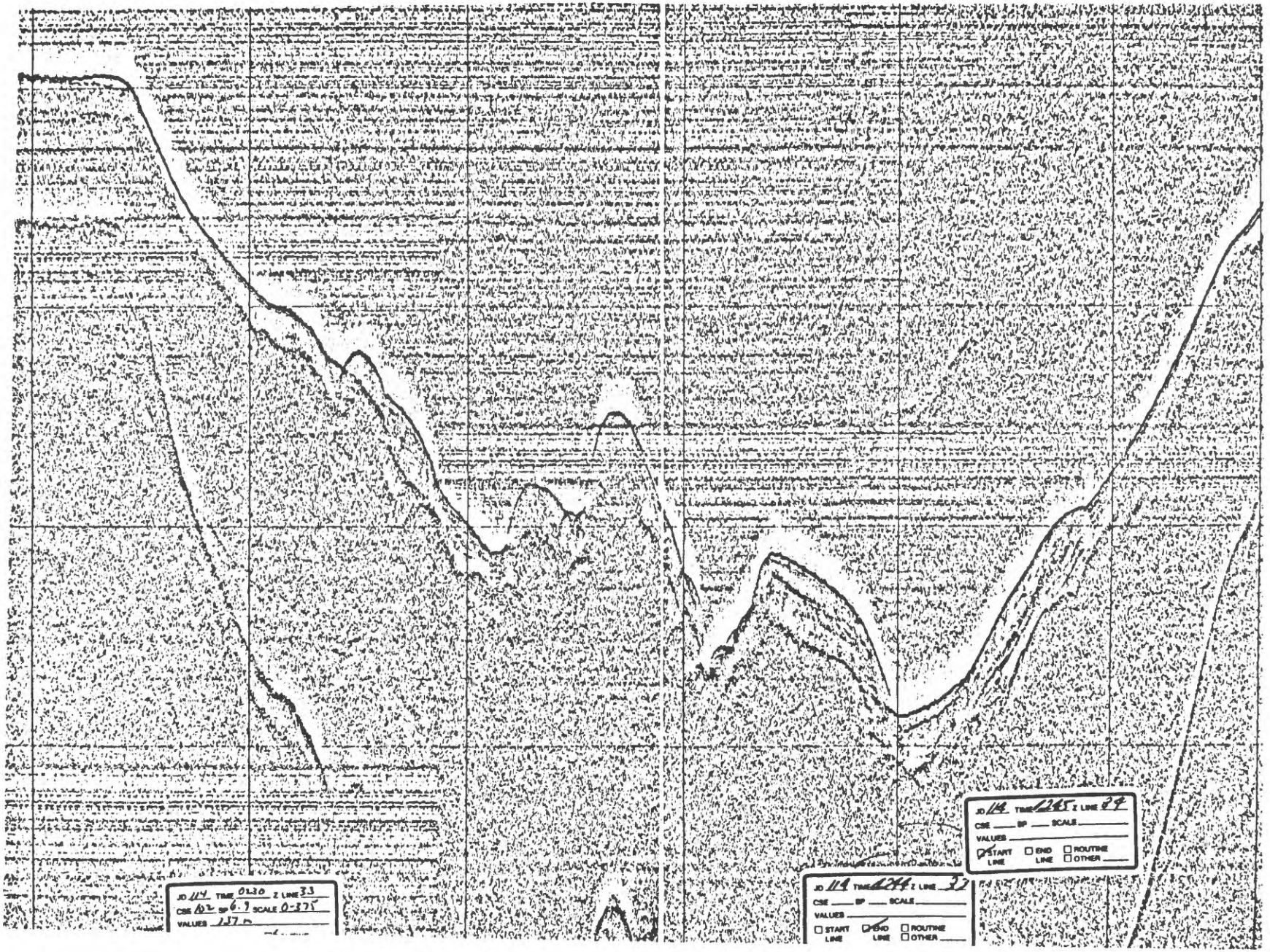

Figure10 . An example of slumping in Newport Submarine Canyon.

Water Column

Physical properties

Representative cross-shelf profiles of temperature and density are shown in Figures 11 and 12. The profiles labelled "A" shown in Figures 11, 12 and 13 were constructed from data collected at a sequence of stations occupied on April 19. These stations were reoccupied 8 days later on April 27; the changes which occurred in temperature, density and light transmission during the 8 day interval are shown in the temperature, density and light transmission during the 8 day interval are shown in the profiles labelled "B" in Figures 11, 12 and 13. These profiles show that a three-layer system, comprised of a 5-15 m thick surface mixed layer separated from a 10-20 m thick cold, dense bottom layer by the seasonal thermocline and pycnocline, had developed in shelf waters, at least during the early part of the experiment. Surface temperature recorded on 18-20 April shows that 14°C water was localized near Point Fermin on Palos Verdes Peninsula (Fig. 14). In ten days this 14°C water had breached the surface over a considerable area of shelf to the southeast (Fig. 14). Figure 16 shows in plan view the 25.75 sigma$_y$ surface.

Suspended Particulate Matter

The areal distribution of suspended particulate matter 1 m above bottom observed during April is fairly uncomplicated (Fig. 17). Basically, TSM concentration decreases seaward from nearshore values greater than 30 mg/l to values over the outer shelf of less than 1 mg/l. Near-bottom samples were not collected during June, but surface concentrations had decreased by nearly an order of magnitude over April surface values.

Representative transmission profiles also evince the distinct three-layer system present at this time (Fig. 13). Relatively turbid layers near the surface and near the bottom are separated by a less turbid mid-water zone. Percent transmission decreases and TSM increases in these turbid layers over the period 19-27 April. Microscopic examination of the filtered samples shows that the TSM increase near-bottom was due to a significant increase in silt at stations in water depths greater than or equal to 50 m. This is reflected by a 10-15% increase in near-bottom ash residue values for the 27 April transect over that of 19 April (average 19 April values are 73%; average 27 April values are 87%). Surface samples do not show any distinctive compositional change between the 19 April and 27 April transects; the average ash residue percentages are 44.6% and 43.8%, respectively.

Geoprobe Data

As mentioned above, all deployment operations with Geoprobe systems were conducted on R/V SEA SOUNDER in April, 1978. Recovery of the long term Geoprobe tripods (G1B and G2) were accomplished in June, 1978 using R/V VELERO IV. Table III summarizes the locations, experimental duration, and instrument sampling schemes for each Geoprobe. Figure 2 shows the locations of each tripod. The short turnaround of Geoprobe tripod G1A was designed to provide data on the near-bottom dynamics at relatively high basic sampling interval and burst rate. Sampling theory dictates that a sampling interval of 7.5 minutes permits examination of motions at twice that period (15 minutes) or greater. One class of motions in which we were particularly interested was relatively high frequency internal

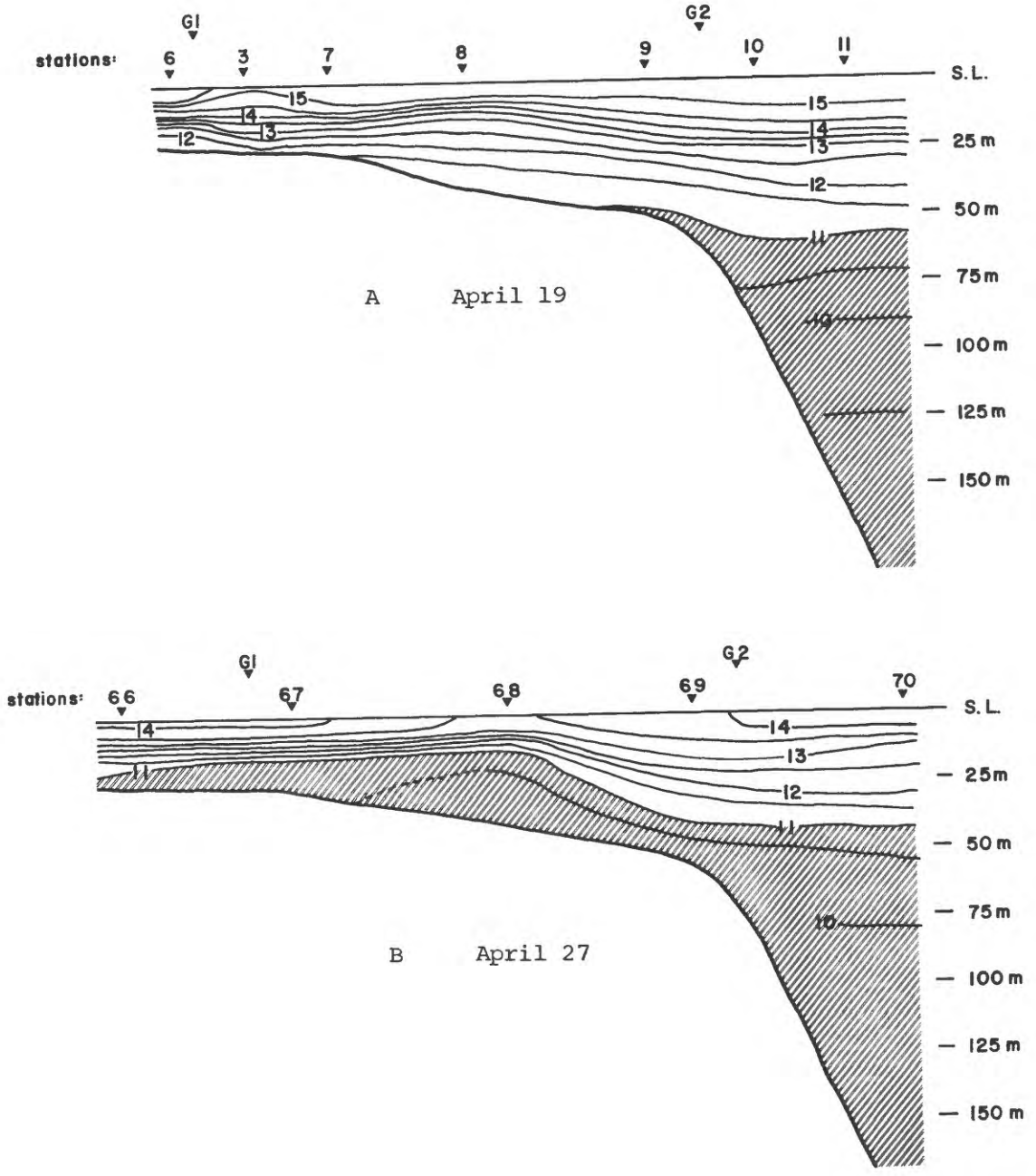

Figure 11. Cross-shelf temperature profiles through virtually coincident transects showing incursion of cold water on to shelf from 19-27 April.

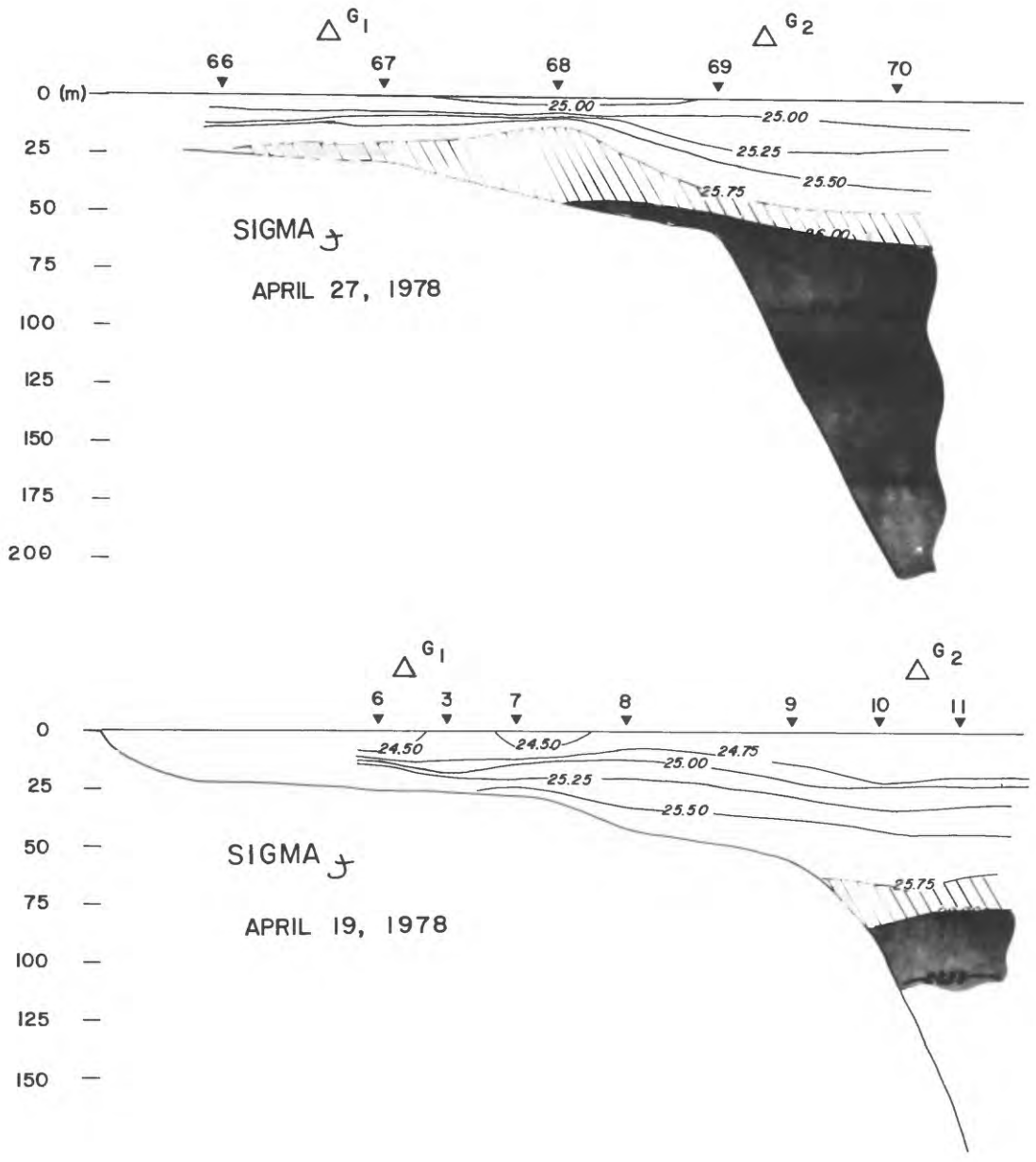

Figure 12. Cross-shelf CTD profiles through virtually coincident transects showing incursion of dense water on to the shelf from 19-27 April.

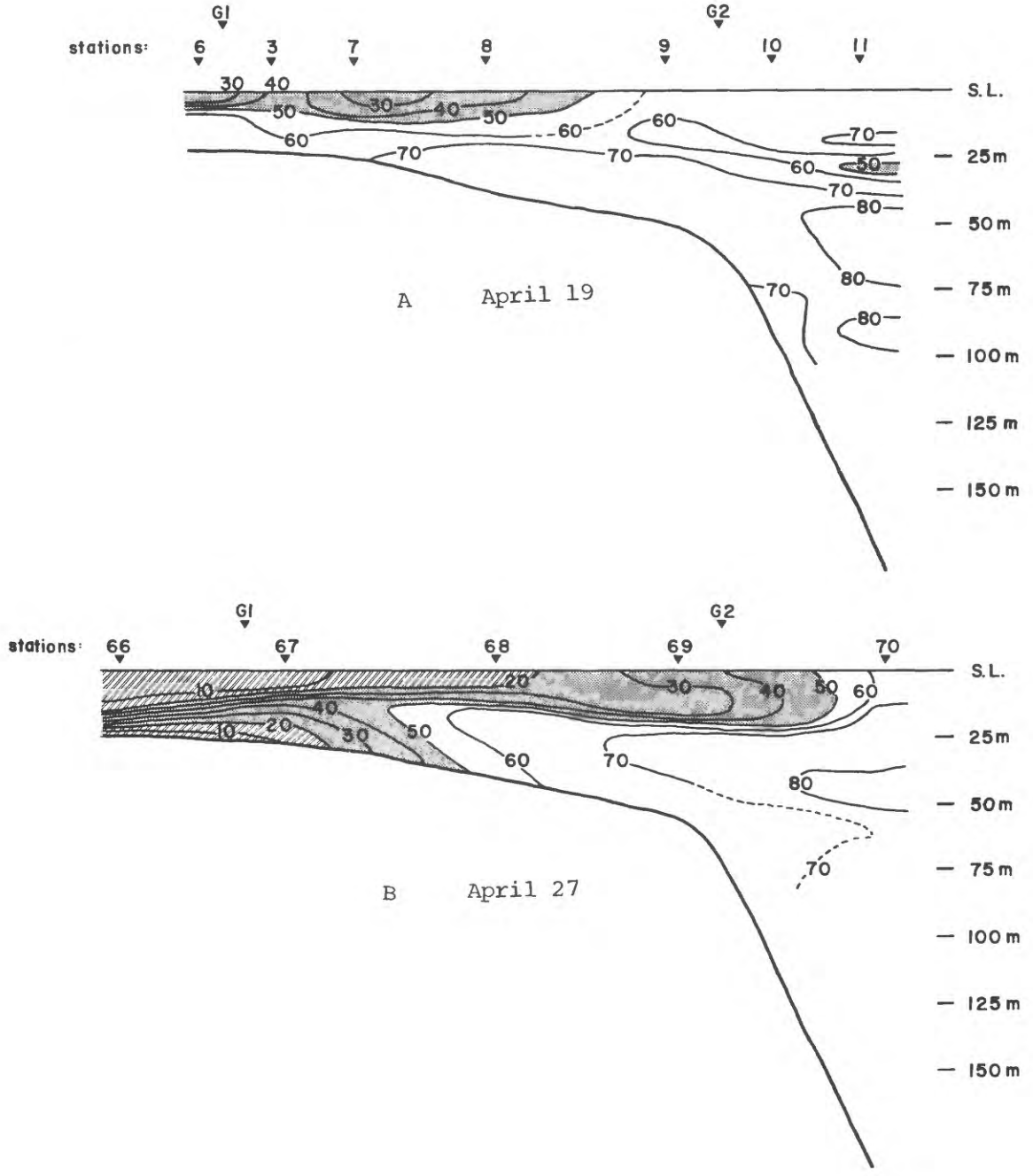

Figure 13. Cross-shelf profiles of light transmission through virtually coincident transects showing increase in near surface and near bottom turbidity from 19-27 April.

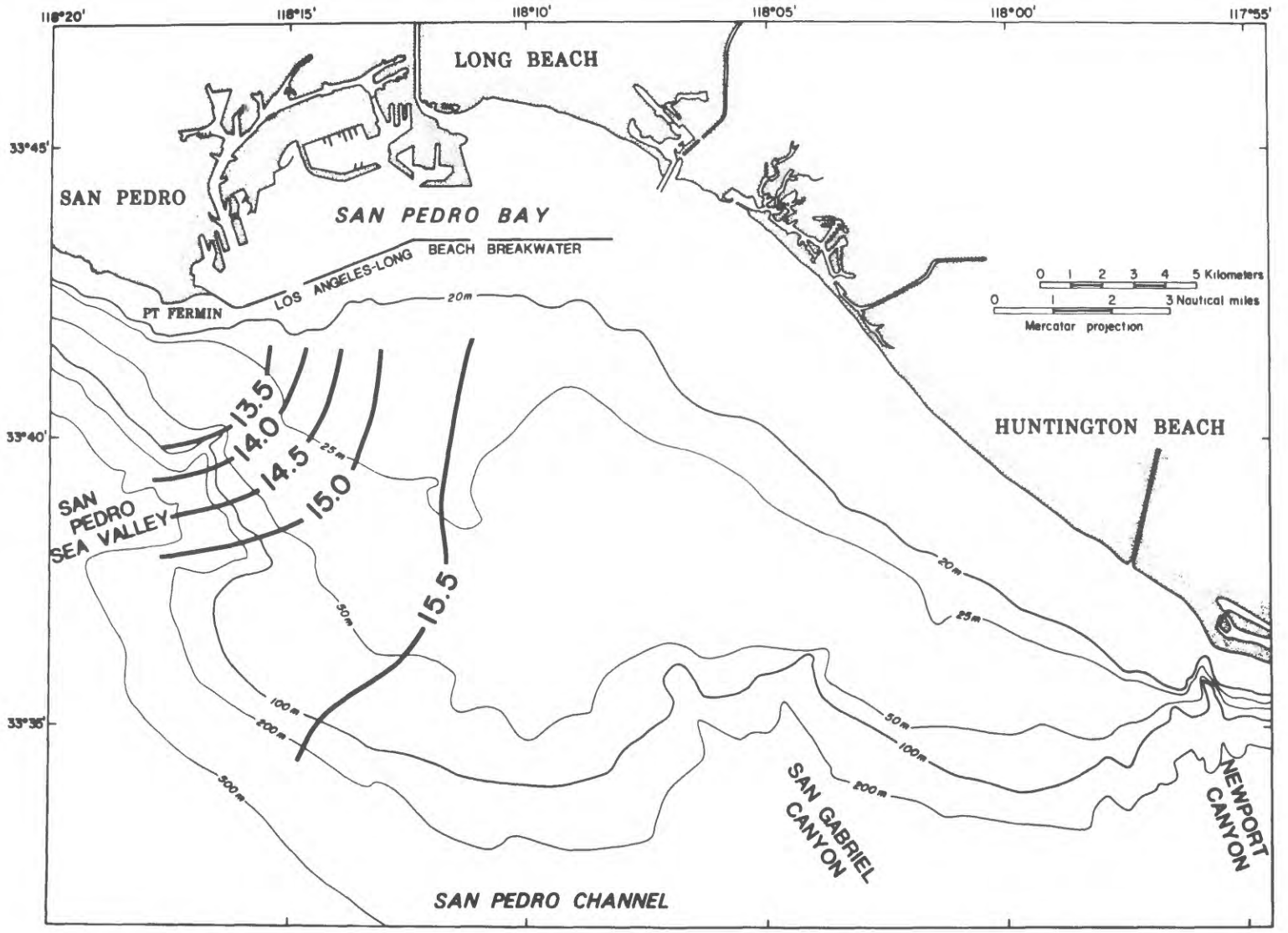

Figure 14. Surface temperature (°C) for 18-20 April, 1978 at the beginning of upwelling conditions.

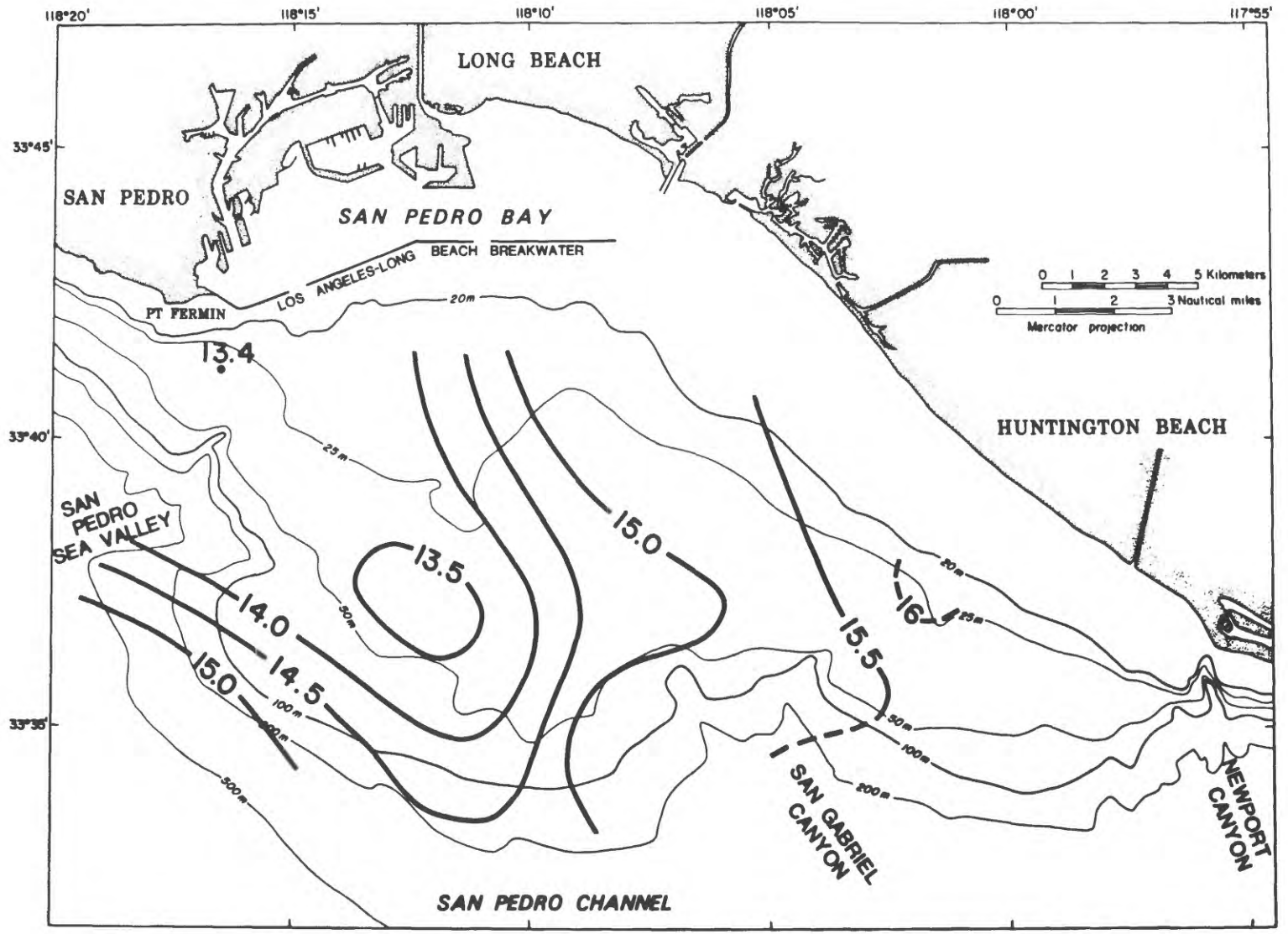

Figure 15. Surface temperature (°C) for 27-28 April, 1978.

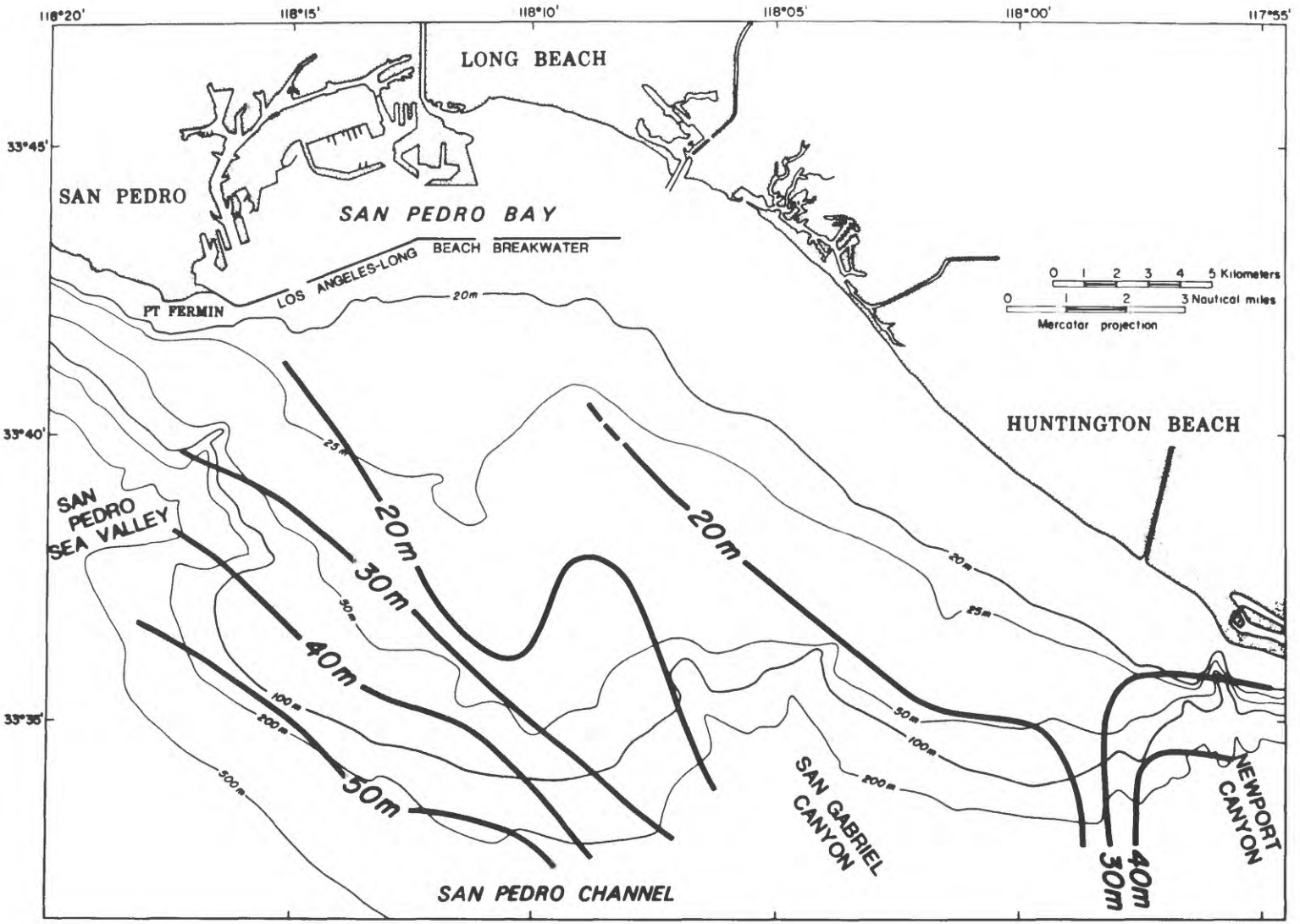

Figure 16. Depth to 25-75 sigma$_t$ surface

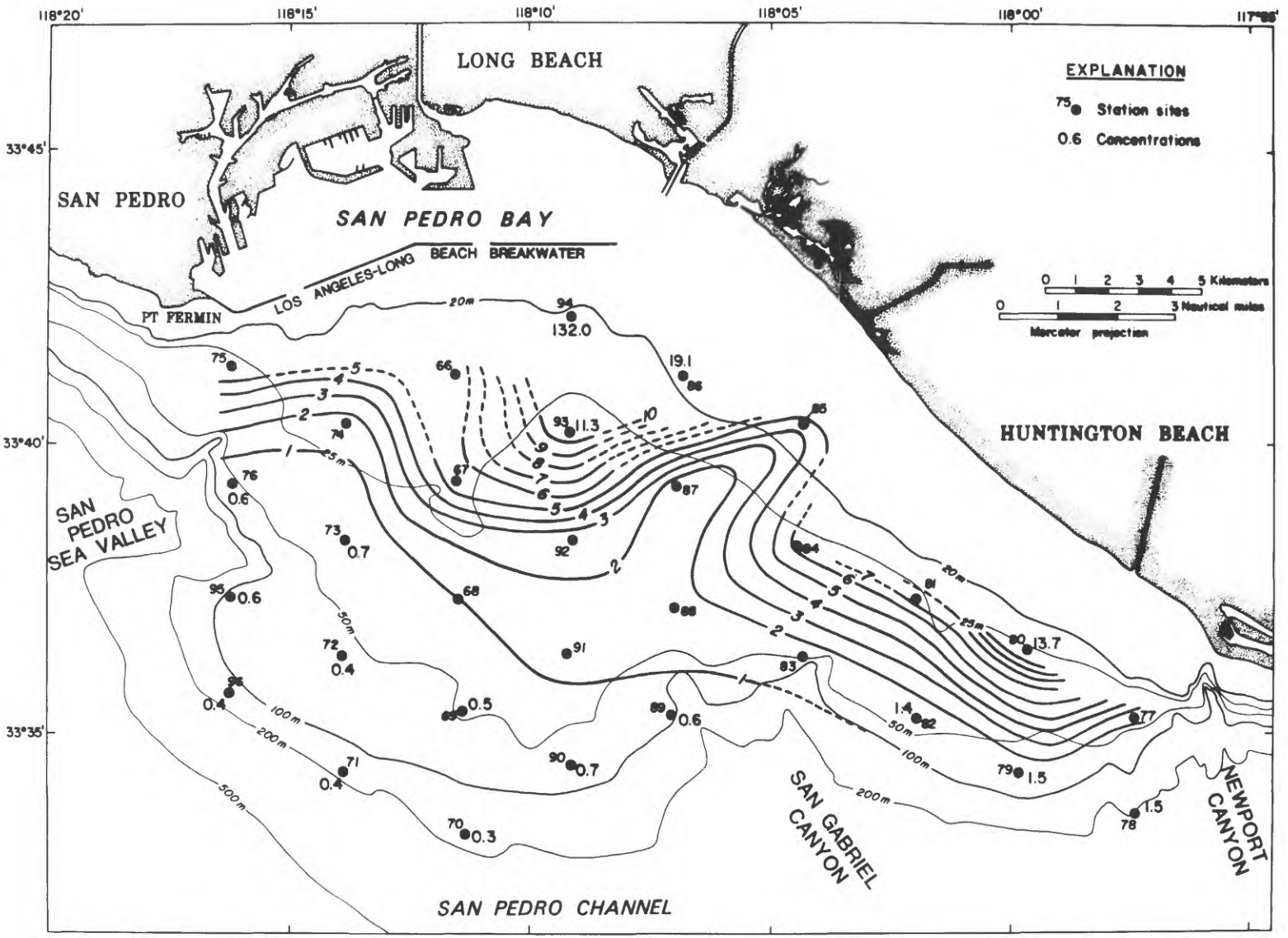

Figure 17. Areal distribution of total suspended particulate matter 1 m above bottom observed during April.

waves with periods between 15 minutes and 6 hours. These waves had previously been measured on southern California shelves (Lee, 1961; Cairns, 1968; Cacchione et al., 1976).

We selected the most rapid burst sampling rate possible on the Geoprobe system (1 sample per second) at G1A to examine effects of surface water wave motions. We also chose a burst length of 200 samples. This scheme would have permitted resolution of surface waves with periods greater than 2 seconds, and possible measurements of at least 14 consecutive waves with periods $\leq$ 14 seconds. Unfortunately, due to a malfunction in a switch in the data logger, we only obtained 72 samples per burst, taken at a rate of one sample per second (Table III). This malfunction limits the statistical reliability of the wave data. However, we feel that our results are sufficient to discuss the relevance of wave motion to transport at G1A.

Another problem in the Geoprobe operation was the failure of the pressure sensor on G2 (Table III). The underwater connector on the cable from the pressure sensor to the data-logger was faulty, allowing sea water to corrode the connector pins and short the power to the sensor. This failure occurred shortly after the tripod was deployed.

A third problem was the anomalously low speeds measured with the Savonius rotor on G2. The reed switch which senses the rotor spin rate apparently skipped counts resulting in low speed values. Also, the rotor current speed data for G1B trends to zero values after 20 days of operation (May 17). Therefore, only the first 20 days of data are considered reliable for that sensor.

Basic data

A statistical summary of the basic data records taken with each Geoprobe is provided in Table IV. In addition, Figure 18 and Figure 19 contain time-series plots of the basic data for each of the sensors on the long term Geoprobe tripods. The results of each data type are described below. Emphasis is on the results from the long term measurements (G1B and G2), because they are useful in examining the lower frequency events and average transport magnitudes and directions.

(1) pressure. The plot of hourly pressure averages in Figure 16 for G1B clearly shows the dominance of a mixed tide with a maximum range of 2.5 m (May 23) and a maximum diurnal inequality of about 1 m (May 23). As is typical of most tidal data on shelves, the diurnal inequality is less significant during neap (Godin, 1972). The forty-day pressure record at G1B also shows two complete cycles of the fortnightly tide.

Figure 20 contains a histogram of basic pressure data; mean pressure was 21.8 m corresponding to a mean water depth of 24.0 m at G1B.

(2) temperature. The major contrast in temperature data between G1B and G2 is that the mean near-bottom temperature at the shallower site is about 1.0°C warmer than at G2 (Table IV). In addition, the temperatures at G1B exhibit greater variance suggesting that low frequency thermal fluctuations were more energetic at the shallower site. The temperature record for the bottom temperature sensor (30 cm above sea floor) is plotted in both Figure 18 (G1B) and Figure 19 (G2). Both records show thermal oscillations of tidal frequency, with irregular, larger amplitude changes occurring at G1B (e.g., on June 1). Sub-tidal temperature fluctuations of about 1°C at G1B are also apparent. No reliable periodicity of these low frequency changes can be determined from the 40 day record, but these oscillations appear to have a recurrence interval of between 12 to 20 days. Since the temperatures are measured once each hour, fluctuations at periods less than two hours are not resolved.

TABLE III

Geoprobe operational summary for SPEX-1

Geoprobe #	Lat. (N)	Long. (W)	Depth (m)	Date Deployed time/date	Date Recovery time/date	Basic sample interval (min)	Samples per burst (#)	Sample rate (sec)
G1A	33°-40.06'	118°-11.89'	24	1000/4-18-78	1100/4-25-78	7.5	72	1
G1B	33°-40.00'	118°-11.92'	24	1327/4-26-78	1704/6-6-78	60	100	1
G2	33°-35.07'	118°-12.20'	67	2342/4-19-78	1355/6-5-78	60	100	1

TABLE IV. Summary of statistics of Geoprobe data for SPEX-1. Data were sampled in basic mode.

G1A	Pressure (m)	Rotor speed (cm/s)	Vane direction (deg)	Temp. (lower) (°C)	Temp. (upper) (°C)	Light transmission (rel.)	Light scattering (rel.)
Mean	20.99	12.09	188.64	11.46	11.49	0.66	0.05
Maximum	22.10	22.20	359.75	12.29	12.26	0.78	0.15
Minimum	19.90	6.17	4.74	10.91	10.92	0.34	0.02
Variance	0.31	9.57	-	0.18	0.18	0.00	0.00
Stand dev.	0.56	3.09	-	0.42	0.42	0.07	0.02
G1B							
		(*)					
Mean	21.83	10.89	204.00	11.76	11.71	0.25	0.14
Maximum	23.04	20.89	359.75	13.70	12.54	0.73	0.78
Minimum	20.55	0.00	3.33	11.01	10.99	0.00	0.02
Variance	0.25	13.02	-	0.14	0.12	0.03	0.01
Stand dev.	0.50	3.61	-	0.37	0.35	0.16	0.08
G2							
Mean		3.02	197.10	10.52	10.43	0.78	0.01
Maximum		9.85	359.75	11.03	10.98	0.93	0.20
Minimum	No Data	0.92	1.93	10.04	9.94	0.13	0.00
Variance		1.58	-	0.02	0.02	0.01	0.00
Stand dev.		1.26	-	0.15	0.15	0.08	0.01

(*) Only rotor data over first 20 days used because of fouling (see text).

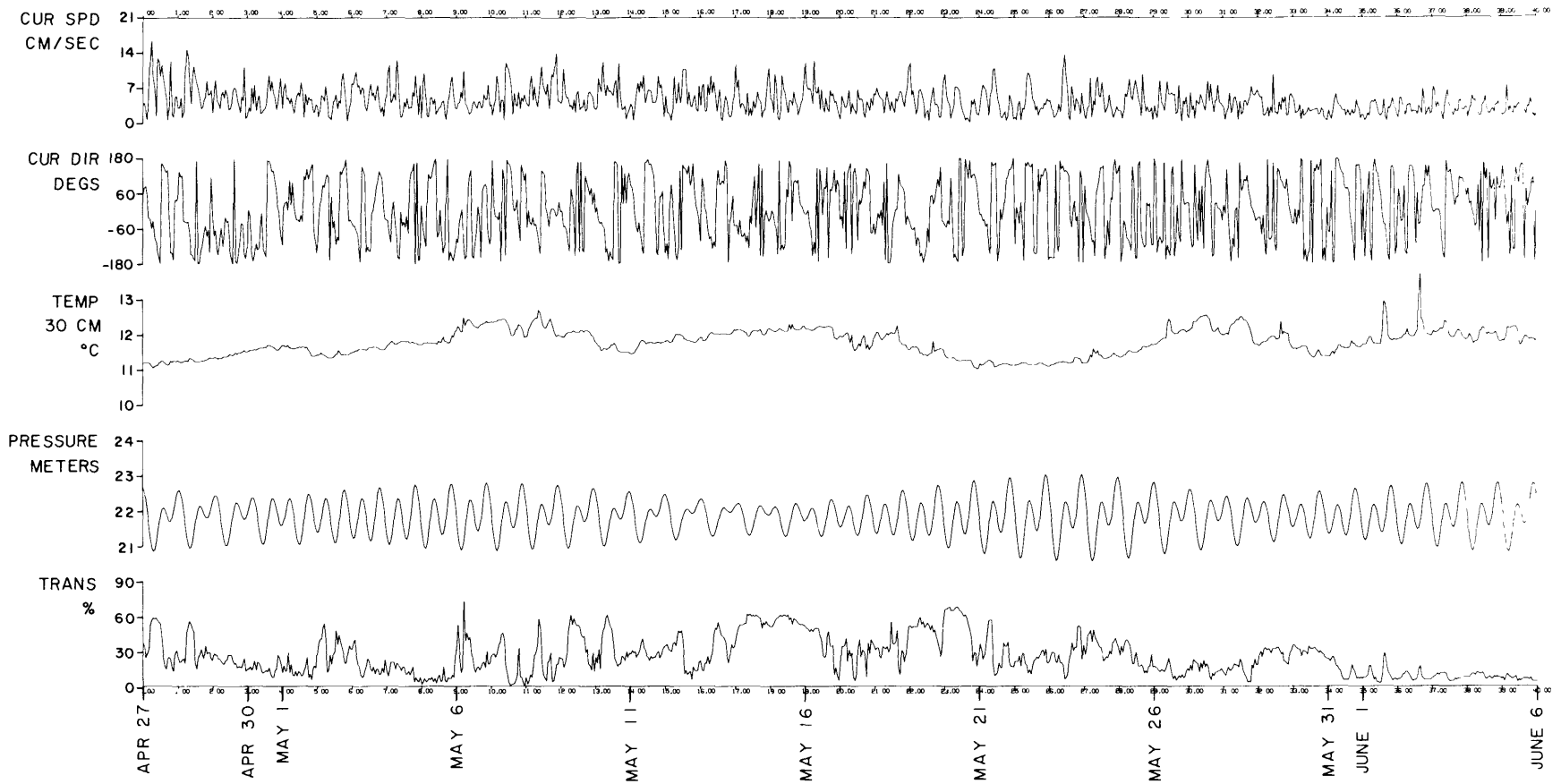

Figure 18. Hourly values of basic data obtained with Geoprobe at site G1B. Current speed and direction were measured by electromagnetic (e-m) current meter at 1 meter above sea floor.

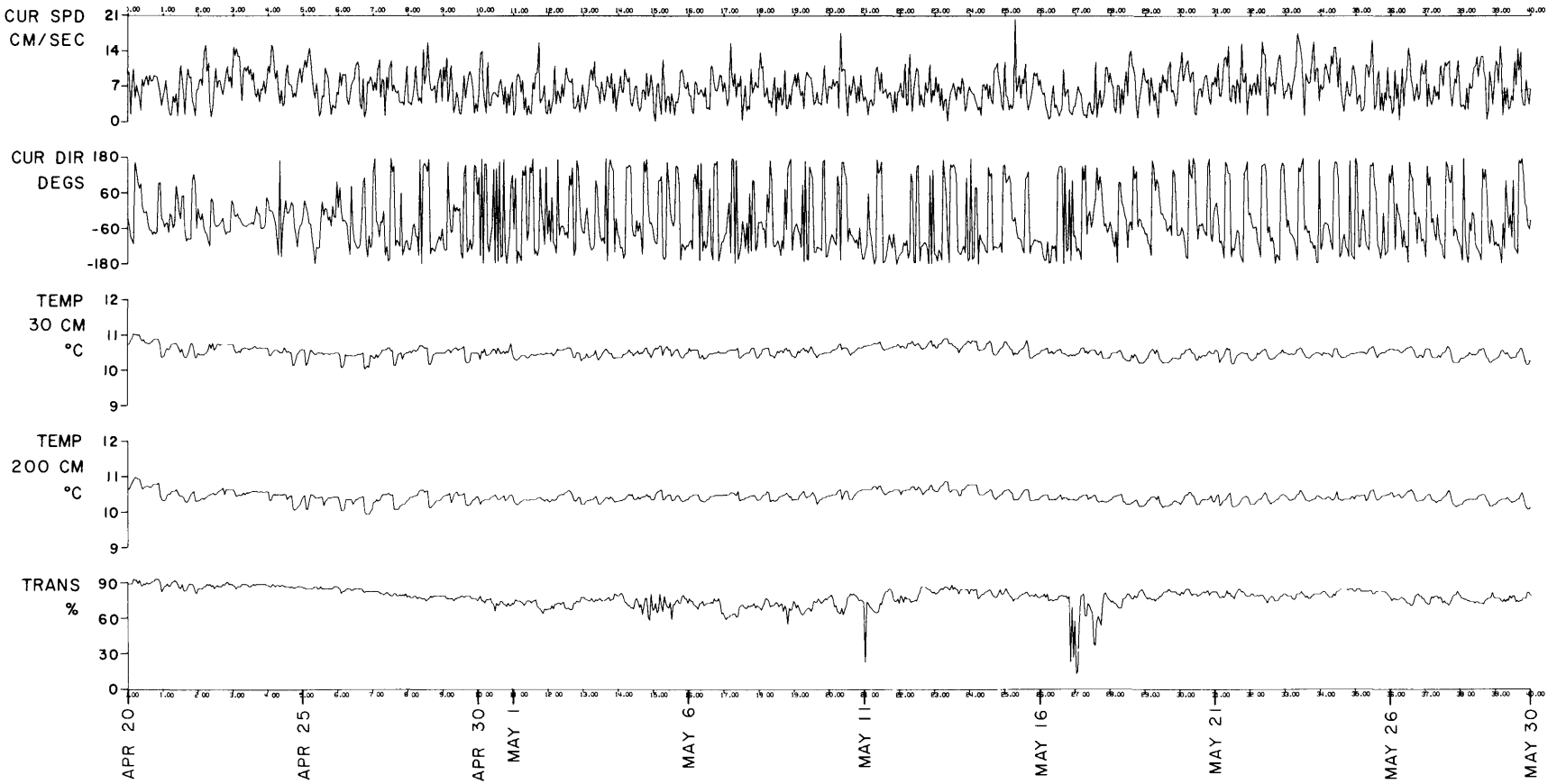

Figure 19. Hourly values of basic data obtained with Geoprobe at site G2. Current speed and direction were measured by electromagnetic (e-m) current meter at 1 meter above sea floor.

Figure 20. Histogram and statistics of basic pressure data - G1B

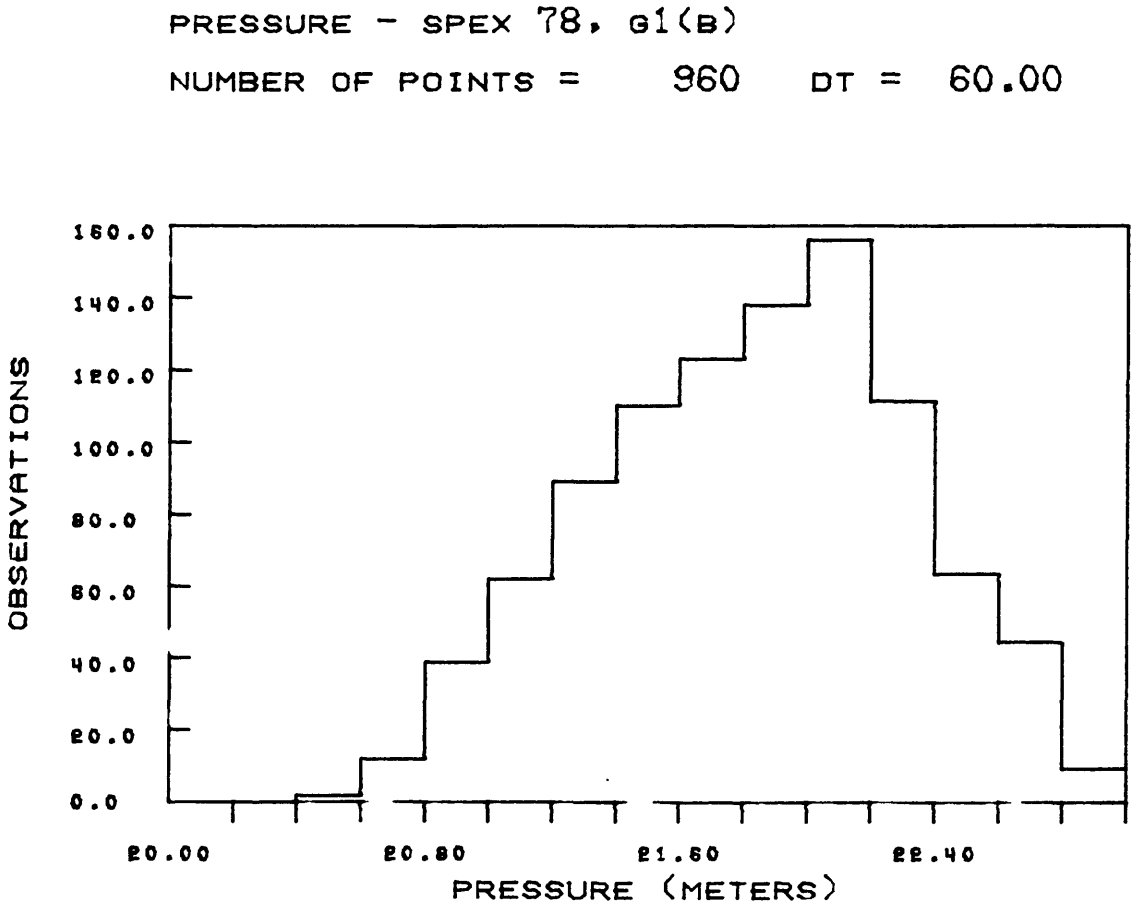

Histograms of temperature data taken with the upper sensors on G1B and G2 are shown in Figure 21 and Figure 22, respectively. The higher variability in near-bottom temperatures at the shallower site is obvious in these plots. The variance in temperatures is nearly an order of magnitude greater at G1B than at G2. Again, this difference is primarily due to the tidal and subtidal temperature changes discussed above.

(3) light transmission and light scattering. The light scattering data from the nephelometers are uneventful, as indicated by the extremely low variance values in Table IV. This result primarily arises from the small amounts of TSM at each site.

Light transmission, however, is more sensitive than 90° scattering at low TSM concentrations, and is more useful in this study. The absolute values of transmission and scattering for each Geoprobe (Table IV) are relative units that do not include instrument calibrations. Therefore, the numerical differences in mean, maximum, and minimum between G1B and G2 (Table IV) are not significant. However, their sense is correct; that is, considerably more turbid water was present at G1B than at G2, as the higher mean at G1B would the spread of values in the histograms, quantitatively indicated by the standard deviations, shows that hourly turbidity levels at G1B were more variable (Figs. 23 and 24).

Time-series plots of light transmission clearly document the greater turbidity fluctuations at the shallow site (Figs. 18 and 19). Changes of up to 50% transmission (relative) occur several times over two consecutive hourly measurements at G1B (e.g., on May 8). By contrast, consistently high values of light transmission were measured at the deeper site (Fig. 19) throughout the record, except for periods when the optics were probably fouled (e.g., on May 11 on May 11 and May 17). A period of more variable turbidity did occur at G2 during May 4-6, with maximum changes of about 15% transmission.

(4) current speed and direction. The data for current speed and direction sampled in the basic modes are taken with a Savonius rotor and small vane. The rotor provides an average speed over the basic interval; whereas the vane gives a single, instantaneous measurement of current direction during each interval. Table IV shows that the mean rotor speed at G2 was relatively low (~3 cm/s). The record for G1A had a mean speed over the 5 days of about 12 cm/s. The mean speed for G1B over the first twenty days was ~11 cm/s (Table IV). Maximum hourly-averaged current speeds did reach 20 cm/s at G1B; G2 had a maximum of only 9.8 cm/s.

The low speeds in the statistics for G2 in Table IV are the result of a malfunction in the rotor. Therefore these statistics are unreliable; the burst-averaged current speeds for the electromagnetic speed sensors (see below) should be used in lieu of the G2 rotor results.

In all three Geoprobe records, the long-term mean flow direction was predominantly south-southwesterly (Table IV). This flow direction implies net offshore movement of the near-bottom water.

Time-series plots of current speed and current direction show that, although the tidal signature can be discerned in the currents at G1B (Fig. 18) and G2 (Fig. 19), the records have irregular fluctuations superimposed on the tidal signals that suggest significant motions at supratidal frequencies. These motions are probably the result of propagating internal gravity waves and are discussed below.

Current directions also show a tidal variation, with superimposed, higher frequency changes. The deeper measurements at G2 have greater occurrence of these higher frequency motions, particularly during the period of April 29 - May 3.

Figure 21. Histogram and statistics of temperature data (upper sensor) - G1B

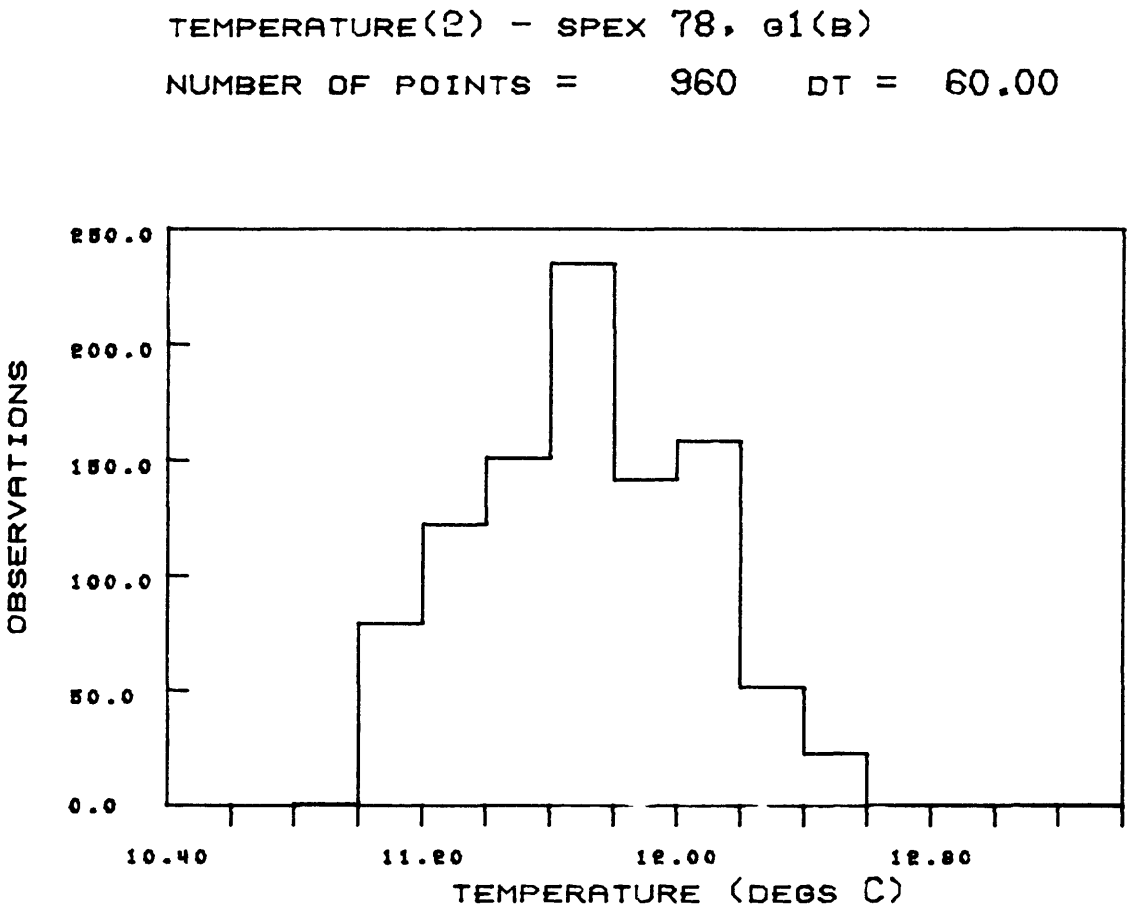

Figure 22. Histogram and statistics of temperature data (upper sensor) - G2

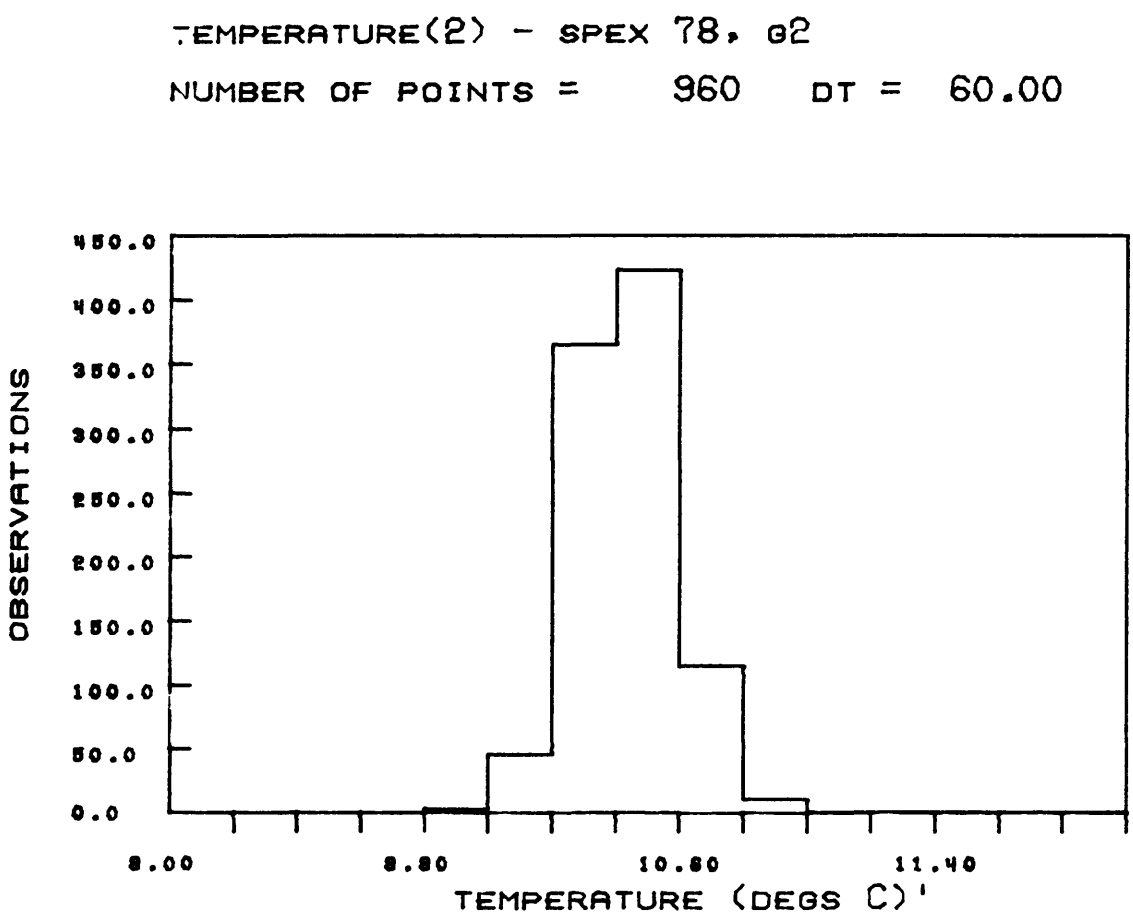

Figure 23. Histogram and statistics of light transmission data - G1B

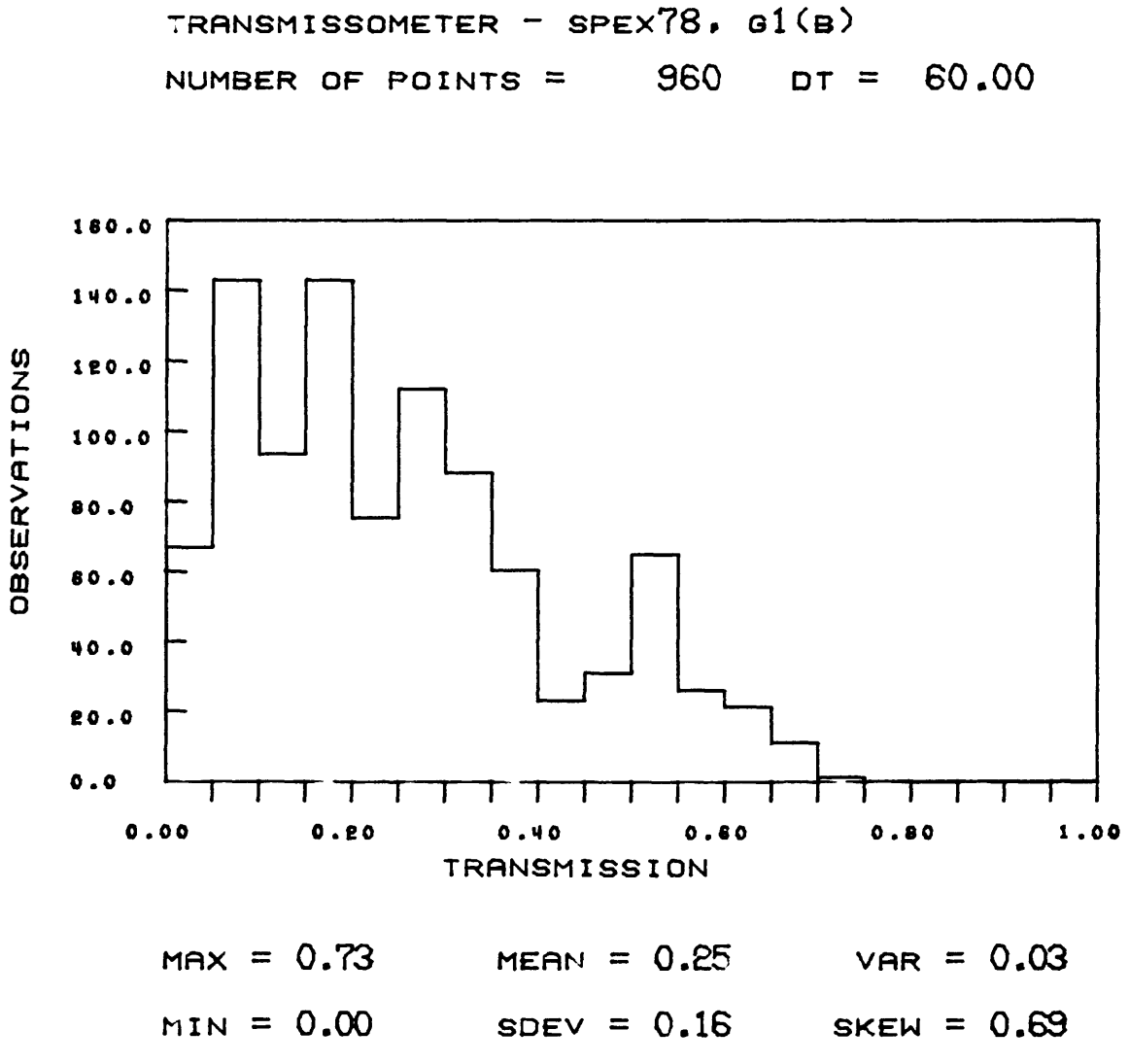

Figure 24. Histogram and statistics of light transmission data - G2

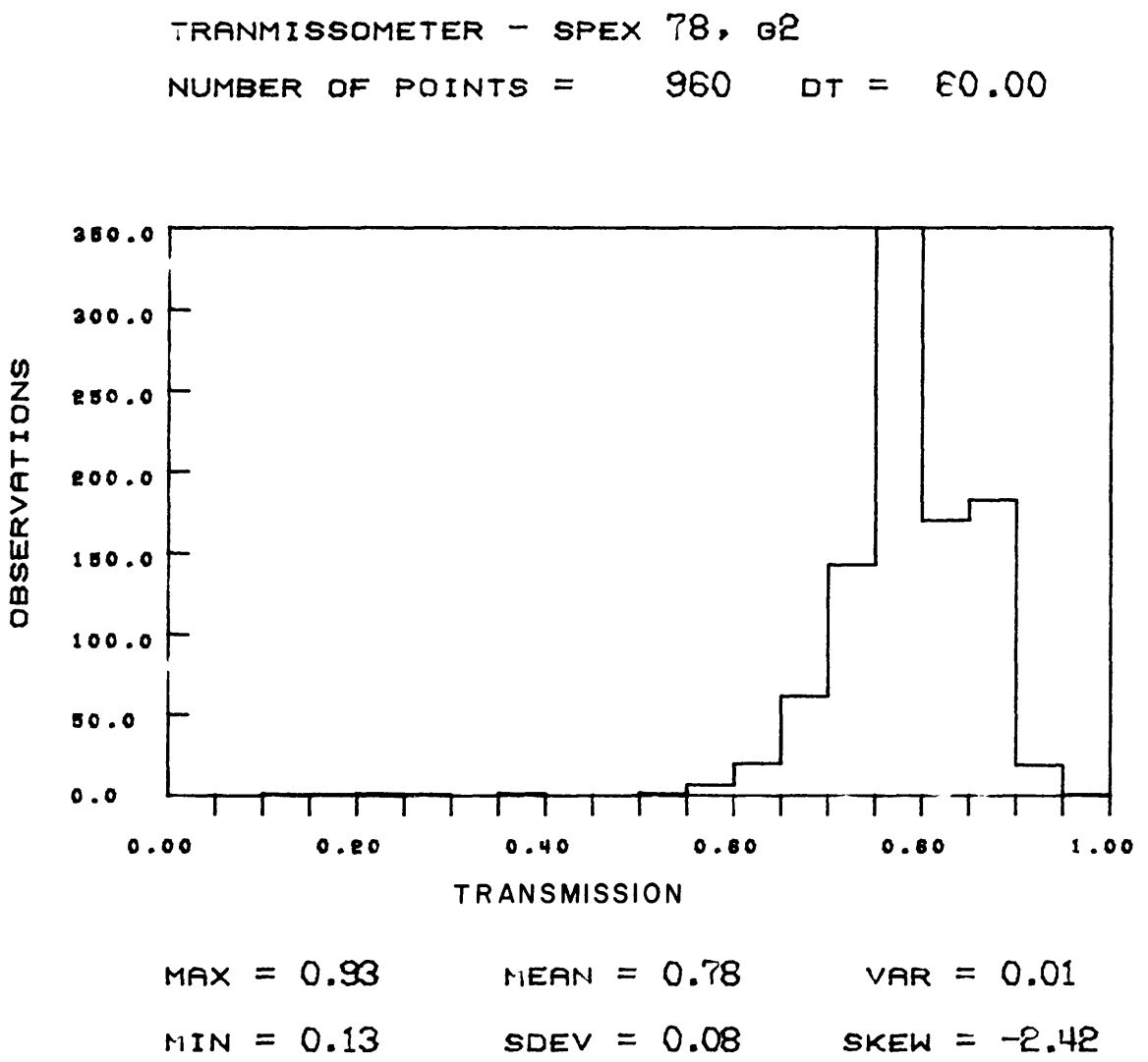

Burst data

(1) low frequency motions. The four electromagnetic current meters on each tripod provided measurements of bottom currents at four levels in the burst mode (Cacchione and Drake, 1979). The pressure sensor was also sampled in this mode to provide surface wave data. As discussed above, the pressure sensor on G2 did not operate during the entire experiment.

Each electromagnetic current sensor measured horizontal speeds of two orthogonal components once each second over the entire burst (Table III). These measurements of horizontal components were first rotated by computer calculations to produce north-south (v) and east-west (u) speed components. Current vectors representing each one-second measurement were then computed with magnitude, s, and direction, θ.

$$s = (u^2 + v^2)^{1/2} \quad ; \quad \theta = \tan^{-1} \frac{v}{h} \qquad (1).$$

Appendix D contains plots of s and pressure (p) for bursts samples taken at G1B and G2. A plot for every second day at 1230 local time is shown for G1B to document the variability in wave motion at the shallower location over the 40 day experiment.

The horizontal speed components, u and v, were also averaged over each burst, to estimate average speed, $\bar{s}$, and direction, $\bar{\theta}$:

$$\bar{u} = \frac{\sum_{i=i}^{N} u_i}{N} \quad ; \quad \bar{v} = \frac{\sum_{i=i}^{N} v_i}{N}$$

$$\bar{s} = (\bar{u}^2 + \bar{v}^2)^{1/2} \quad ; \quad \bar{\theta} = \tan^{-1} \frac{\bar{v}}{\bar{u}} \qquad (2).$$

In the cases of G1B and G2, N = 100; for G1A, N = 72. $\bar{s}$ and $\bar{\theta}$ are hourly burst averages of the data from electromagnetic (e-m) current sensors on G1B and G2. For G1A, they represent burst averages obtained every 7.5 minutes.

$\bar{s}$ values are plotted for the long-term records in Figure 25 (G1B) and Figure 26 (G2). These data are considered to be accurate to about 1 cm/s. The upper e-m current meter (CM4) and the rotor speed data on both tripods were coherent throughout the records. Based on analysis of Geoprobe photographs, the severe fouling of the sensors, and the nature of the speed curves in Figure 25, we feel that the speed values beyond day 32 (May 28) are unreliable and consistently low. The burst averages, $\bar{s}$, for the short term deployment, G1A, are shown in Figure 27.

Inspection of Figures 25-27 indicates three important features: (1) tidal current speeds are relatively low in the long-term records (Figs. 25 and 26); (2) bottom current speeds at the shallow and deep sites have similar magnitudes; and (3) speed fluctuations at supratidal frequencies are significant. Figure 27 clearly shows higher frequency oscillations in current speed superimposed on the tidal currents. In Figure 25 there are about 10 current speed maxima every 3 hours, corresponding to a periodicity of about 30-40 minutes. At the lower resolutions in the longer-term records in Figures 25 and 26, there are typically 8 current maxima each day, which suggests a periodicity of about 6 hours. Both of these motions (0.5 hours and 6 hours) are probably caused by internal waves.

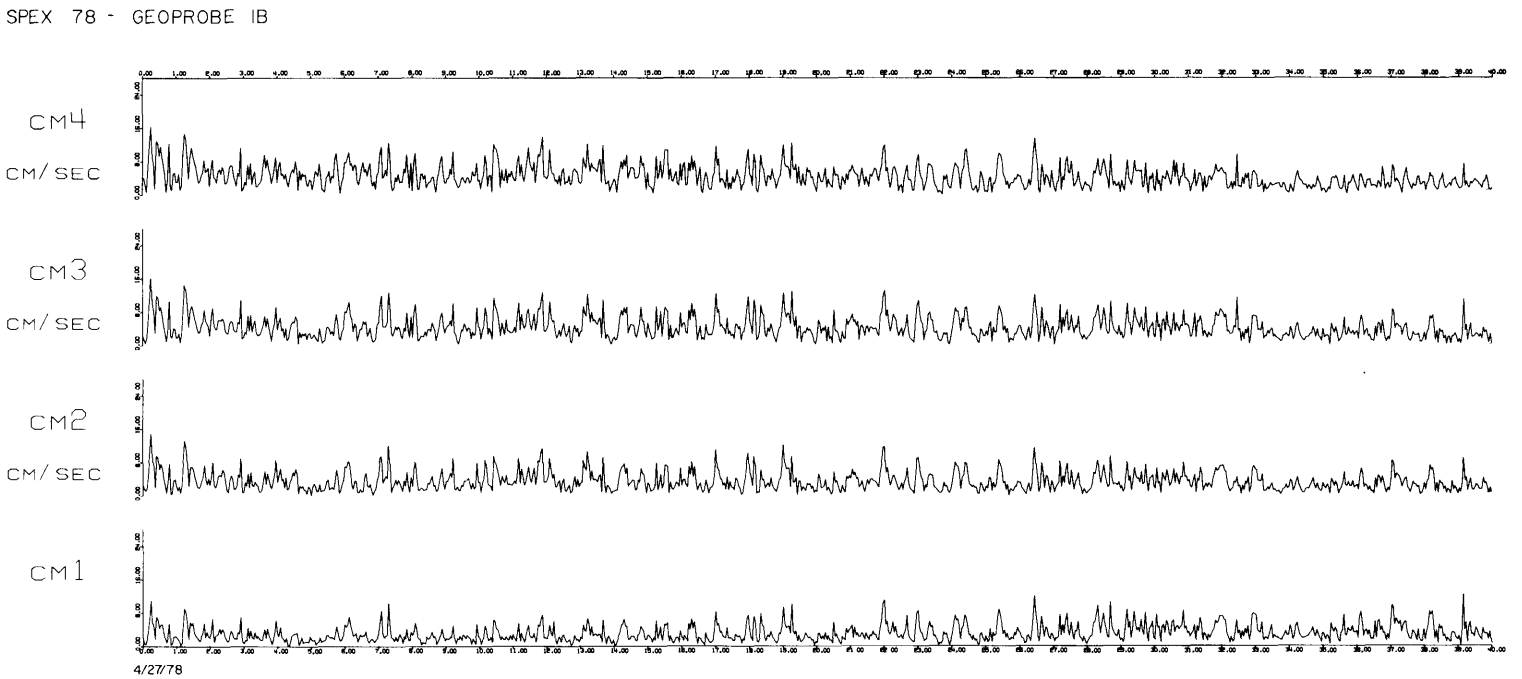

Figure 25. Hourly burst averages of horizontal current speed for e-m sensors at 20 (CM1), 50 (CM2), 70 (CM3), and 100 (CM4) centimeters above the bottom. Horizontal axis is days from start (0000 on 4/27/78). Vertical axis is speed (cm/s) and reads 0.00, 8.00, 16.00, and 24.00. Horizontal axis is days beginning 4/27/78.

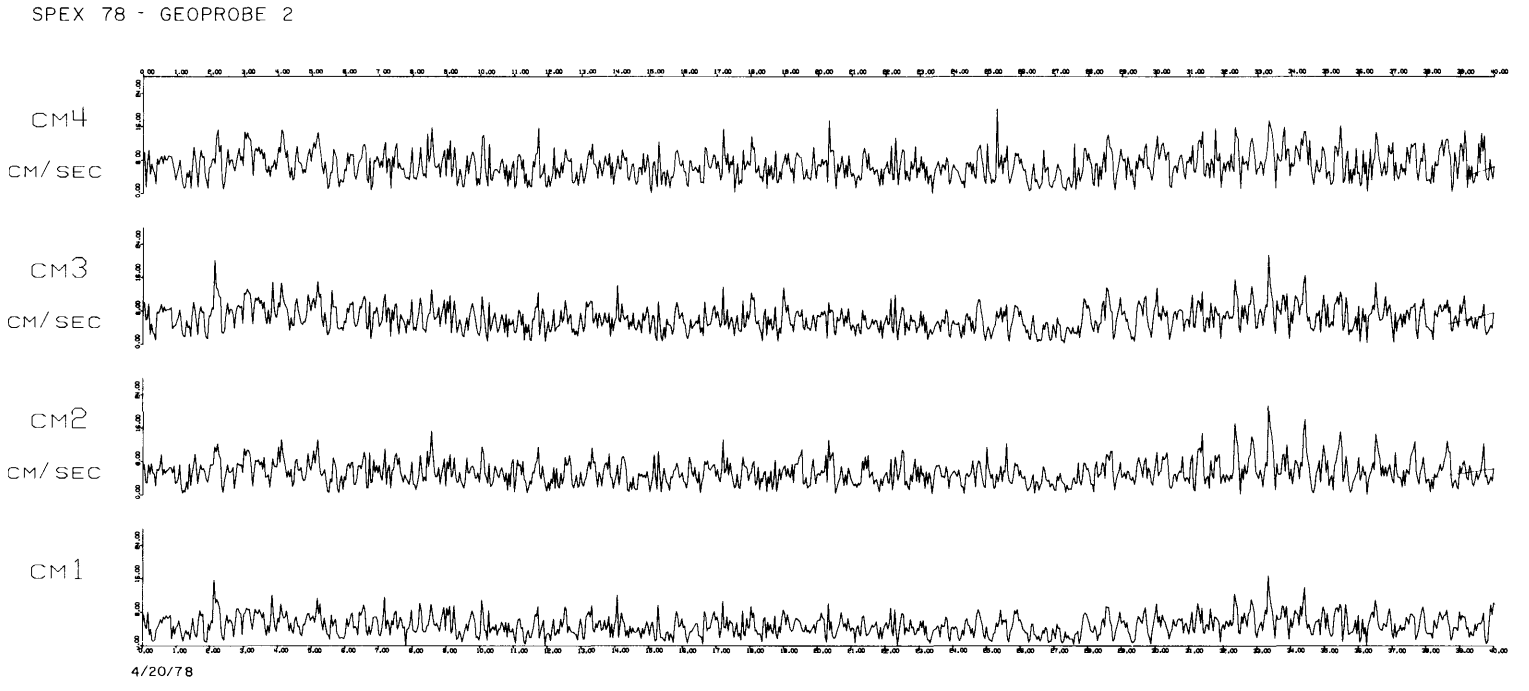

Figure 26. Hourly burst averages of horizontal current speed for e-m sensors at 20 (CM1), 50 (CM2), 70 (CM3), and 100 (CM4) centimeters above the bottom. Horizontal axis is days from start (0000 on 4/20/78). Vertical axis is speed (cm/s) and reads 0.00, 8.00, 16.00, and 24.00. Horizontal axis is days beginning 4/20/78.

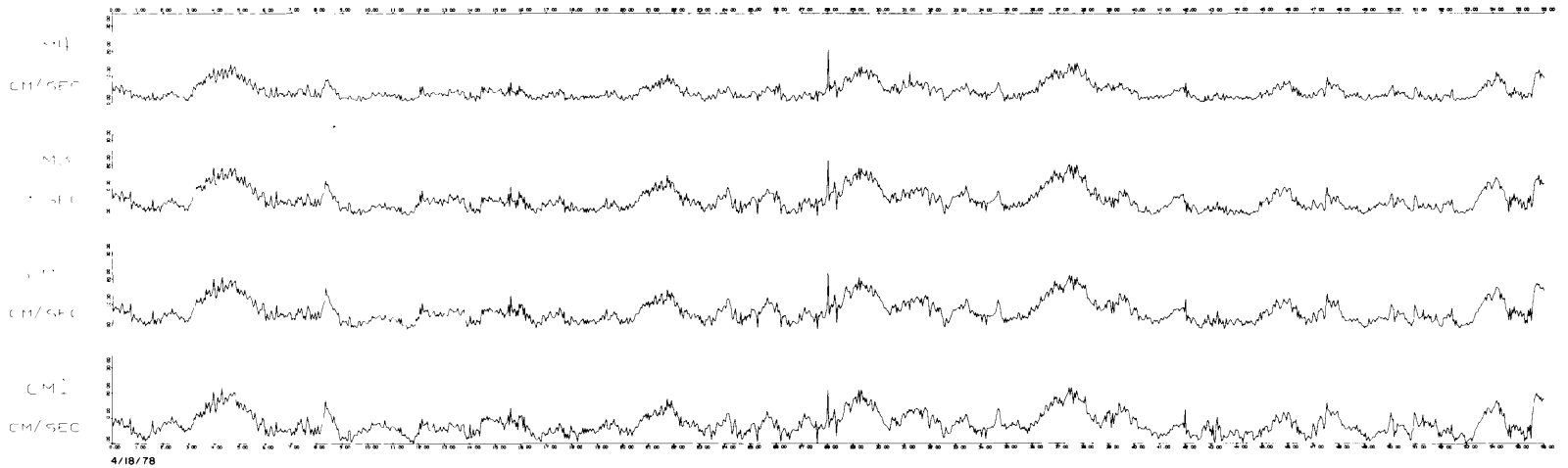

Figure 27. Burst averages (one value every 7.5 minutes) for e-m sensors at 20 (CM1), 50 (CM2), 70 (CM3), and 100 (CM4) centimeters above the bottom. Horizontal axis is marked every 3 hours from start (000 on 4/18/78). Vertical axis is speed (cm/s) and reads 0.00, 10.00, 20.00, and 30.00. Horizontal axis is days beginning 4/18/78.

Appendix A contains the results of our time-series analysis of e-m current sensors CM4 (uppermost) and CM1 (lowest) on G1B and G2. A similar analysis for CM4 (uppermost) on G1A is also presented there. Histograms and statistics for each of these sensors (Figs. A-1, A-7, A-13, A-19, A-25) illustrate the predominantly low speeds throughout the experiment. The increased frequency of occurrence of higher speeds at the upper e-m (e.g., Figs. A-1 and A-7) also demonstrates the decreasing velocity magnitudes in the bottom boundary layer, indicative that the Geoprobes were actually within the frictional bottom layer.

The speed data in Appendix A have also been plotted as N-S and E-W components (Figs. A-2 and A-3 for CM4 on G1B, and Figs. A-14 and A-15 for CM4 on G2). These component plots show the tidal periodicities more clearly than the total speed plots. There is some indication in the diminishing speed values for CM4 at G1B (Fig. A-3) that this sensor was malfunctioning after about May 28.

The kinetic energy spectra for the upper sensors at each long-term site show the dominance of tidal energy. Figure A-5 demonstrates the nearly equal tidal peaks at the diurnal (K_1) and semi-diurnal (M_2) periods. By contrast, Figure A-17 at G2 shows lower energy at both tidal frequencies by about an order of magnitude, and a marked decrease in the K_1 tide relative to the M_2 tide. Similar changes in offshore tidal energetics have been reported for current records taken off southern California by Winant and Davis (personal communcations). The kinetic energy spectra of N-S (v) and E-W (u) components (Fig. A-6 and Fig. A-18) further show the tidal energy is greatest for the u component at both semi-diurnal and diurnal frequencies. This result suggests that the tide has its most intense motion nearly parallel to the bottom contours.

Another important and as yet unexplained result is that the rotary spectra for the e-m current data at the shallow site show that the K_1, tide propagates in a counterclockwise direction (Fig. A-6 and A-12). The data at G2, however, do not show a similar K_1 tidal rotation (Figs. A-18 and A-24). There is some indication that at G2, the K_1 tidal motion is clockwise. This suggests a decoupling in the lower frequency tidal motion between these two sites.

It is also worth noting that the inertial period (frequency) for this shelf region is about 21.5 hours (4.7×10^{-2} cph). The kinetic energy (K.E.) spectra for all e-m sensors (e.g., Fig. A-5) show, at most, a small peak in current energy at or near the inertial period. This result also agrees with other current meter data taken on southern California shelves (Winant, personal communication).

The K.E. spectra show significant peaks at frequencies in the internal wave band. The cut-off frequency in the spectra for the long-term measurements is 0.5 cycles/hour (2 hour period). Significant spectral energy peaks occur at about 2.0, 5.0, 6.5, and 8.0 hours at G1B (Fig. A-5) and at about 2.0, 4.6, 6.0, and 8.0 hours at G2 (Fig. A-17). A smaller spectral peak also occurs at 3.5 hours at G2 (Fig. A-17). These peaks probably represent internal waves propagating over the shelf from offshore generating regions (Cacchione and Drake, 1976).

The K. E. spectra for G1A (short-term) resolves energy content to a cut-off frequency of 4 cycles/hour (15 minute period). Figure A-28 shows several significant spectral peaks at relatively high frequencies, particularly at 18, 24, 36, and 54 minutes. The peak at 3.0 hours is also significant at the 95% confidence interval. These high frequency internal waves are probably responsible for the irregular motion seen in the data in Figure 9.

Finally, the long-term measurements show an extremely important result for transport of near-bottom materials: over the 40 days of the experiment, the net movement of materials was offshore, towards the south-southwest. The progressive vector diagrams in Appendix A indicate the path a particle would

take if responding to the flow measured at each site. For example, at G2 (Fig. A-16), the net transport at 1 meter above the sea floor for the period April 20-26 was southeasterly at about 5 km/day (5.8 cm/s); and from April 26 to May 30 the flow was southwesterly at about 2.6 km/day (3.1 cm/s). This latter net flow speed also occurred at the lowest e-m sensor on G2 (Fig. A-22).

At G1B, the net transport was more variable in direction and less intense, trending south-southwesterly at 1 m above the bottom from April 27 to June 2, with several days of easterly flow interspersed (Fig. A-4). The net flow over the entire period to June 6 was southwesterly at about 0.4 km/day (0.4 cm/s). At the lowest e-m sensor on G1B, the net rate was southerly at about 1.1 km/day (1.2 cm/s). The net flow at the shallower site, therefore, was considerably slower than the net flow at G2.

One further aspect of the progressive vector diagrams is the turning in net flow direction from lower to uppermost current sensor (Fig. A-16 and A-22). This veering is consistent with the other e-m current sensor progressive vectors results (not shown). Quite possibly this turning is a result of Ekman veering in the lower part of the bottom turbulent Ekman layer.

(2) surface wave data. The burst data from pressure and e-m sensors provide synoptic measures of surface wave effects at the sea floor. Examples of these data are shown in Figure 28 and Figure 29 for G1B and G2, respectively. These plots contain one hundred points for each e-m sensor, with speed, s , computed from equation (1). The corresponding pressure record is also plotted for G1B. A selected group of similar plots is provided in Appendix B. These plots are included to document the variable wave conditions and to show actual bottom speeds due to surface waves.

The most impressive feature in the wave records, particularly at the shallow site, is the rhythmic oscillations in bottom pressure due to the swell. The bottom pressures illustrated in Figure 28 correspond to surface waves with heights, H , of about 0.7 meters. Average wave period, T, over the record in Figure 28 is about 12.8 seconds. The wave length, L, corresponding to this average period can be calculated from linear wave theory (Kinsman, 1965). In this case, $L \simeq 177$ meters. The maximum horizontal bottom speeds due to surface waves in the plots occurred on May 27 at site G1B (Appendix B). The peak wave speeds were above 25 cm/s. This high wave surge was caused by the low frequency swell evident in the pressure record ($T \simeq 18$ sec.).

DISCUSSION

Substrate

Because grain-size distribution shown in Figure 7 is based on the results of a previous study (Karl, 1976), the areal trends are not interpreted in detail in this report. The samples collected during this experiment were used only to establish the grain-size distributions at Geoprobe and SMS sites. By calculating shear stresses at the Geoprobe sites, it is then possible, using grain-size data, to estimate the frequency with which sediment at these sites is being transported. Of interest on Figure 6 is the zone of fine-grained sediment on the shelf adjacent to San Gabriel Canyon. As discussed by Karl (1980a) this zone may represent a corridor for the seasonal and episodic preferential transport of suspended particulate matter; thus pollutants released near the area would be preferentially transported toward the head of San Gabriel Canyon. As noted by Karl (1980a), this corridor is best defined during the winter and may not be active during the spring and summer.

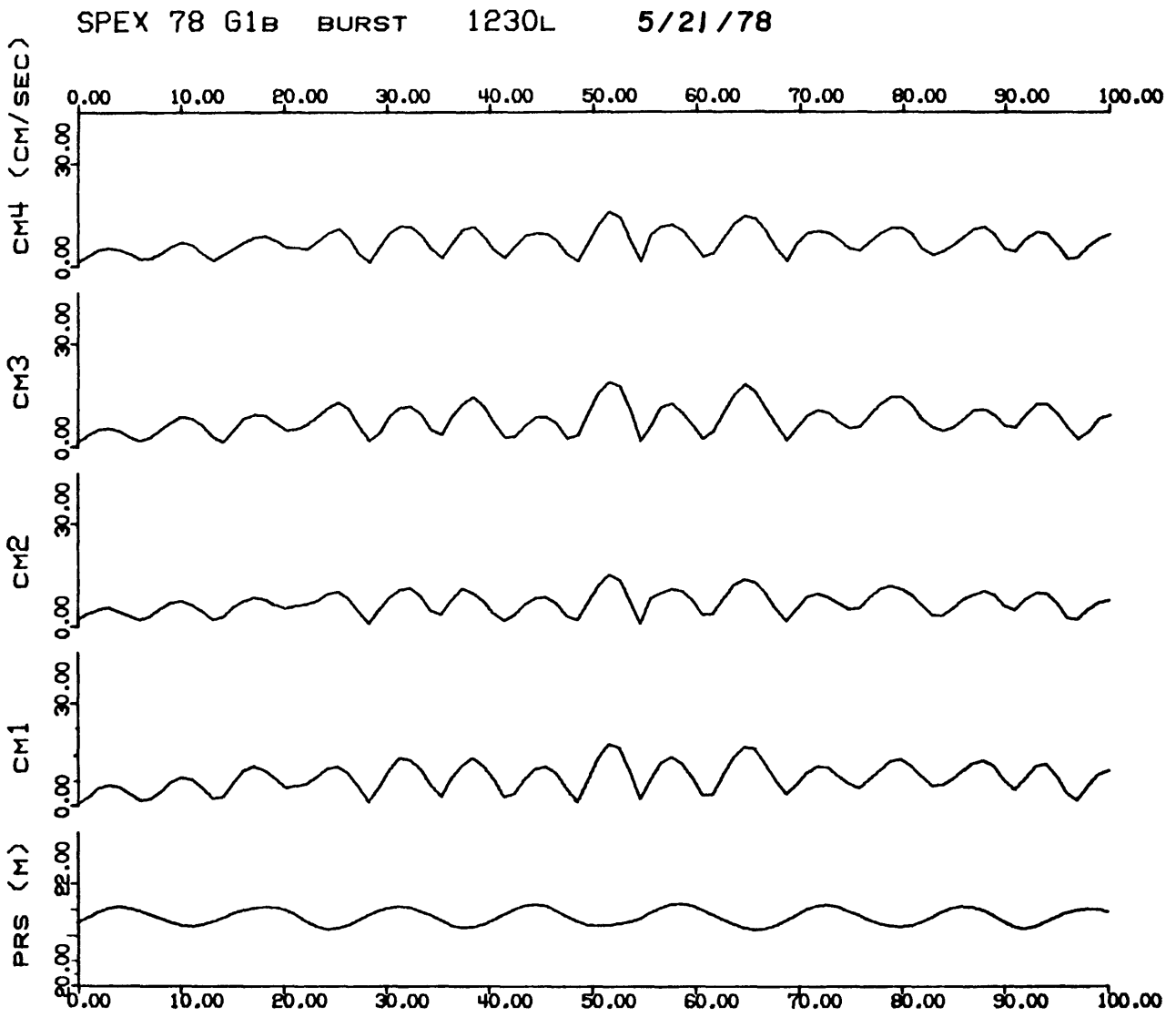

Figure 28. Burst speed data from e-m sensors on G1B. Burst pressure (PRS) is given in meters of water. Horizontal axis is seconds.

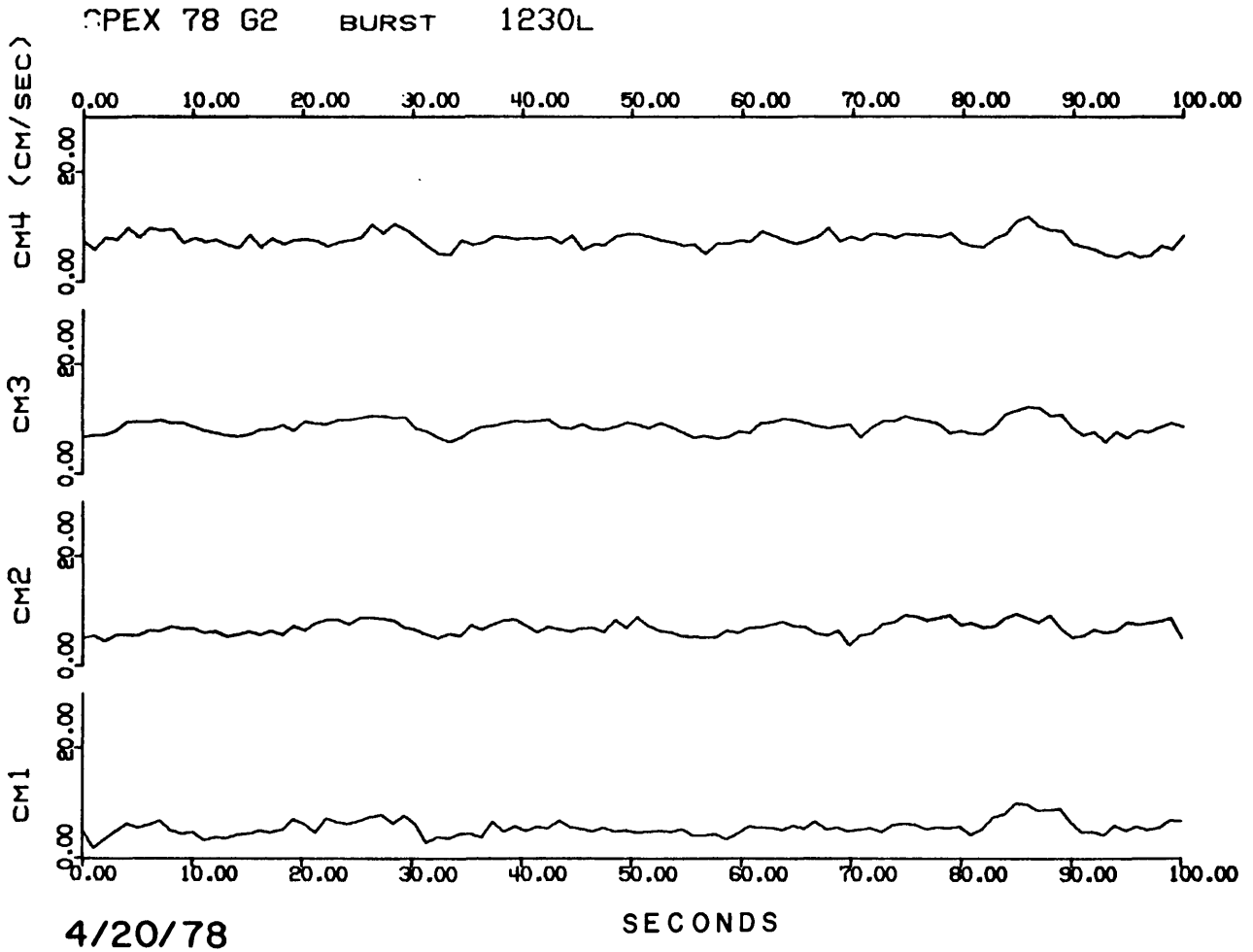

Figure 29. Burst speed data from e-m sensors on G2.

Geophysical surveys were made primarily to establish the morphology of the sea-floor at each of the instrument sites, and we lack sufficient data to make meaningful interpretations of sub-bottom profiles and assessments of potential geologic hazards. The line shown in Figure 10 is an example of extensive slumping along the walls of Newport Canyon. This slumping may result from sediment loading caused by high rates of mud deposition. This suggests that, although Newport Canyon may no longer be active as a "sand" canyon (Felix and Gorsline, 1971), it is a depositional site for fine-grained material, and it is a potential sink for pollutants released and dispersed on San Pedro shelf to the east of San Gabriel Canyon. For a detailed evaluation of other potential geologic hazards on San Pedro shelf, we refer the reader to the report by Greene et al. (in press).

Bedforms

Well-developed ripples on the shelf reflect the periodic transport of sediment as bedload. The origin of the type A ripple geometry is not clear. Karl (1976) suggested four possible mechanisms for generation of these ripples; one of these included formation by interfering wave trains.

Waves approach San Pedro shelf through corridors from the west and south. Islands and banks tend to attenuate long period (15-20 sec) swell from the west (Horrer, 1950), leaving short (7-10 sec) period waves to pass relatively free of interference. Long period waves propagating from the south reach the shelf without interruption. Short period waves from the west interferring with these long period swell from the south could account for type A ripples observed at Geoprobe site 1 and other shallow stations. Although data from G1B indicates that wave generated currents were, at times, sufficiently strong (>20 cm/s) to form ripples, we cannot deduce wave direction; hence the origin of type A ripples remains problematic.

The symmetrical ripples occurring on deeper areas of the shelf can be attributed to long period surface waves propagating from the southern hemisphere. Data from the Geoprobes support a surface wave genesis for these bedforms. Mean velocities (>1 - 3 cm/s) are too low to move sediment as bedload, but instantaneous wave velocities (>20 cm/s) are easily capable of moving bedload particles at both Geoprobe sites (Appendix E). The progressive change from biogenically-reworked sediment on the outer shelf to well-developed wave ripples nearshore reflects a gradual increase of energy characteristic of shoaling surface waves. Thus, the distribution, orientation and morphology of small-scale bedforms on San Pedro shelf are consistent with a surface wave origin (see also Karl, 1975). It could not be determined how many, if any, of these bedforms were remnant features from large storms passing through the area before the April cruise.

Water Column

Upwelling typically occurs along the southern California coast from March through June. Figures 11, 12, 14 and 15 show that during the 8 day period between 19-27 April, cold and dense water moved from the upper slope off Point Fermin (Palos Verdes Peninsula) onto the shelf where it spread southeastward. Net transport near the bottom, integrated over 1.5 m above the bottom, during this period as measured at both Geoprobe sites was to the southeast (Figs. A-22, A-27). Between 26 and 27 April net current direction changed dramatically to southerly flow and remained persistently south-southwest for the rest of the experiment (A-22).

Wind is the most common mechanism forcing an upwelling event. The closest good wind measurements to the study area are made at Long Beach Airport. A progressive

vector diagram of resultant wind direction from 8 April to 7 June shows that from 16-27 April this wind was southwesterly blowing from 250° (Fig. 29). Prior to 16 April and after 27 April the wind was southerly from about 195°. These changes in wind direction correlate with the changes in near-bottom net current direction on 27 April from southeastward to southward flow.

In the northern hemisphere, surface water moves to the right of the prevailing wind. Thus a southwesterly wind accounts for the southeasterly surface drift currents. In deep water (>100 m), the anticyclonic spiralling continues unimpeded to produce a fully developed Ekman spiral. In shallow shelf waters, frictional resistance of the sea-floor prevents full development of the surface Ekman spiral. In fact, a reverse spiral may develop from the sea-floor upward. The CTD profiles evince a three-layer system on San Pedro shelf; the surface layer separated fromthe bottom layer by a relatively strong pycnocline. Net flow directions measured by the E-M current meters indicate Ekman veering, described further in subsequent paragraphs, within 1 m of the bottom at both Geoprobe sites. Although both the surface water and near-bottom water are flowing southeasterly during an upwelling event, the former may be governed by the surface winds whereas the latter may be influenced by bottom friction. Because we lack measurements in mid-water depths, we are uncertain as to flow directions in this zone. Thus, we cannot establish whether or not the whole shelf system responds as a unit to westerly wind stress.

CTD and transmission profiles suggest that a mid-water wedge of relatively cold, dense and clear water is moving shoreward (Figs. 11-13). If this is the case, then offshore flow at the surface and bottomwould balance the volume of mid-depth water driven shoreward and to the surface by the wind stress. Data from the Coastal Upwelling Experimental Analysis (CUEA) program off the Oregon-Washington coast and off Peru show that offshore drift at the bottom is replenished by upwelling waters flowing onshore at mid-water depths (personal cummunication, D. Halpern, 1978; Brink et al., 1978; O'Brien et al., 1978).

The nature of the isopycnals in Figures 12 and 16 suggest a more complex flow pattern than simple southeasterly drift over the whole shelf during an upwelling event. The 25.75 sigma$_t$ surface slopes upward from both the northeast and southwest to form a ridge that crests at 20 m below the water surface (Figs. 12 and 16). The isopycnals slope more steeply away from the crest of the ridge to the southwest than to the northeast. This indicates a southeasterly flowing current on the seaward side of the "ridge" and a weaker northwesterly drift on the landward side. Thus, upwelling may generate or reinforce a cyclonic eddy in San Pedro Bay. This interpretation is supported by data compiled from satellite images discussed by Pirie et al. (1975).

Because we have no regional hydrographic data after 28 April, we cannot discuss the non-upwelling situation in detail. The persistent southerly flow near-bottom correlates with steady winds from about 195°. We speculate that the southerly wind pushes surface water landward. The configuration of the coast line traps the surface water causing a warm water wedge nearshore. This may generate a coastal downwelling which possibly explains the net offshore drift at the sea-floor.

The importance of local coastal upwelling to pollutant transport is illustrated by the dramatic effect it produces on the distribution of suspended particulate matter. On 19 April, just after the onset of upwelling, the water column, except very close to shore, was relatively non-turbid (Fig. 11a). By 27 April, after upwelling conditions were fully developed, transmission profiles show highly turbid zones at the surface and bottom (Fig. 11b). Currents generated during the upwelling regime advected seaward nearshore surface particulate matter, present in concentrations higher than normally expected during spring owing to terrigenous input from rains several weeks prior to data collection, and particles near the bottom resuspended

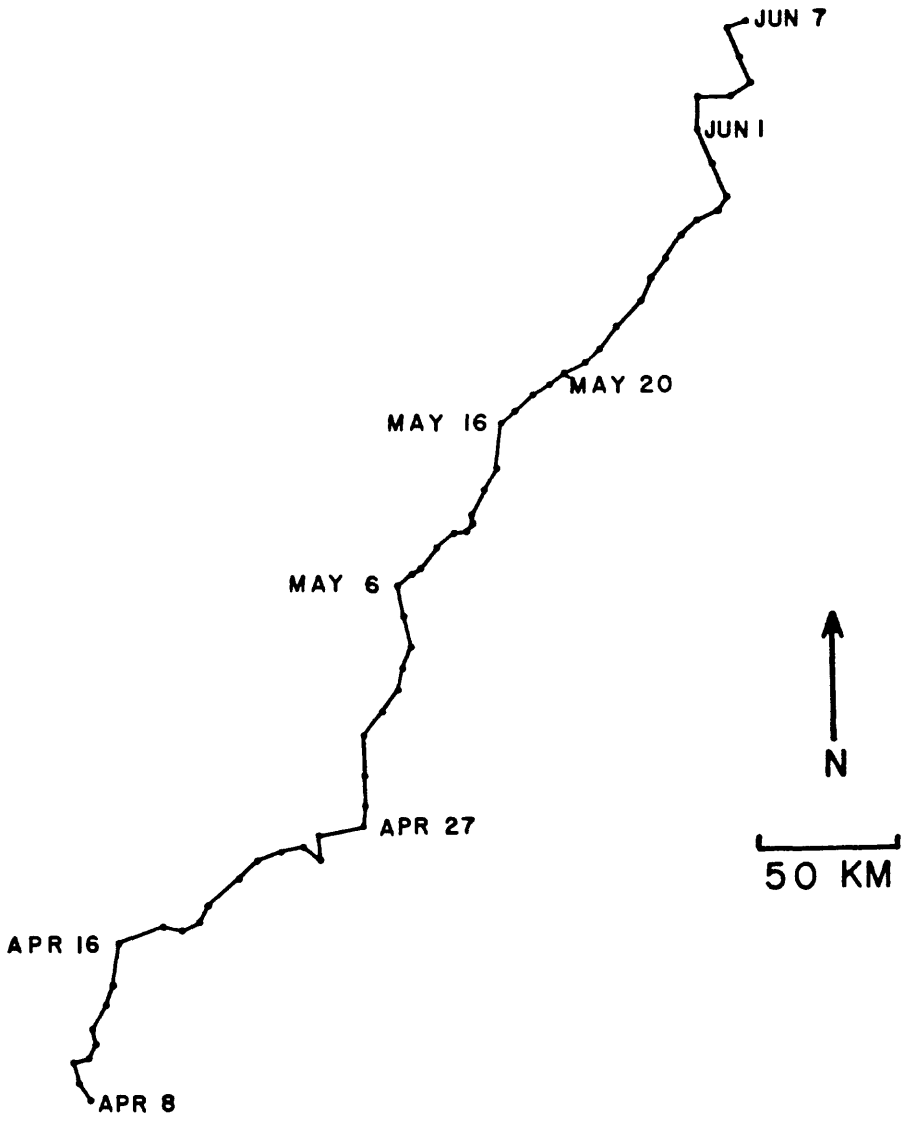

Figure 29. Daily mean wind vectors measured at Long Beach Airport.

by waves and other processes in shallow water. Much of the TSM settles out of the water column as it crosses the central shelf, never reaching the shelf break, on the broad section of shelf between San Pedro Sea Valley and San Gabriel Canyon (Fig. 17). This, in part, explains the rocky outcrops and coarser sediment found on the outer shelf in this region. The finest particles advected to the shelf break are winnowed from the bottom sediment and dispersed by current activity at the shelf break. In contrast, high concentrations of TSM blanket the entire segment of shelf between San Gabriel Canyon and Newport Canyon (Fig. 17). The higher rates of deposition account for the finer-grained surface sediment and thicker accumulations of unconsolidated sediment on the shelf and slope and in and around Newport Canyon. This segment of the shelf and slope would presumably be an important sink for pollutants as well.

The measurements of low frequency motions near the sea floor at both Geoprobe sites suggest that over the approximately 40 days during fair weather the net transport of near-bottom suspended matter materials is offshore, with a slightly higher transport rate at the deeper site. Measured offshore velocities are about 3.1 cm/s and 0.4 cm/s at G1B and G2, respectively. Evidence of Ekman veering within the bottom 1 m of the water column is apparent in the Geoprobe velocity data; this veering will require an integrated estimate of flow direction in the bottom layer to represent more accurately the transport paths of suspended materials.

Weatherly (1977) measured Ekman veering in the Straits of Florida from current meter data taken 1 m and 3 m above the sea floor; mean veering was about 10° and maximum veering was about 27°. Our data suggest a veering of 10° to 20° between 20 cm and 1 m above the bottom at both shelf sites. Weatherly (1977) also shows that the thickness (D) of the bottom Ekman layer can be estimated from the velocity shear (u_*) as:

$$D = 0.4 \frac{u_*}{f}$$

where f is inertial frequency (8.13×10^{-5} sec $^{-1}$). For a daily average u_* of 0.5 cm/s (see below), D = 24 m. This estimate of layer thickness is consistent with the measured thickness of the turbid bottom layer (Fig. 13).

The potential importance of internal waves in transport of near-bottom sediment on continental shelves has been discussed by Lafond (1961) and Cacchione and Southard (1974) and Cacchione et al. (1976). Bottom currents due to internal waves were present at both Geoprobe sites. These currents were superimposed on tidal and other lower frequency motions. Although the internal wave-induced velocities were less than 15 cm/s at 1 m above the bottom, the bottom-stresses which they cause are additive to the stresses from the other major fluid motions. Cacchione and Southard (1974) provide a technique for estimating the largest sediment sizes (i.e., largest diameters, D_i) that can be moved by internal waves of amplitude, a_o, and frequency, ω, on a continental shelf.

$$D_i/a_o = K \omega^{1.5} / c \; h/h_o.$$

$c^2 = \frac{\omega^2 - f^2}{N^2 - \omega^2}$; N is the Brunt - Vaisala or stability frequency; f is inertial frequency; h is local water depth; h_o is depth at the shelf edge, and K is a dimensional constant ($K \simeq 2.8 \times 10^{-3}$). N can be calculated from the formula:

$$N^2 = \left(\frac{g}{\bar{\rho}} \frac{d\rho}{dz} \right)^{1/2}$$

$\bar{\rho}$ is mean water density and $d\rho/dz$ is the vertical density gradient.

We found internal waves of several frequencies in our spectral analysis of currents. If we select typical internal wave periods, T, of 24 minutes and 6 hours for G1A and G2, respectively, then the following parameters can be estimated:

	G1A	G2
T	24 min.	6 hrs.
ω	4.36×10^{-3} sec^{-1}	2.91×10^{-4} sec^{-1}
N	2.12×10^{-2} sec^{-1}	1.16×10^{-2} sec^{-1}
C	0.211	0.024
D_i/a_o	1.3×10^{-5}	7.01×10^{-7}

The D_i/a_o values indicate that for internal waves of 5 m amplitudes, D_i would be 6.5×10^{-2} mm and 3.5×10^{-3} mm at G1A and G2, respectively. These estimates of the larges diameters that can be moved by 5 m internal waves of measured frequencies suggest that this process is not, by itself, significant for initial motion of bottom materials. The presence of these internal waves, however, can have significant effects on transport of suspended materials as discussed by Cacchione et al. (1976).

The highest frequency motions present in our data, surface waves, have their most important effects at shallower locations on the shelf. The maximum wave stress on the bed at G1B can be estimated using the theoretical model for oscillation bottom stress given by Smith (1977). With wave periods of 12 seconds, maximum wave speed at the bottom of 20 cm/s, and an estimated bed roughness of 0.1 cm, the maximum shear velocity is about 2.7 cm/s. This wave-induced shear velocity is high enough to cause sediment entrainment and to form wave-generated ripples. This result agrees with bottom photographs at G1A and at other shallow (<30-40 m) sites on the San Pedro shelf.

Bottom currents due to surface waves propagating over continental shelves can produce bedforms and initiate bottom sediment movement in relatively deep water (Komar et al., 1972). The effectiveness of these waves in disturbing the bottom sediments depends primarily on the wave heights and wave periods. During the 40 day experiment fair weather prevailed over the San Pedro shelf area, and close examination of the burst pressure records from G1B shows that wave heights were low to moderate (<2 m). However, low amplitude, long period swells propagating from the west to southwest were observed during both cruises. These swells are easily seen in the burst pressure data, particularly in Figure 26. The waves are typically smooth indulations in the pressure record, corresponding to a smooth, regular oscillation of the sea surface. Typical swell periods were 12 to 14 seconds; typical swell heights were 0.5 to 1.5 meters (Appendix E).

To evaluate the intensity and variability of the wave currents over the 40 day experiment, the variance in the burst current data was calculated for each tripod and is shown in Figure 28. The variance in each burst is related to the kinetic energy in the fluctuating part of the currents; i.e., the energy in the wave-induced motions at each sensor level. The square root of the variance values in Figure 28 is essentially the r-m-s wave current for each sensor. The variance in the burst pressure data is related to the bottom pressure fluctuations and has not been converted to wave height estimates. The pressure variance in indicative of changes in wave height and/or wave period.

Two striking features are evident in Figure 30. (1) Although local winds were generally light to moderate, the wave currents at G1B were significantly

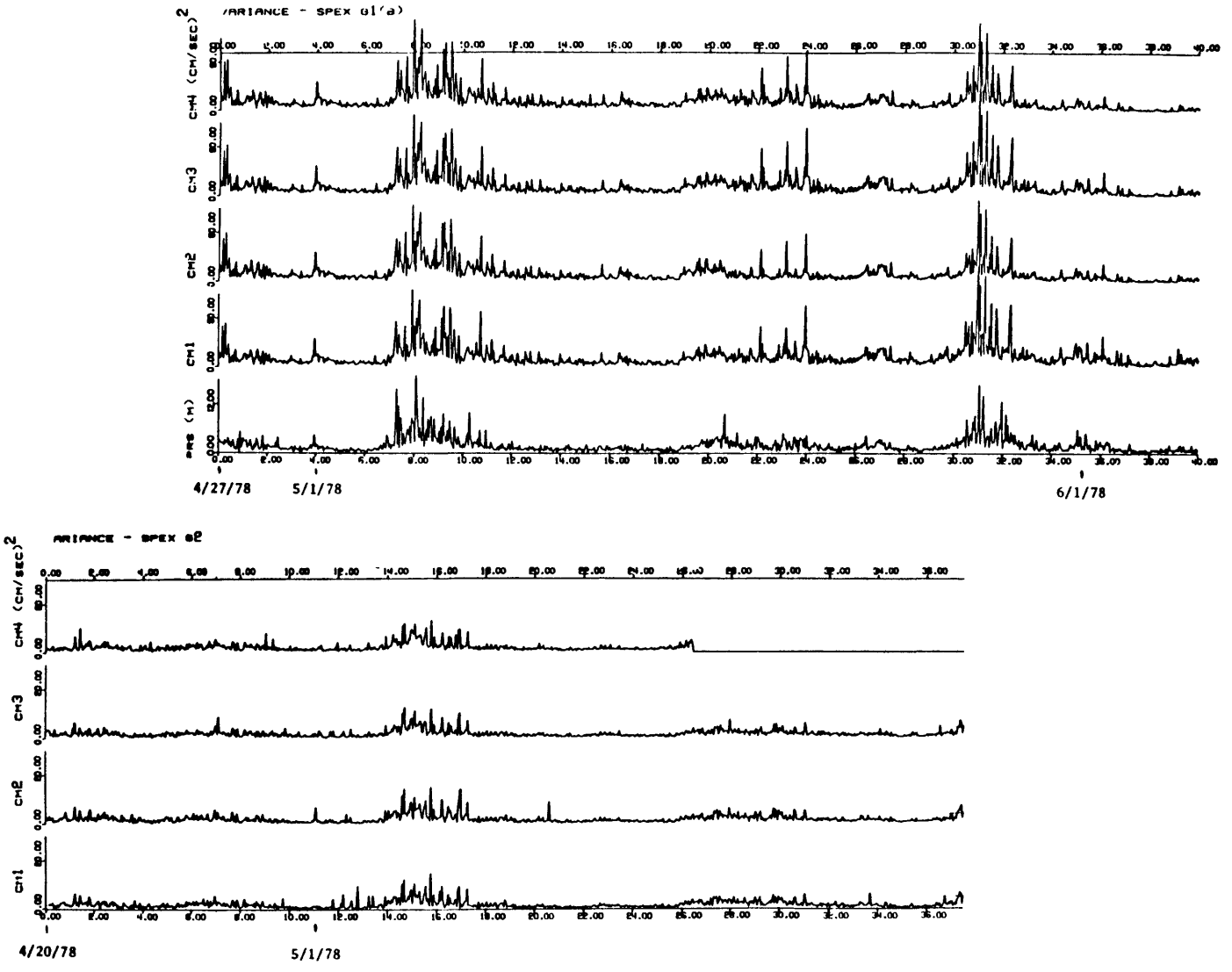

Figure 30. Variance in burst speed data for each e-m sensor from G1B (top) and G2 (bottom). Horizontal axis is days.

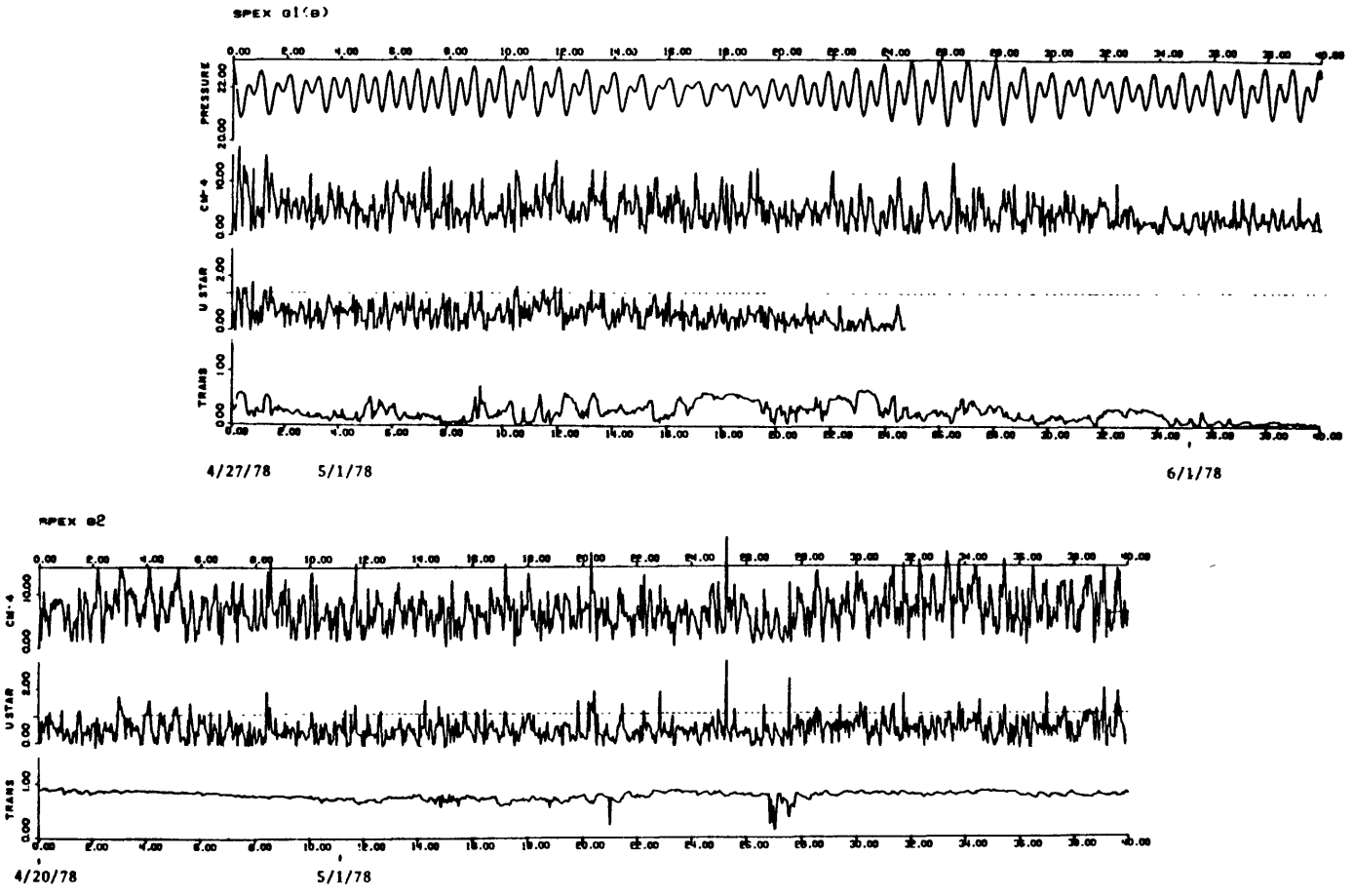

Figure 31. Pressure in meters; current speed (CM4) in cm/s at upper e-m; shear velocity (u_*) in cm/s; and light transmission (trans) in relative units for G1B (top) and G2 (bottom). Horizontal axis is days. Note: u_* was calculated from speed profiles measured with e-m sensors. The critical shear velocity/u_{*c}) needed to initiate sediment movement at each site is indicated by a heavy line on the u_* axis. For G1B, u_{*c} = 1.4 cm/s; for G2, u_{*c} = 1.0 cm/s.

energetic during several periods, particularly during May 4-8 and May 27-30. The r-m-s fluctuating currents during these periods were 12-14 cm/s at G1B, suggesting that wave currents were high enough to induce bottom sediment movement during those periods (Komar et al., 1972). (2) The deeper site had relatively low wave energy throughout the record except for a marked increase during the May 4-8 period. RMS speeds were less than 4.5 cm/s during that time, indicating that these waves could not, by their own action, transport bottom sediment and form ripple marks.

Sediment data taken previously (Karl, 1976) at the Geoprobe sites indicate that the mean sizes are about 0.3 mm and 0.10 mm at G1B and G2, respectively. Sternberg (1972) and others have shown that mean sizes correspond to a critical shear velocity, u_{*_c} , that is necessary for bottom sediment motion to occur. The u_{*_c} values for sediments at G1B and G2 are 1.4 cm/s and 1.0 cm/s, respectively. Figure 29 contains the computed u_* values based on the velocity profiles measured with the e-m current sensors on each tripod. One u_* value is computed and plotted for each burst. The technique for the u_* computations is described by Cacchione and Drake (1979). It should be noted here that the u_* values do not include the effects of wave stresses (i.e., burst averages have been used in the computations). The additional effect of waves will be small except during May 4-8 and May 27-30 at G1B.

The u_* values suggest that $u_* < u_{*_c}$ is typical over most of the record, with some short periods of $u_* \geq u_{*_c}$. Bottom sediment is generally not being moved by the hourly-averaged currents at the Geoprobe sites, except at times when $u_* \geq u_{*_c}$.

Figure 29 also shows pressure (G1B only), current speed (CM-4) and light transmission for each tripod. The u_* record is similar to the current record at CM-4, not a surprising result since the current speeds are used to compute u_*.

CONCLUSIONS

Observations of numerous oceanic parameters over forty days of early spring, fair-weather conditions clearly reveal the complex sediment dynamics of the continental shelf. Surface waves, internal waves, and tides contribute to and are superimposed on a mean flow which also responds to meteorological forcing; these interact to produce the circulation system and sediment transport patterns characterizing San Pedro Bay. Storms, which were not encountered during the experiment, would substantially modify the fair-weather system observed by us and described in the following paragraphs.

No single process dominates sediment transport on San Pedro shelf in the way, for instance, that tides control deposition in Cook Inlet, Alaska or that large surface waves predominate on the Oregon and Washington shelf. Instead, several processes are more or less in balance with one another. The relative importance of these processes, however, varies spatially and temporally. For example, shoaling surface waves affect bottom sediments more in shallow water than deep water and concentrate more energy at points of convergence than divergence. Also, there are times when packets of more energetic waves approach the shelf, thereby intensifying bottom currents and making a proportionately greater contribution to incipient sediment movement than other processes. While these various processes can initiate sediment motion, we found that local coastal upwelling had the most profound effect onmean circulation, and hence, sediment dispersal in San Pedro Bay during our experiment.

Local wind direction seems to govern upwelling in San Pedro Bay. We observed that a shift in wind direction from southerly to southwesterly initiated upwelling.

Upwelled water moved onto the shelf in the vicinity of San Pedro Sea Valley and spread southeastward across the shelf. Before the onset of upwelling, suspended particulate matter was concentrated nearshore. As the upwelled water moved over the shelf, it advected suspended matter seaward, dramatically increasing TSM concentration in the surface and bottom layers. Water at mid-depth remained clear, and, although uncertain of direction, we suspect water in this layer moved at some angle shoreward. In Figure 32, we schematically depict our conception of circulation and sediment dispersal during an upwelling event. At non-upwelling times, bottom transport would be southerly, directly off the shelf and the northwesterly drift shown near Huntington Beach might not exist. We do not know the direction of surface transport during the non-upwelling situation.

In effect, we conclude that contaminants released near the bottom, or those at the surface settling to the bottom, seaward of approximately the 20 m isobath, will move off the shelf. Pollutants will accumulate in San Pedro Sea Valley, San Gabriel Canyon and environs, Newport Canyon and on the segment of shelf between San Gabriel Canyon and Newport Canyon. Those particles not accumulating on the bottom will be dispersed by currents in San Pedro Channel.

Fair-weather conditions in San Pedro Bay pose little, if any, threat to drilling rig or pipe line construction. However, areas of wave convergence and possibly unstable sediment accumulations at the heads of submarine canyons and on the upper slope could be potentially hazardous; but we did not evaluate these situations. Storms are capable of causing severe damage and must be taken into account.

We emphasize that our conclusions are valid only for the fair-weather, spring-time regime prevalent during the experiment. In order to predict confidently pathways of pollutant dispersal, we recommend that similar instrument arrays be maintained on the shelf for a period greater than one year. Data from a long-term experiment could then be used to develop or to test computerized numerical models. These models could then be applied to other shelf segments.

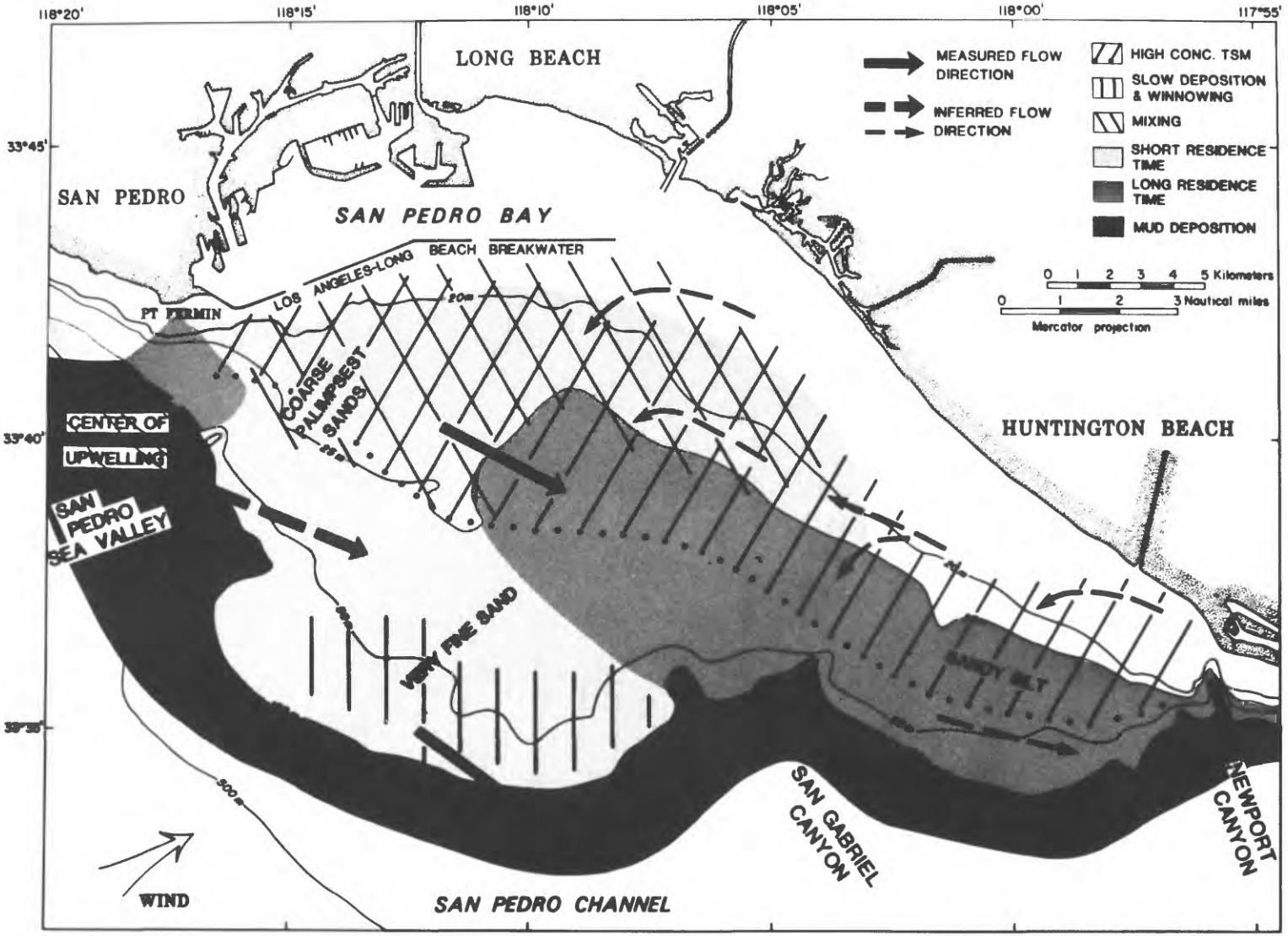

Figure 32. Conceptual model of near-bottom current systems, direction of sediment transport, particle residence time and sites of accumulation during an upwelling event. Length of arrows does not indicate relative current speeds.

REFERENCES

Bartz, R., J. R. V. Zaneveld and H. Pak, preprint, A transmissometer for profiling and moored observations in water: Proceedings of the Society of Photo-Optical Instrumentation Engineers, 7 p.

Brink, K. H., D. Halpern and R. L. Smith, 1978, Circulation in Peruvian Coastal upwelling system near 15°S (abs.): EOS American Geophysical Union Transaction, San Francisco, CA., v. 59, no. 12, p. 1103.

Bunnell, V. D., 1969, The water structure of the San Pedro Basin, California Borderland: unpub. M.S. thesis, Univ. Southern California, Los Angeles, California, 127 p.

Butman, B., M. Noble, and D. W. Folger, 1979, Long-term observations of bottom current and bottom sediment movement on the mid-Atlantic continental shelf: Jour. Geophysical Res., v. 84, no. C3, p. 1187-1205.

Cacchione, D. A., D. E. Drake, J. D. Dingler, C. D. Winant, and J. R. Olson, 1976, Observations of sediment movement by surface and internal waves off San Diego, California (abs.): Am. Geophys. Union Trans., v. 58(5), p. 307.

Cacchione, D. A. and D. E. Drake, 1979, A new instrument system to investigate sediment dynamics on continental shelves, Mar. Geol., v. 30, p. 299-312.

Cacchione, D. A. and J. B. Southard, 1979, Incipient sediment movement by shoaling internal gravity waves: Jour. Geophys. Res., v. 70, p. 2237-2242.

Cairns, J. L., 1968, Thermocline strength fluctuations in coastal waters: Jour. Geophys. Res., v. 73, p. 2591-2595.

Caldwell, J. M., 1956, Wave action and sand movement near Anaheim Bay, California: U.S. Army Corps of Engineers, Beach Erosion Board, Tech. Memo. 68, 21 p.

Davis, R. and R. Weller, preprint, Propeller current sensors: preprint volume, "Instruments and methods in air-sea interaction", NATO School, Ustaoset, Norway, April, 1978, 12 p.

Douglas, R. G., M. L. Cotton and L. Wall, 1979, Distributional and variability analysis of benthic foraminifera in the Southern California Bight, BLM southern California benthic program, vol. II, rpt. 21.0; Washington, D.C., Bureau of Land Management.

Emery, K. O., 1960, The sea off southern California: John Wiley and Sons, Inc., New York, 366 p.

Felix, D. W. and D. S. Gorsline, 1971, Newport Submarine Canyon, California: an example of the effects of shifting loci of sand supply upon canyon position: Marine Geology, v. 10, p. 177-198.

Fischer, P. J., R. W. Berry and W. E. Reed, 1976, Southern California Bight, sediment characterization and analysis for the Bureau of Land Management Baseline Study; unpub. rept., California State University at Northridge, 164 p.

Godin, G., 1972, The Analysis of Tides, University of Toronto Press, 264 p.

Gorsline, D. S. and D. J. Grant, 1972, Sediment textural patterns on San Pedro shelf, California (1951-1971): reworking and transport by waves and currents: in Swift, D.J.P., D. B. Duane and O. H. Pilkey, (eds.), Shelf sediment transport: Process and Pattern, Dowden, Hutchinson and Ross, Inc., Stroudsbourg, Pa., p. 575-600.

Greene, H. G., Field, M. E. and Clarke, S., in preparation, Geologic Hazards in the southern California continental borderland.

Hendricks, T., 1976a, Current velocities required to move sediments: in Southern California Coastal Water Research Project Annual Report 1976, p. 71-76.

Hendricks, T., 1976b, Measurements of subthermocline currents: in Southern California Coastal Research Project Annual Report 1976, p. 63-70.

Horrer, P. L., 1950, Southern hemisphere swell and waves from a tropical storm at Long Beach, California: U.S. Army Corps of Engineers, Beach Erosion Board Bulletin, v. 4, no. 3, p. 1-18.

Inman, D. L. and J. D. Frautschy, 1966, Littoral Processes and the development of shorelines: Coastal Eng. Santa Barbara Specialty Conference, New York, Am. Soc. Civil Eng., p. 511-536.

Karl, H. A., 1975, Distribution and significance of sedimentary structures and bedforms on the continental shelf, southern California (abs.): Geol. Soc. America Abstracts with programs, v. 7. no. 3, p. 331-332.

Karl, H. A., 1976, Processes influencing transportation and deposition of sediment on the continental shelf, southern California: unpub. Ph.D. dissertation, Univ. Southern California, Los Angeles, California, 331 p.

Karl, H. A., 1980a, Influence of San Gabriel Submarine Canyon on narrow shelf sediment dynamics, southern California: Marine Geology, v. 34, p. 61-78.

Karl, H. A., 1980b, Speculations on processes responsible for mesoscale current lineations on the continental shelf, southern California: Marine Geology, v. 34, p. M9-M18.

Komar, P. D., P. H. Hendeck, and L. K. Kulm, 1972, Observations and significance of deep-water oscillatory ripple marks on the Oregon continental shelf: in D.J.P. Swift, D. B. Duane, and O. H. Pilkey, eds., Shelf Sediment Transport. Dowden, Hutchinson, and Ross, Stroudsburg, Pa., p. 601-620.

LaFond, E. C., 1961, Internal wave motion and its geological significance: in "Mahodevan Volume", Osmania University Press, p. 61-77.

Lee, O. S., 1961, Observations on internal waves in shallow water: Limnol. Oceanogr, v. 6, p. 312-321.

Moore, D. G,1951, Submarine geology of San Pedro shelf, California: unpub. M.S. thesis, Univ. Southern California, Los Angeles, California.

Moore, D. G., 1954, Submarine geology of San Pedro shelf: Jour. Sed. Petrology, v. 24, p. 162-181.

O'Brien, J. J., D. Halpern, and R. L. Smith, 1978, Determining vertical velocity on the continental shelf (abs.): EOS American Geophysical Union, Transactions, San Francisco, CA., v. 59, no. 12, p. 1096.

O'Brien, M. P., 1950, Wave refraction at Long Beach and Santa Barbara, Calif.: U.S. Army Corps of Engineers, Beach Ersion Board Bull., v. 4, no. 1, p. 1-11.

Pirie, D. M., M. J. Murphy, and Edmiston, 1975, California nearshore surface urrents: Shore and Beach, Oct. 1975, p. 23-24.

Smith, J. D., 1977, Modeling of sediment transport on continental shelves: in E. D. Goldberg, I. N. McCave, J. J. O'Brien, and J. H. Steele, eds., The Sea: vol. 6, Marine Modeling. Wiley-Interscience, New York, p. 539-578.

Smith, J. D. and T S. Hopkins, 1972, Sediment transport on the continental shelf off of Washington and Oregon in light of recent current measurements: in D.J.P. Swift, D. B. Duane, O. H. Pilkey (eds.), Shelf Sediment Transport: Process and Pattern, Dowden, Hutchinson and Ross, Inc., Stroudsburg, Pa., p. 83-97.

Sternberg, R. H., 1972, Predicting initial motion and bedload transport of sediment particles in the marine environment: in D.J.P. Swift, D. B. Duane, and O. H. Pilkey, eds., Shelf Sediment Transport, Dowden, Hutchinson and Ross, Stroudsburg, Pa., p. 61-82.

Vernon, J. W., 1966, The Shelf Sediment Transport System: unpub., M.S. thesis, Univ. of Southern California, Los Angeles, CA., 135 p.

Weatherly G. L., 1977, Bottom boundary layer observations in the Florida current: in Bottom Turbulence, Proc. of the 8th International Liege Colloquium on Ocean Hydrodynamics, Elsevier Oceanography Series, 19, p. 237-254.

APPENDIX A

Time-series analysis and plots of electromagnetic current meter data for upper (100 cm) and lower (20 cm) sensor from G1B (pages D-1 to D-12) and G2 (pages D-13 to D-24). Similar plots for the upper (100 cm) sensor on G1A are shown (pages D-25 to D-29).

Burst data represent burst averages as described in text.

STATISTICS AND HISTOGRAMS OF CURRENTS AT CM4 - SPEX 1B 1978
LOCATION = LAT 33 40N, LONG 118 12W, DEPTH = 21 METERS
OBSERVATION PERIOD = 0000 27 APR 78 TO 2300 5 JUN 78 (40.0 DAYS)
N = 960 DT = 1.00 HOURS, UNITS = (CM/SEC)

	MEAN	VARIANCE	ST-DEV	SKEW	KURT	MAX	MIN
S	4.44	7.03	2.65	0.998	4.022	16.35	0.15
U	-0.33	15.24	3.90	0.019	3.322	13.23	-11.90
V	-0.28	11.33	3.37	-0.423	3.507	9.72	-13.82

S = SPEED
U = EAST-WEST COMPONENT OF VELOCITY, EAST =POSITIVE U
V = NORTH-SOUTH COMPONENT OF VELOCITY, NORTH = POSITIVE V

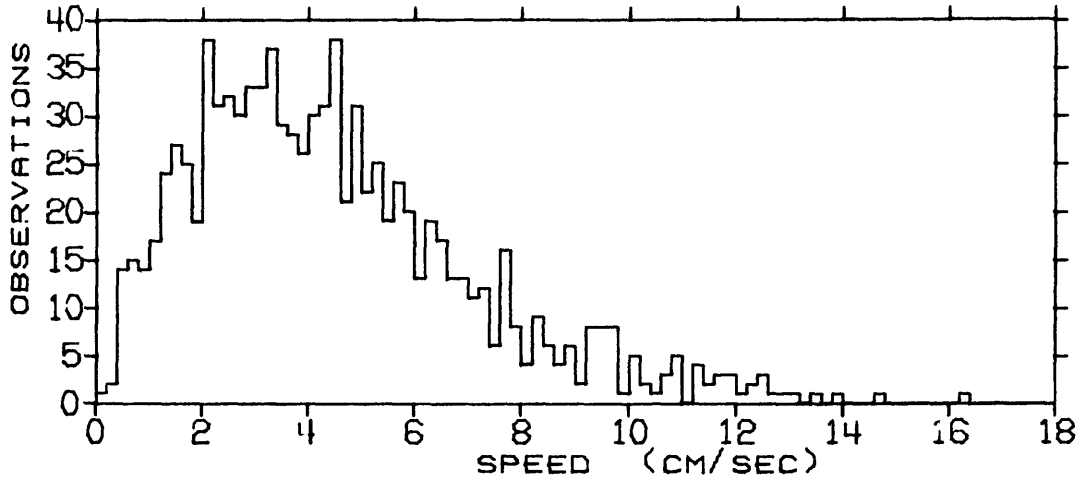

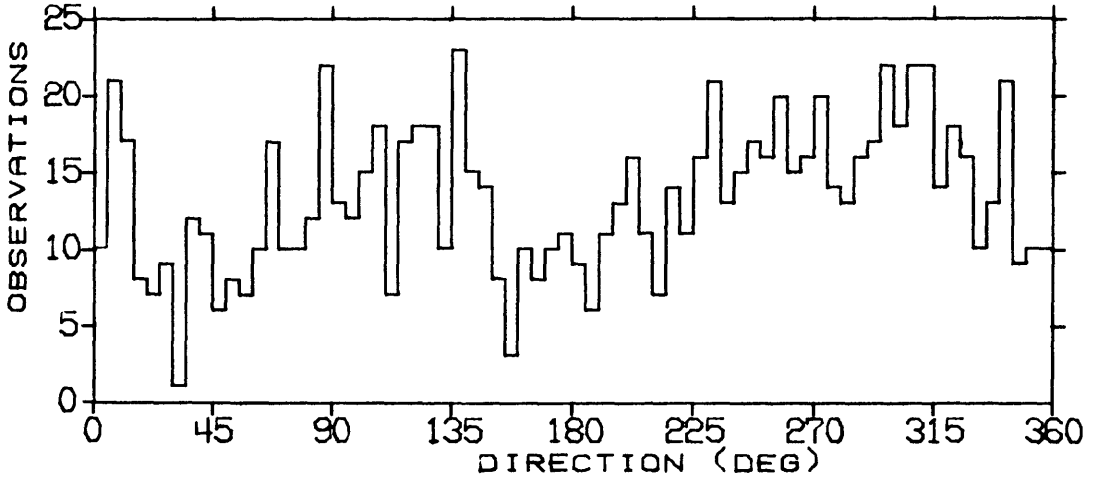

TIME SERIES OF VECTOR AVERAGED CURRENTS AT CM4 - SPEX 1B 1978
LOCATION = LAT 33 40N, LONG 118 12W, DEPTH = 21 METERS
OBSERVATION PERIOD = 0000 27 APR 78 TO 2300 16 MAY 78 (20.0 DAYS)
AVERAGING INTERVAL = 1.0 HOURS (1 POINTS)

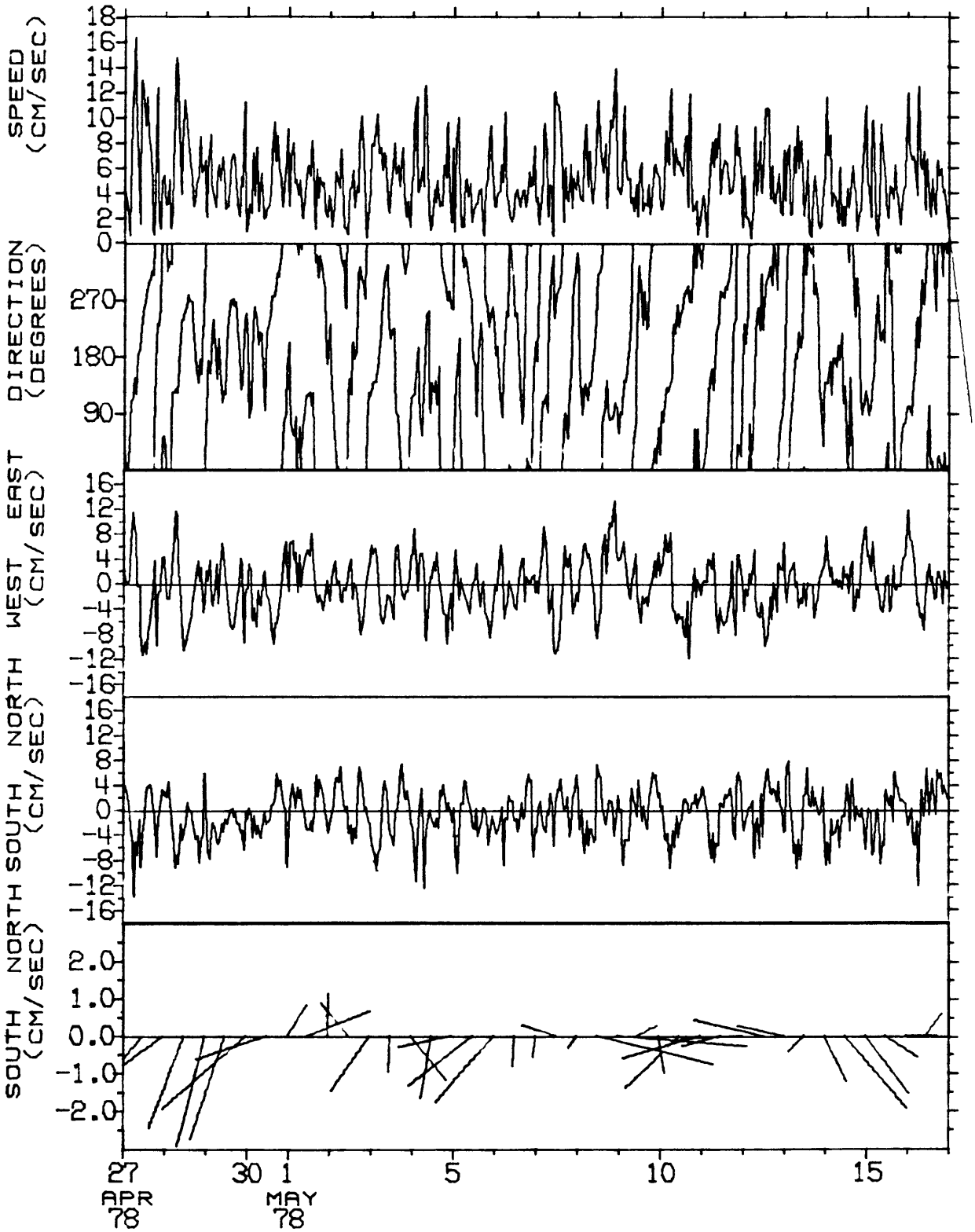

TIME SERIES OF VECTOR AVERAGED CURRENTS AT CM4 - SPEX 1B 1978
LOCATION = LAT 33 40N, LONG 118 12W, DEPTH = 21 METERS
OBSERVATION PERIOD = 0000 17 MAY 78 TO 2300 5 JUN 78 (20.0 DAYS)
AVERAGING INTERVAL = 1.0 HOURS (1 POINTS)

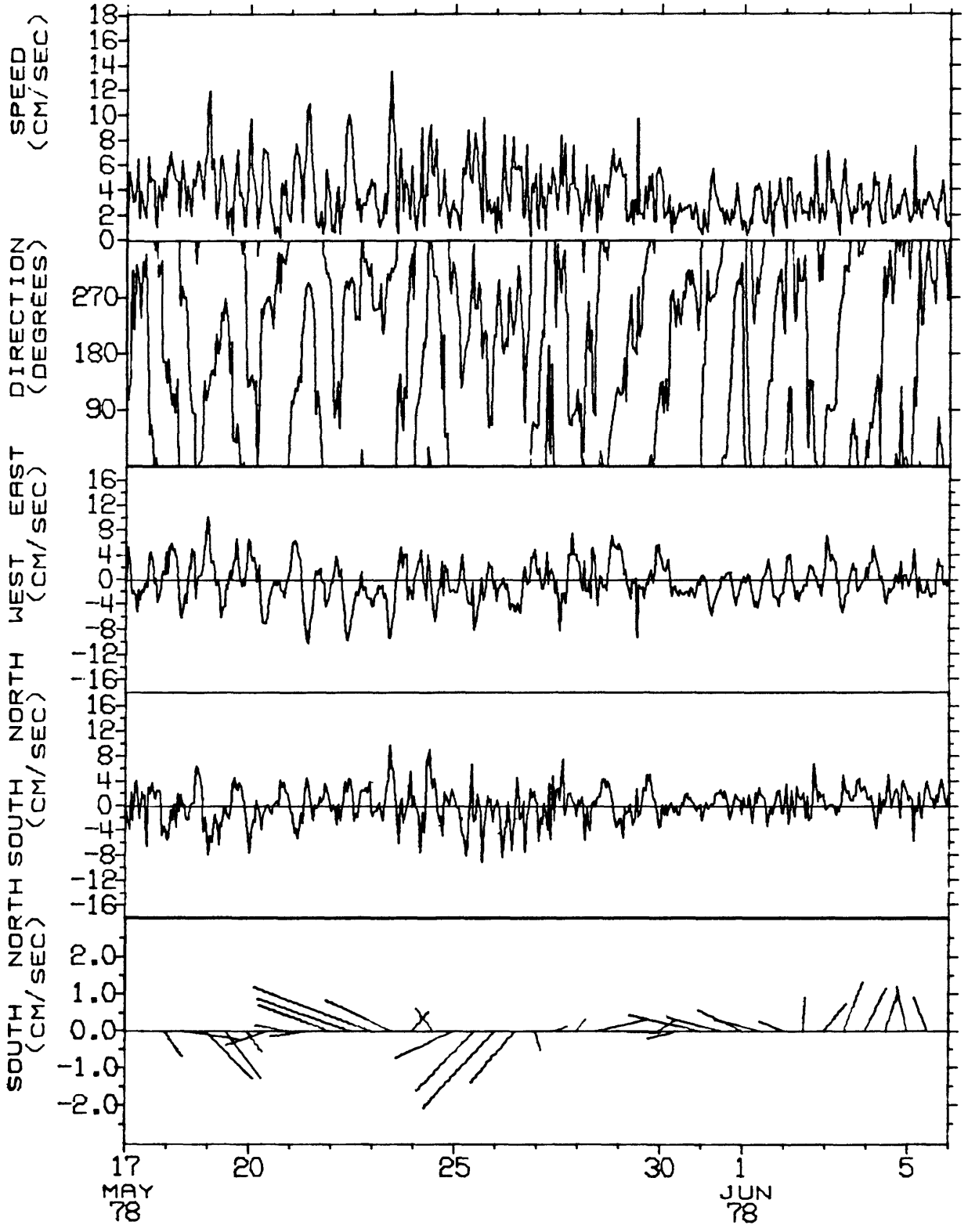

PROGRESSIVE VECTOR DIAGRAM OF CURRENTS AT CM4 - SPEX 1B 1978
LOCATION = LAT 33 40N, LONG 118 12W, DEPTH = 21 METERS
OBSERVATION PERIOD = 0000 27 APR 78 TO 2300 5 JUN 78 (40.0 DAYS)
* EVERY 1.0 DAYS BEGINNING AT 0000 27 APR 78

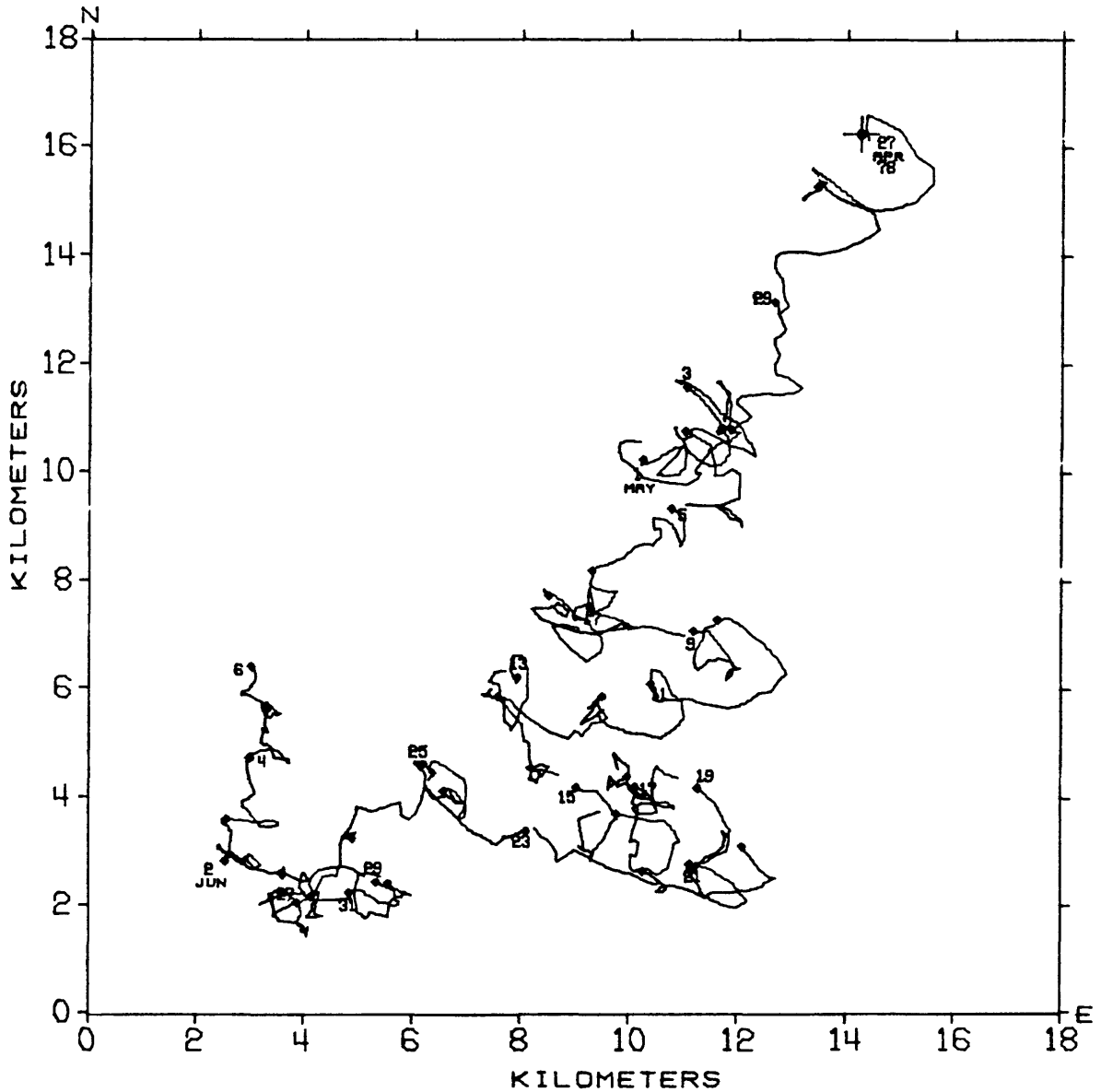

KINETIC ENERGY SPECTRUM OF CURRENTS AT CM4 - SPEX 1B 1978
LOCATION = LAT 33 40N, LONG 118 12W, DEPTH = 21 METERS
OBSERVATION PERIOD = 0000 27 APR 78 TO 2300 5 JUN 78 (40.0 DAYS)
N = 960, DT = 1.0 HOURS, SMOOTHING - DANIELL WINDOW

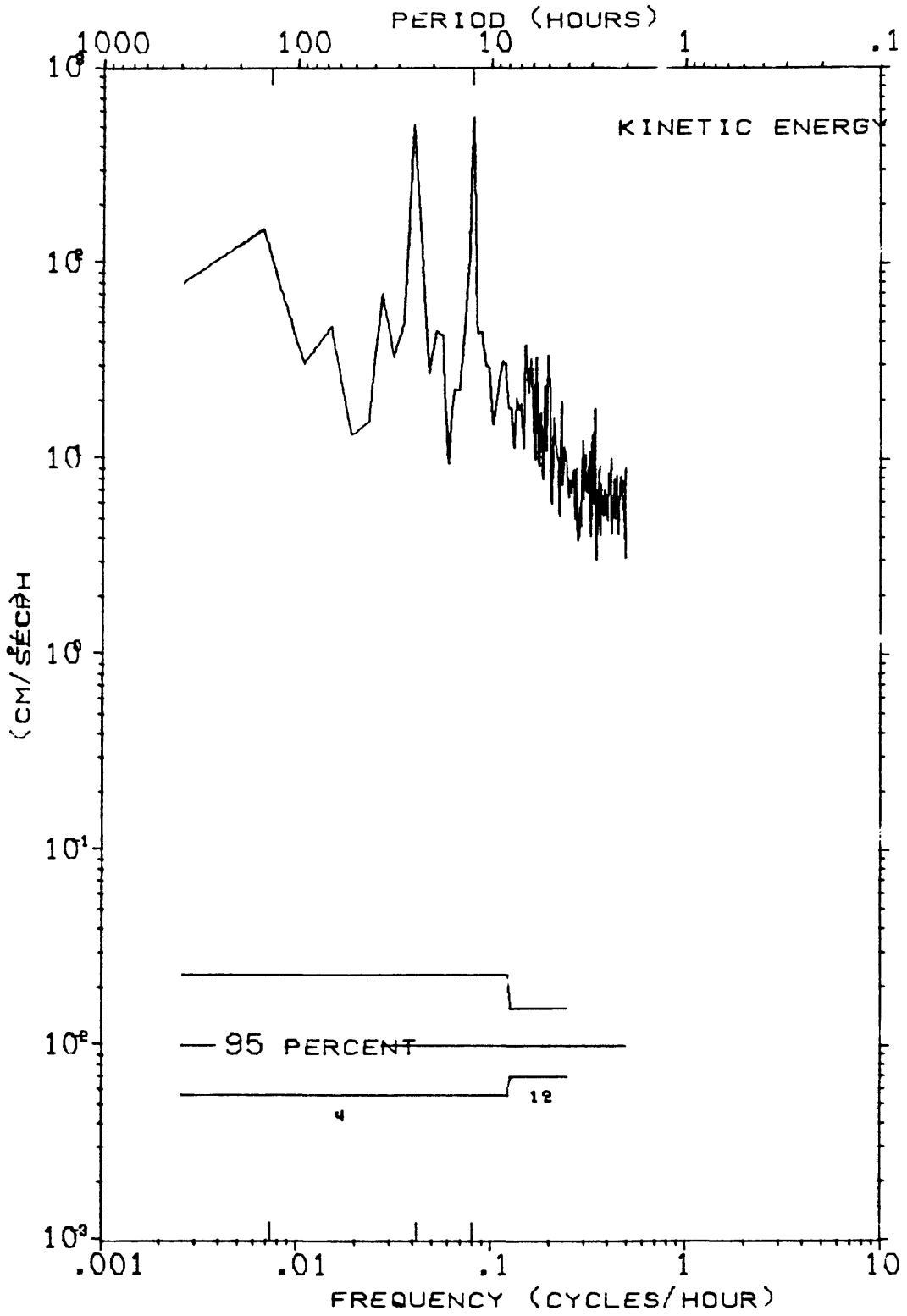

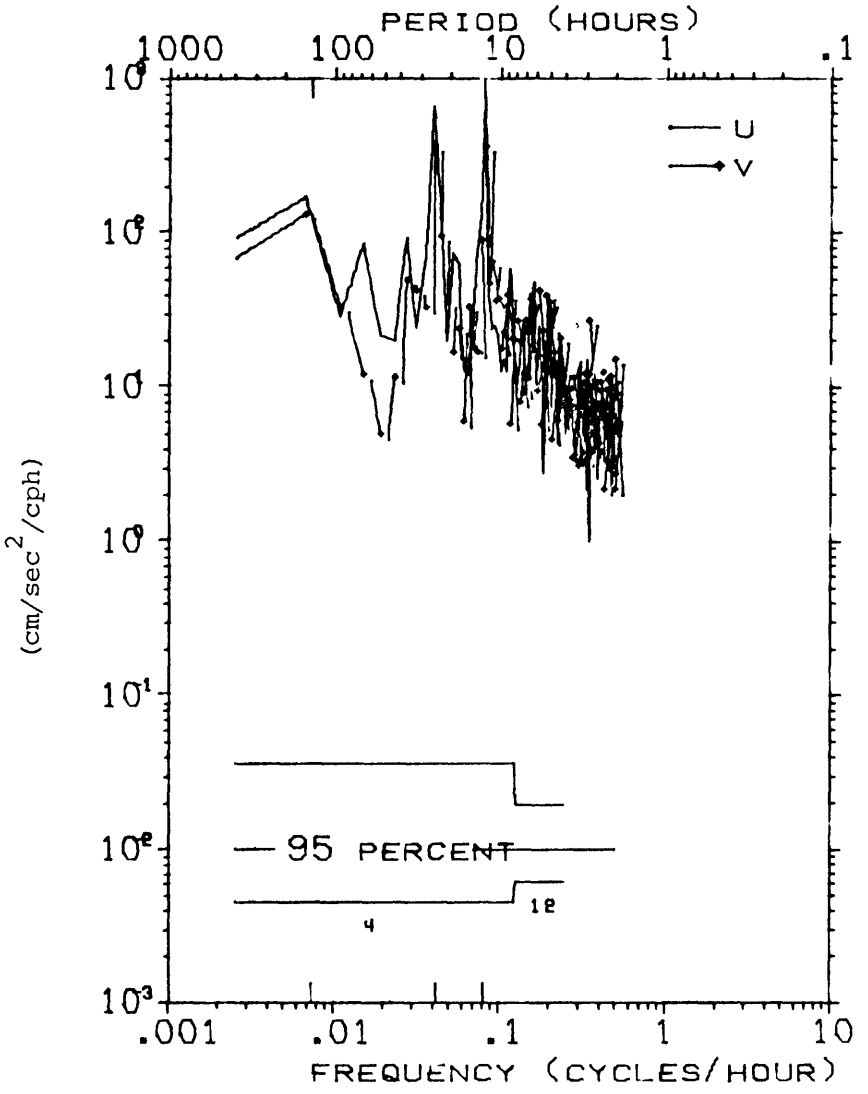

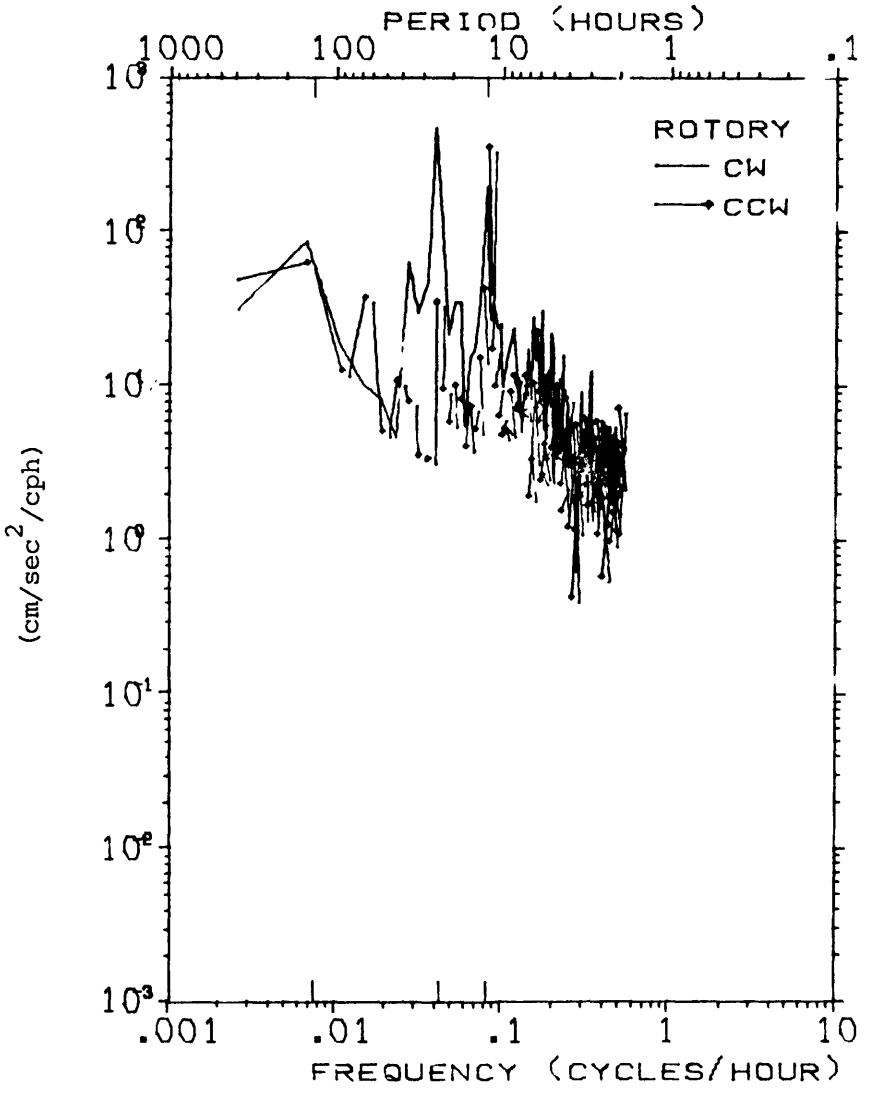

U, V AND ROTORY SPECTRA OF CURRENTS AT CM4 - SPEX 1B 1978
LOCATION = LAT 33 40N, LONG 118 12W, DEPTH = 21 METERS
OBSERVATION PERIOD = 0000 27 APR 78 TO 2300 5 JUN 78 (40.0 DAYS)
N = 960, DT = 1.0 HOURS, SMOOTHING - DANIELL WINDOW

STATISTICS AND HISTOGRAMS OF CURRENTS AT CM1 - SPEX 1B 1978
LOCATION = LAT 33 40N, LONG 118 12W, DEPTH = 21 METERS
OBSERVATION PERIOD = 0000 27 APR 78 TO 2300 5 JUN 78 (40.0 DAYS)
N = 960 DT = 1.00 HOURS, UNITS = (CM/SEC)

	MEAN	VARIANCE	ST-DEV	SKEW	KURT	MAX	MIN
S	3.07	3.97	1.99	1.272	4.828	12.34	0.04
U	0.19	6.75	2.60	0.236	3.707	9.43	-8.82
V	-1.15	5.27	2.29	-0.478	4.693	8.81	-10.48

S = SPEED
U = EAST-WEST COMPONENT OF VELOCITY, EAST =POSITIVE U
V = NORTH-SOUTH COMPONENT OF VELOCITY, NORTH = POSITIVE V

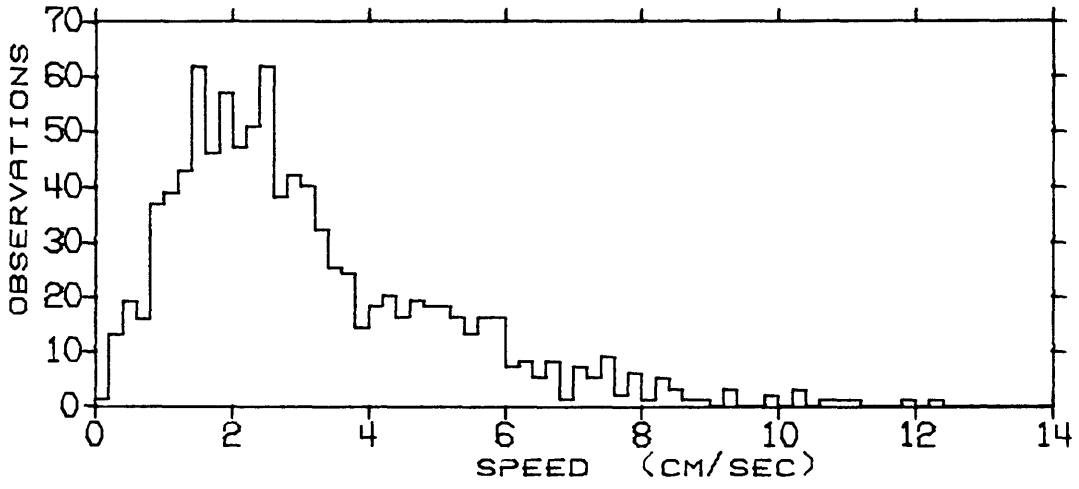

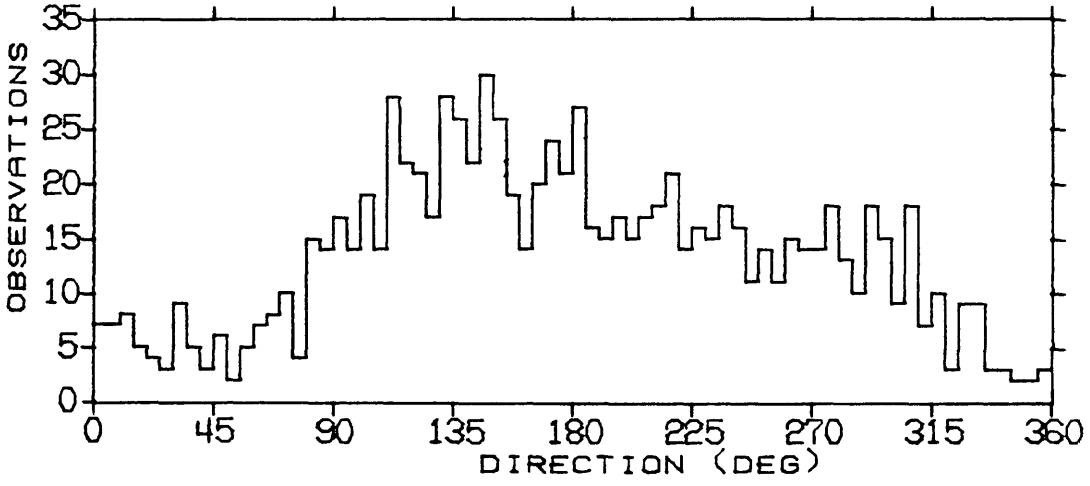

TIME SERIES OF VECTOR AVERAGED CURRENTS AT CM1 - SPEX 1B 1978
LOCATION = LAT 33 40N, LONG 118 12W, DEPTH = 21 METERS
OBSERVATION PERIOD = 0000 27 APR 78 TO 2300 16 MAY 78 (20.0 DAYS)
AVERAGING INTERVAL = 1.0 HOURS (1 POINTS)

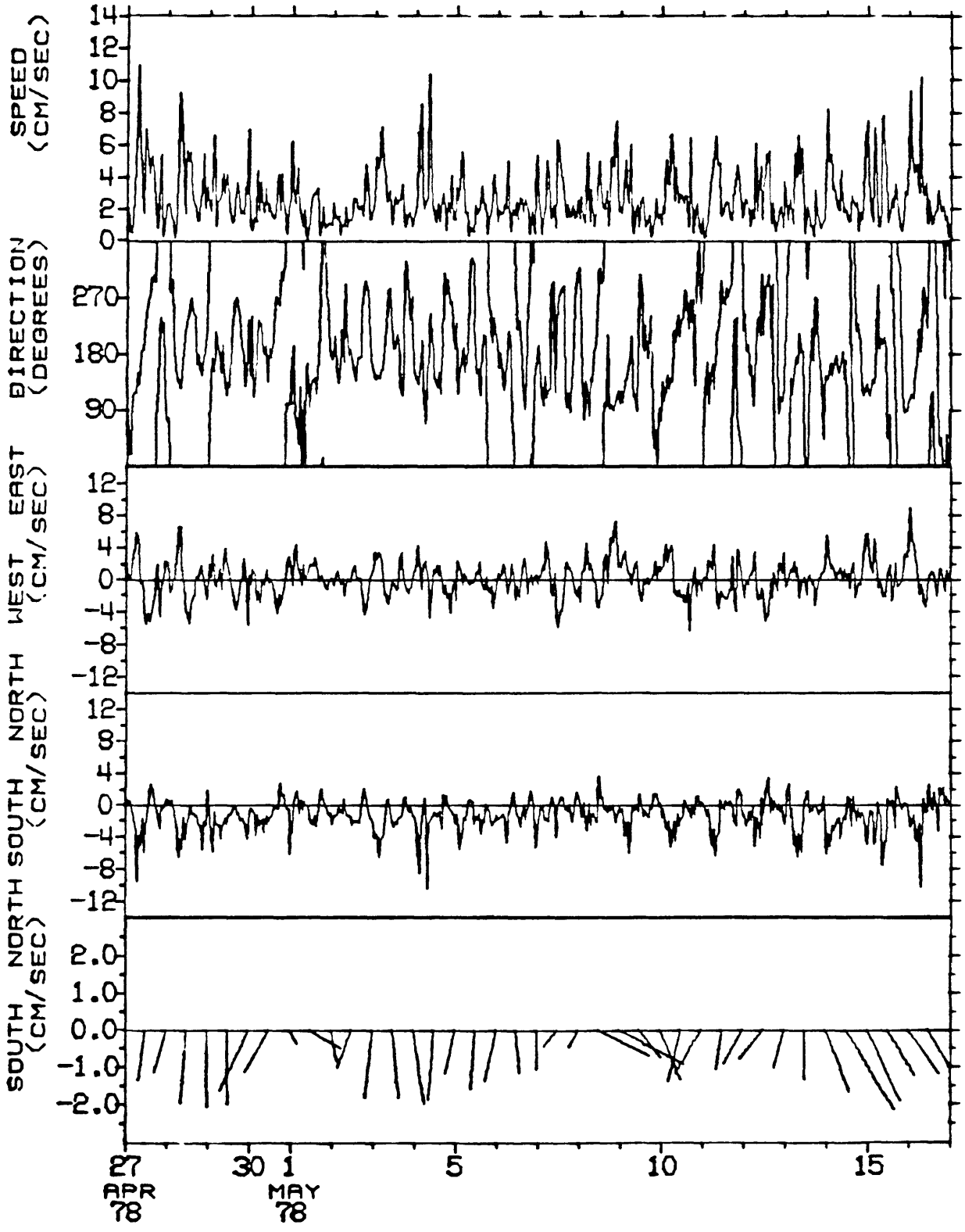

TIME SERIES OF VECTOR AVERAGED CURRENTS AT CM1 - SPEX 1B 1978
LOCATION = LAT 33 40N, LONG 118 12W, DEPTH = 21 METERS
OBSERVATION PERIOD = 0000 27 APR 78 TO 2300 16 MAY 78 (20.0 DAYS)
AVERAGING INTERVAL = 1.0 HOURS (1 POINTS)

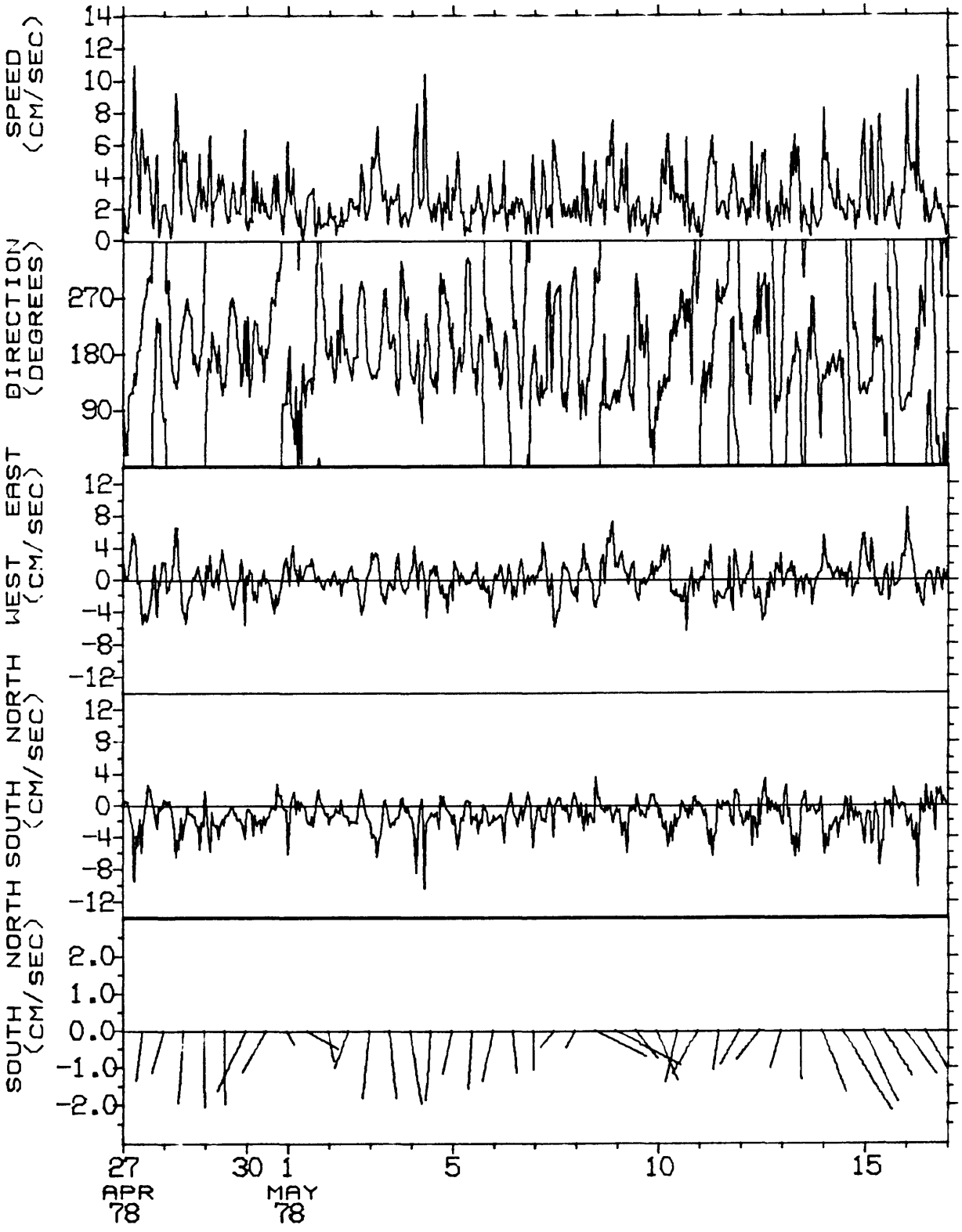

PROGRESSIVE VECTOR DIAGRAM OF CURRENTS AT CM1 - SPEX 1B 1978
LOCATION = LAT 33 40N, LONG 118 12W, DEPTH = 21 METERS
OBSERVATION PERIOD = 0000 27 APR 78 TO 2300 5 JUN 78 (40.0 DAYS)
* EVERY 1.0 DAYS BEGINNING AT 0000 27 APR 78

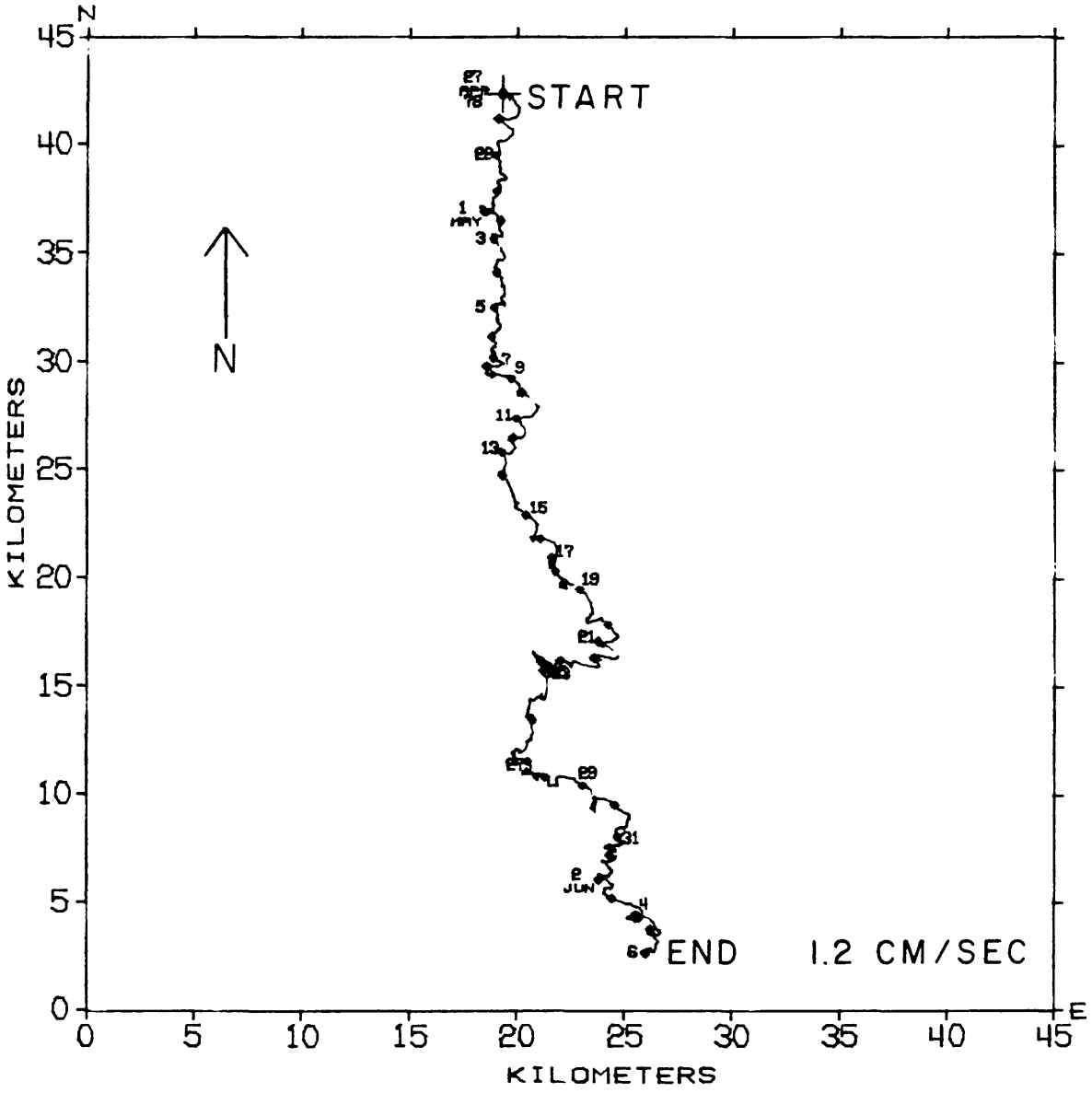

KINETIC ENERGY SPECTRUM OF CURRENTS AT CM1 - SPEX 1B 1978
LOCATION = LAT 33 40N, LONG 118 12W, DEPTH = 21 METERS
OBSERVATION PERIOD = 0000 27 APR 78 TO 2300 5 JUN 78 (40.0 DAYS)
N = 960, DT = 1.0 HOURS, SMOOTHING - DANIELL WINDOW

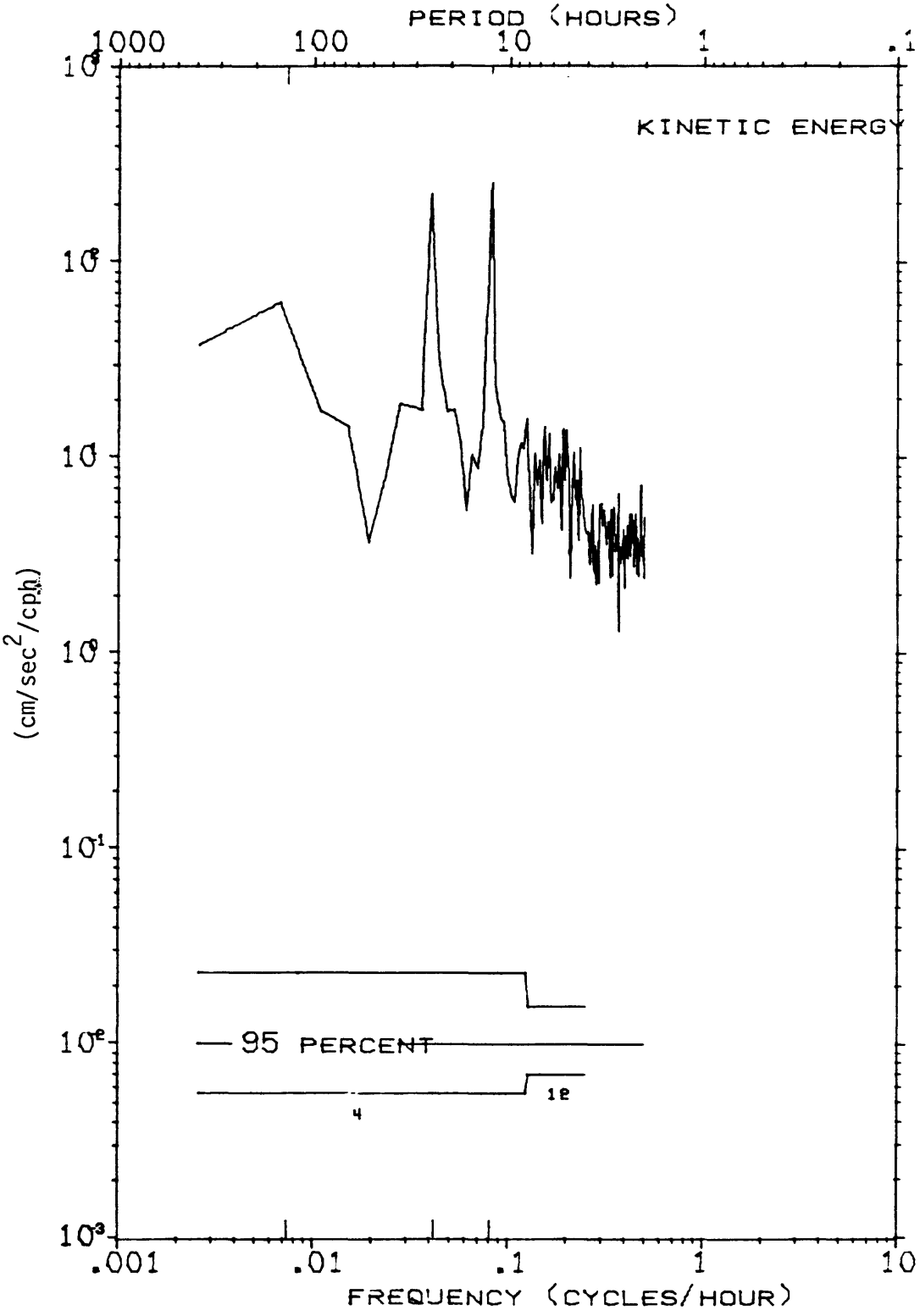

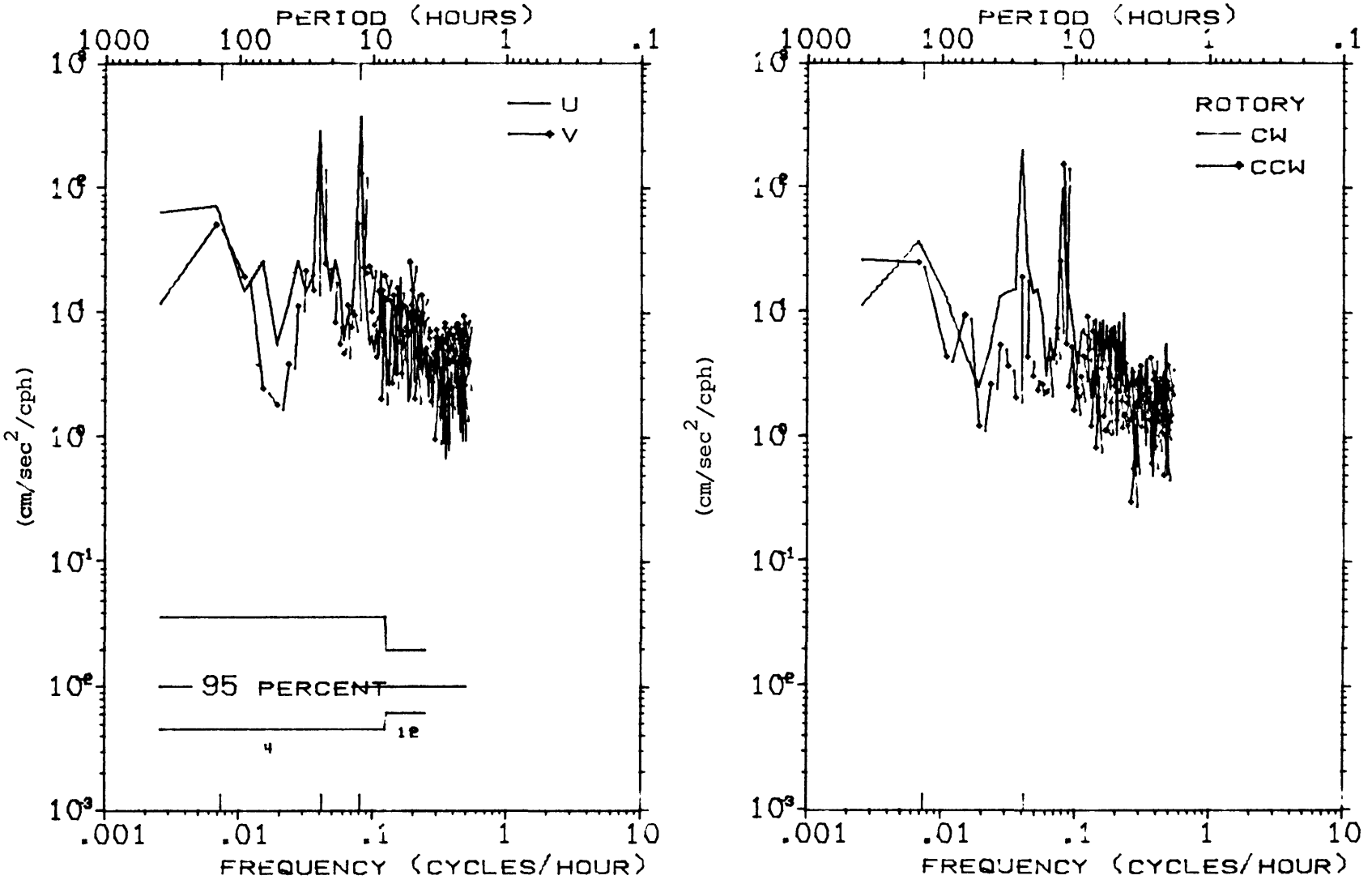

U, V AND ROTORY SPECTRA OF CURRENTS AT CM1 - SPEX 1B 1978
LOCATION = LAT 33 40N, LONG 118 12W, DEPTH = 21 METERS
OBSERVATION PERIOD = 0000 27 APR 78 TO 2300 5 JUN 78 (40.0 DAYS)
N = 960, DT = 1.0 HOURS, SMOOTHING - DANIELL WINDOW

STATISTICS AND HISTOGRAMS OF CURRENTS AT CM4 - SPEX G2 1978
LOCATION = LAT 33 35N, LONG 118 12W, DEPTH = 60 METERS
OBSERVATION PERIOD = 0000 20 APR 78 TO 2300 29 MAY 78 (40.0 DAYS)
N = 960 DT = 1.00 HOURS, UNITS = (CM/SEC)

	MEAN	VARIANCE	ST-DEV	SKEW	KURT	MAX	MIN
S	6.82	11.27	3.36	0.460	2.993	20.39	0.19
U	-1.24	28.36	5.33	0.140	3.137	19.02	-17.18
V	-2.30	22.62	4.76	0.300	2.648	11.83	-14.62

S = SPEED
U = EAST-WEST COMPONENT OF VELOCITY, EAST =POSITIVE U
V = NORTH-SOUTH COMPONENT OF VELOCITY, NORTH = POSITIVE V

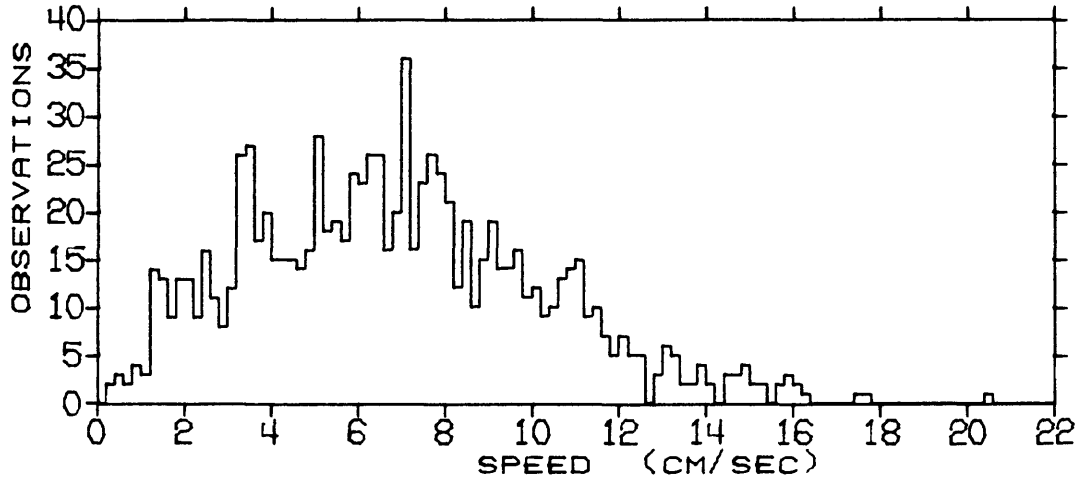

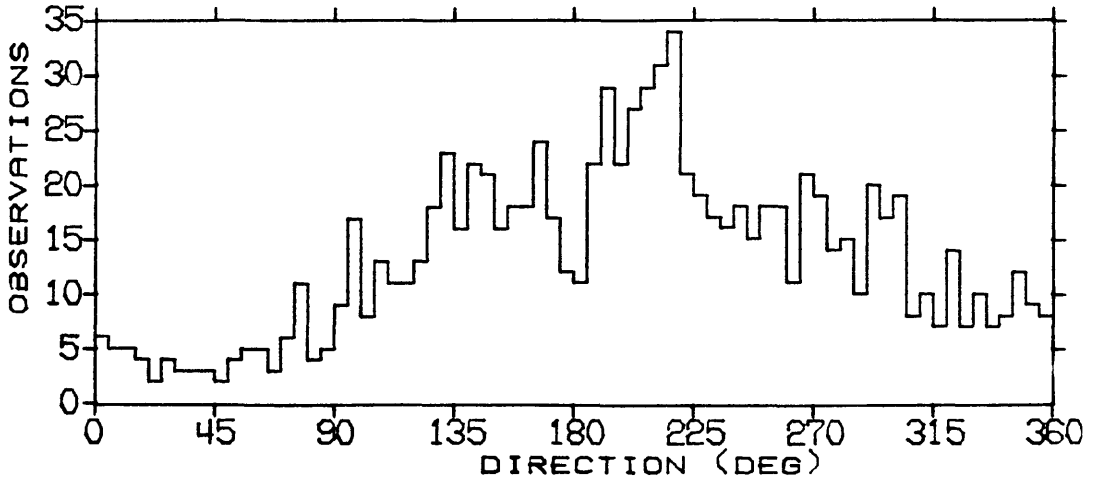

TIME SERIES OF VECTOR AVERAGED CURRENTS AT CM4 - SPEX G2 1978
LOCATION = LAT 33 35N, LONG 118 12W, DEPTH = 60 METERS
OBSERVATION PERIOD = 0000 20 APR 78 TO 2300 9 MAY 78 (20.0 DAYS)
AVERAGING INTERVAL = 1.0 HOURS (1 POINTS)

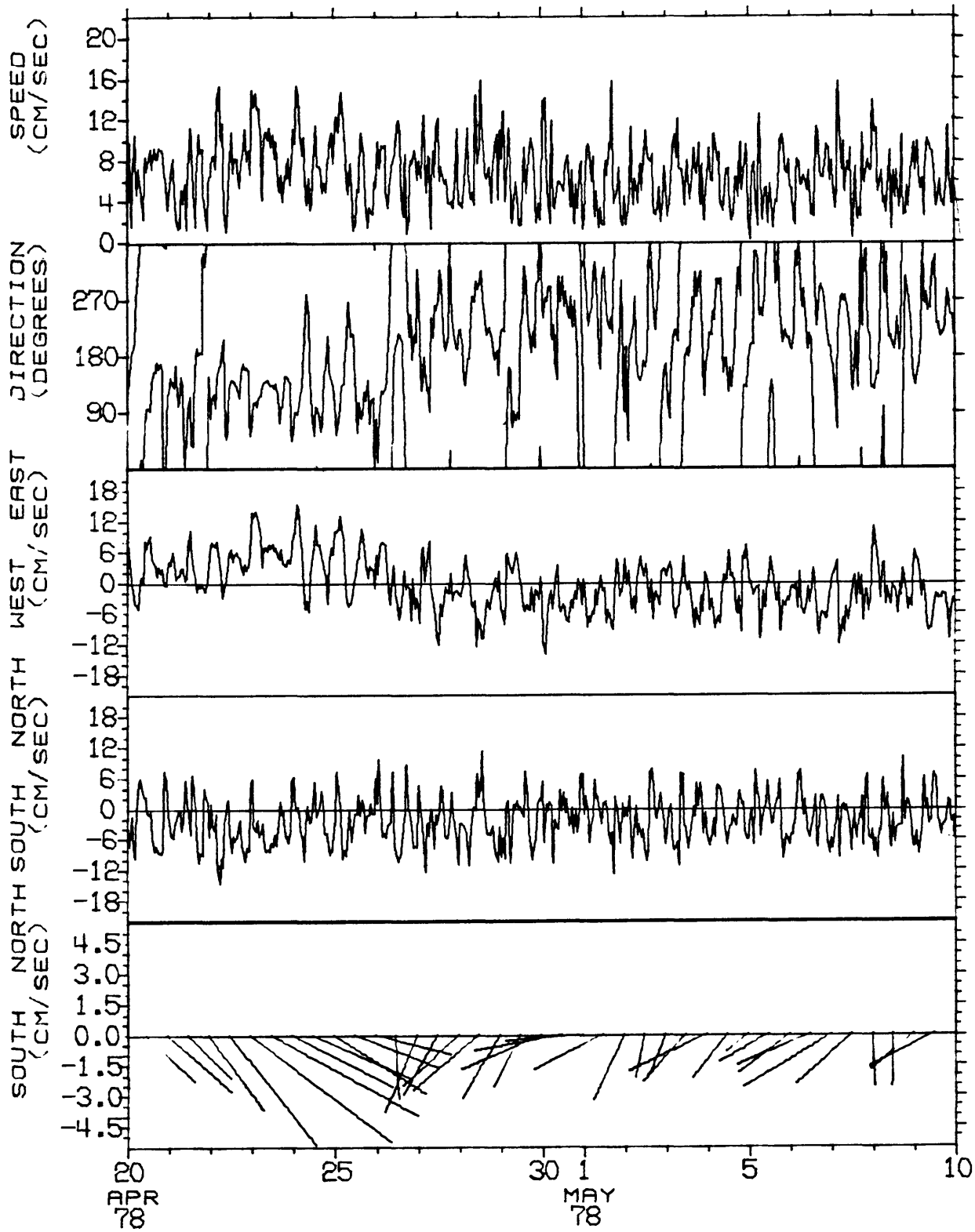

TIME SERIES OF VECTOR AVERAGED CURRENTS AT CM4 - SPEX G2 1978
LOCATION = LAT 33 35N, LONG 118 12W, DEPTH = 60 METERS
OBSERVATION PERIOD = 0000 10 MAY 78 TO 2300 29 MAY 78 (20.0 DAYS)
AVERAGING INTERVAL = 1.0 HOURS (1 POINTS)

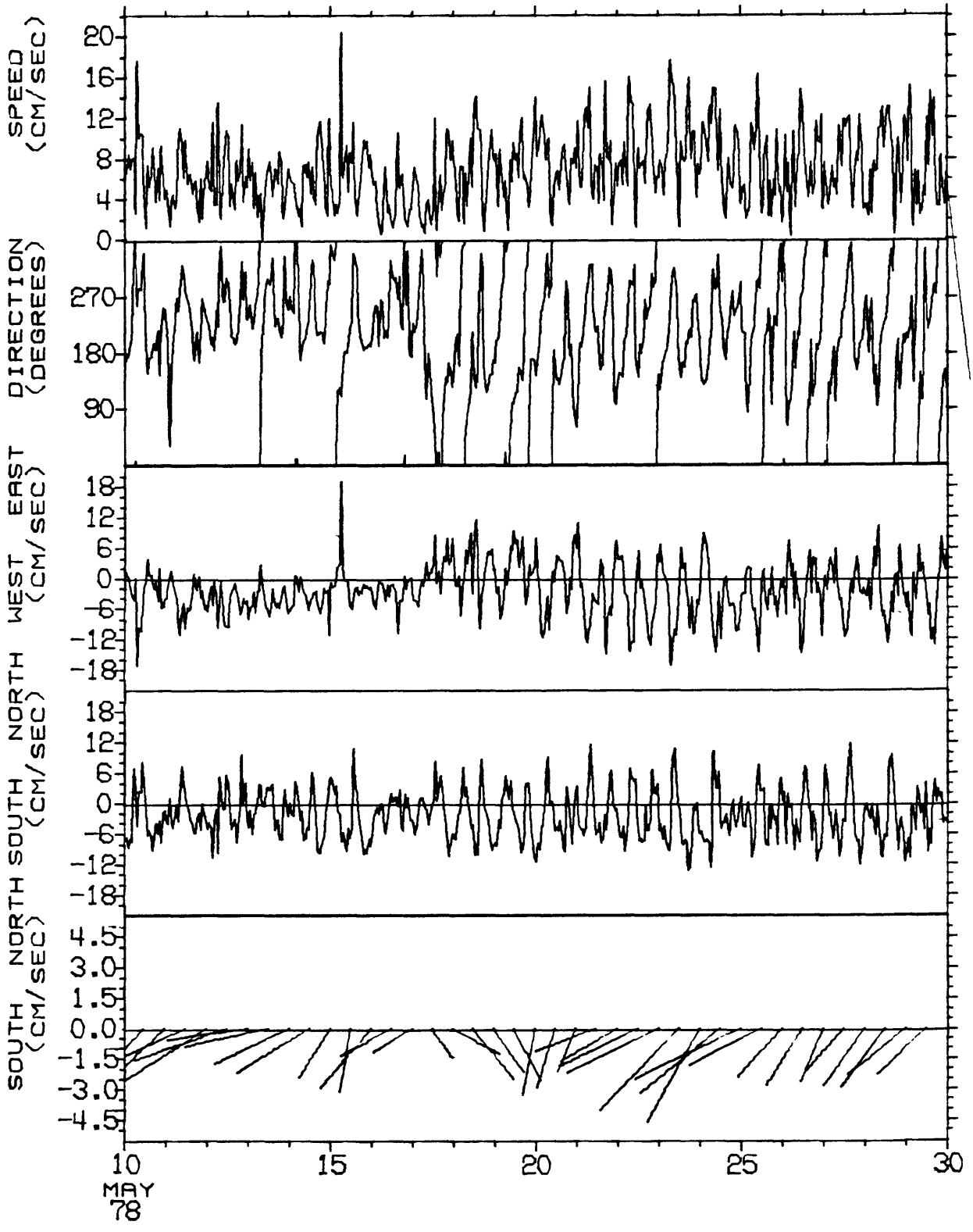

PROGRESSIVE VECTOR DIAGRAM OF CURRENTS AT CM4 - SPEX G2 1978
LOCATION = LAT 33 35N, LONG 118 12W, DEPTH = 60 METERS
OBSERVATION PERIOD = 0000 20 APR 78 TO 2300 29 MAY 78 (40.0 DAYS)
* EVERY 1.0 DAYS BEGINNING AT 0000 20 APR 78

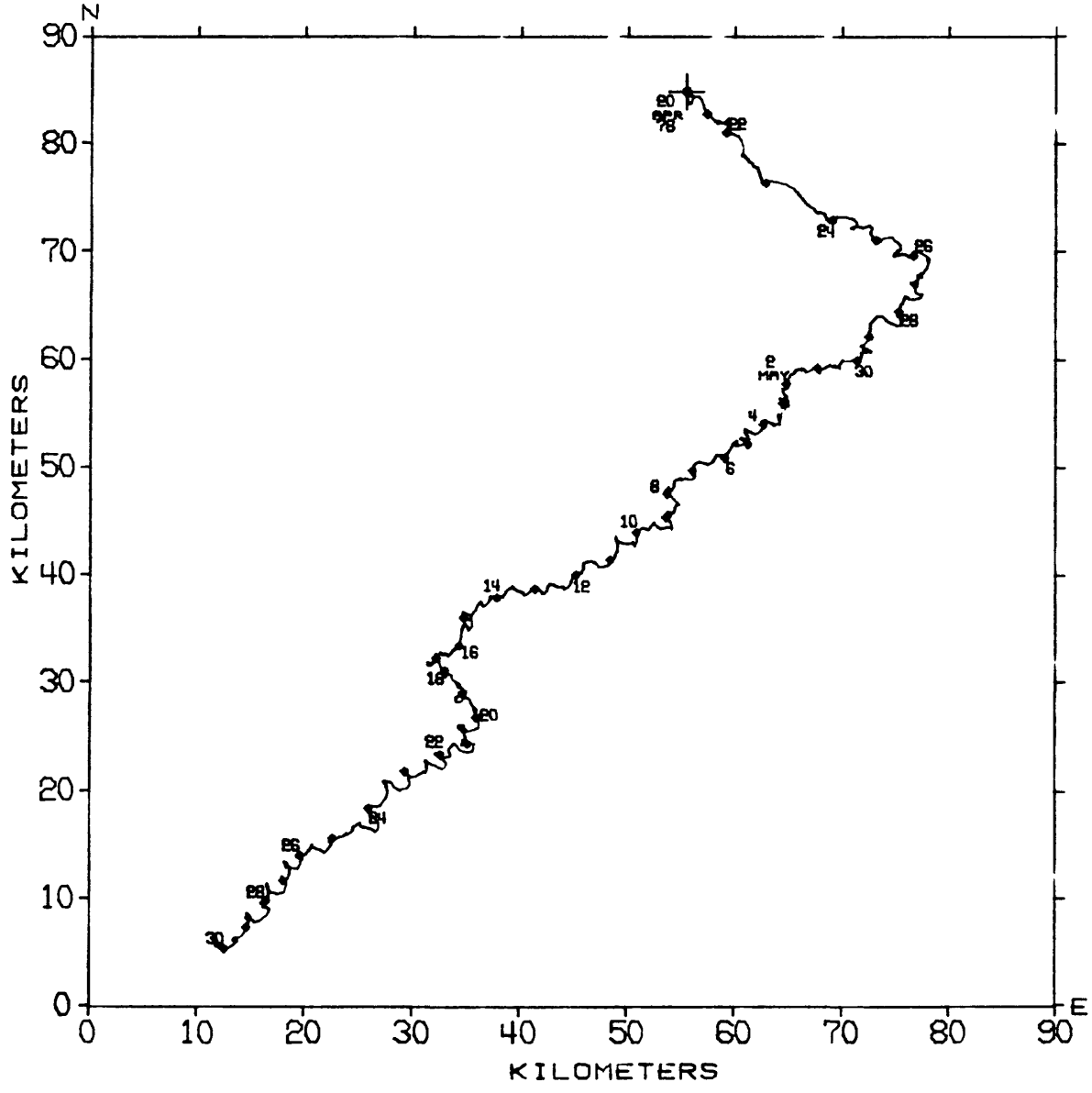

KINETIC ENERGY SPECTRUM OF CURRENTS AT CM4 - SPEX G2 1978
LOCATION = LAT 33 35N, LONG 118 12W, DEPTH = 60 METERS
OBSERVATION PERIOD = 0000 20 APR 78 TO 2300 29 MAY 78 (40.0 DAYS)
N = 960, DT = 1.0 HOURS, SMOOTHING - DANIELL WINDOW

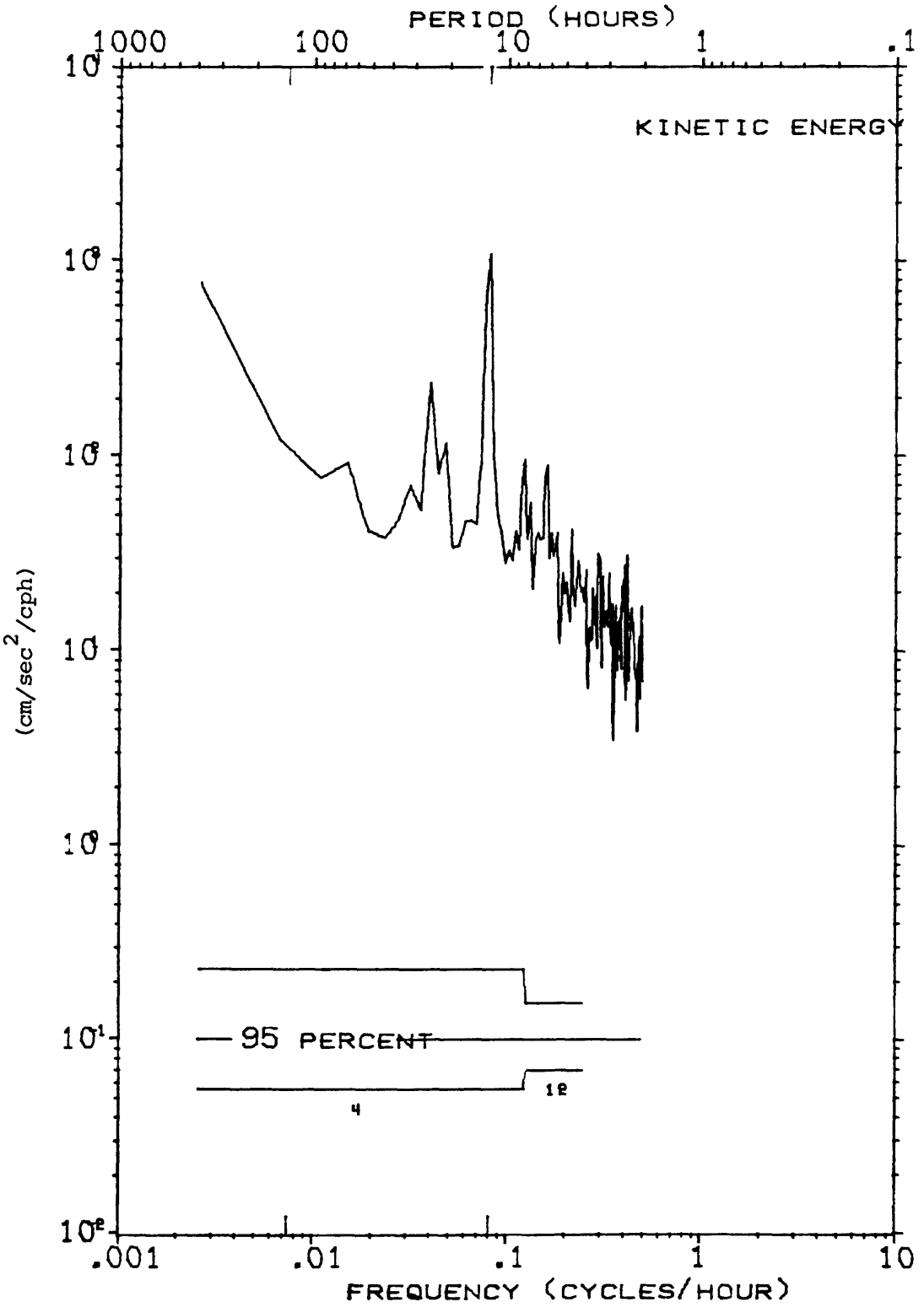

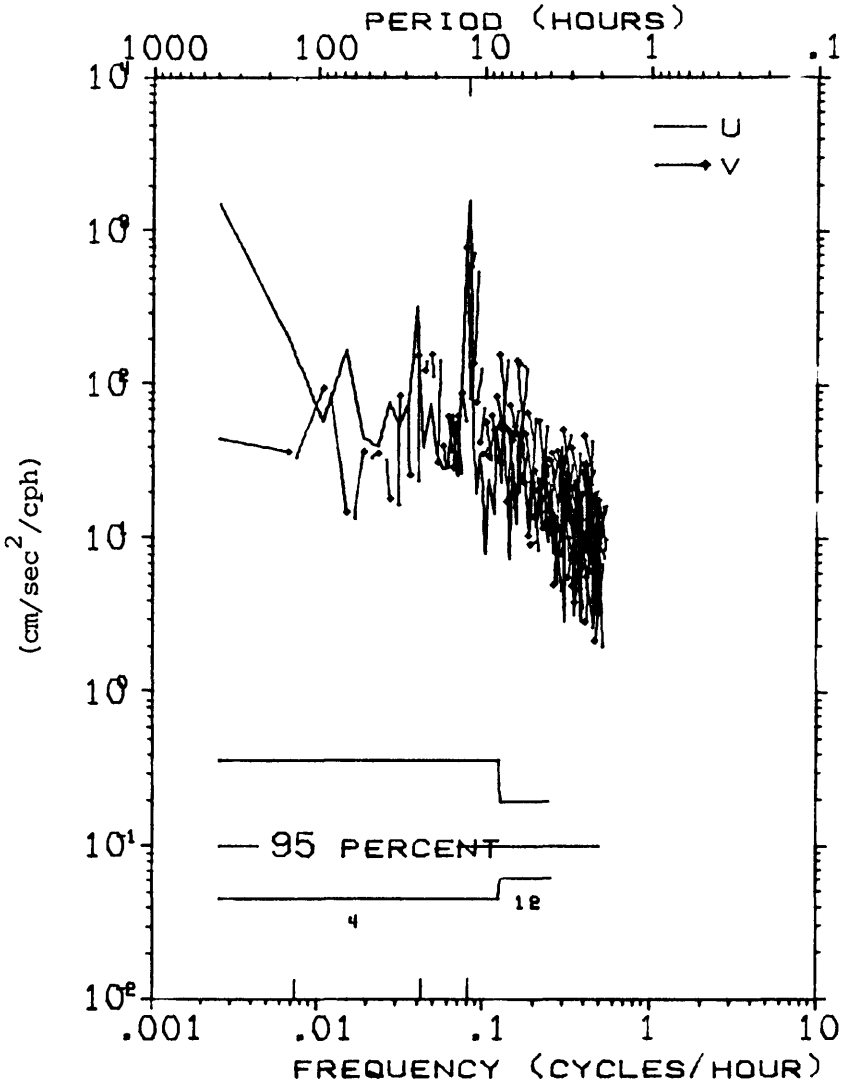

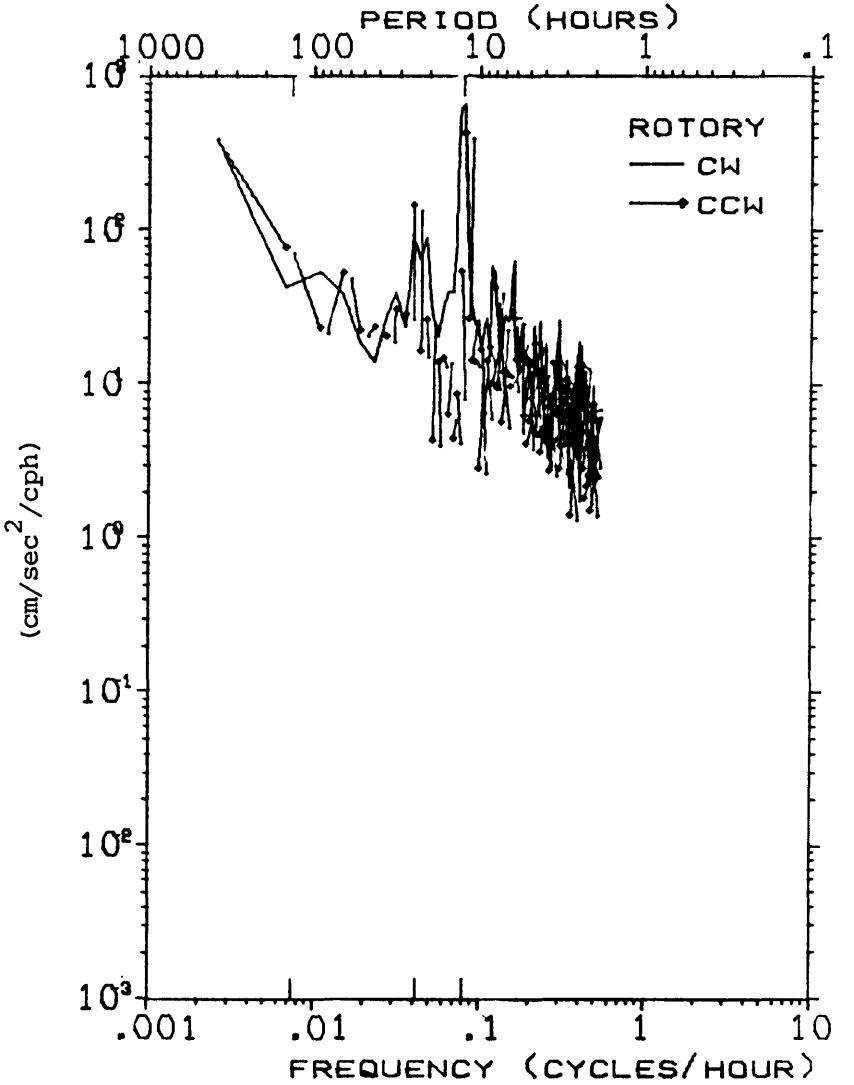

U, V AND ROTORY SPECTRA OF CURRENTS AT CM4 - SPEX G2 1978
LOCATION = LAT 33 35N, LONG 118 12W, DEPTH = 60 METERS
OBSERVATION PERIOD = 0000 20 APR 78 TO 2300 29 MAY 78 (40.0 DAYS)
N = 960, DT = 1.0 HOURS, SMOOTHING - DANIELL WINDOW

STATISTICS AND HISTOGRAMS OF CURRENTS AT CM1 - SPEX G2 1978
LOCATION = LAT 33 35N, LONG 118 12W, DEPTH = 60 METERS
OBSERVATION PERIOD = 0000 20 APR 78 TO 2300 29 MAY 78 (40.0 DAYS)
N = 960 DT = 1.00 HOURS, UNITS = (CM/SEC)

	MEAN	VARIANCE	ST-DEV	SKEW	KURT	MAX	MIN
S	4.90	6.11	2.47	0.577	3.522	16.82	0.00
U	0.16	11.54	3.40	-0.283	4.146	14.74	-13.69
V	-3.14	8.67	2.95	0.061	2.875	6.15	-12.16

S = SPEED
U = EAST-WEST COMPONENT OF VELOCITY, EAST =POSITIVE U
V = NORTH-SOUTH COMPONENT OF VELOCITY, NORTH = POSITIVE V

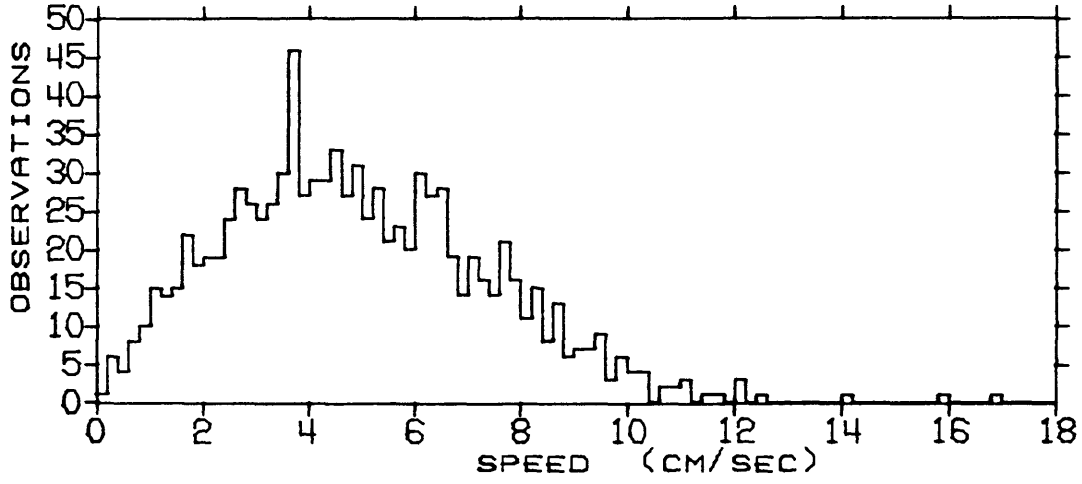

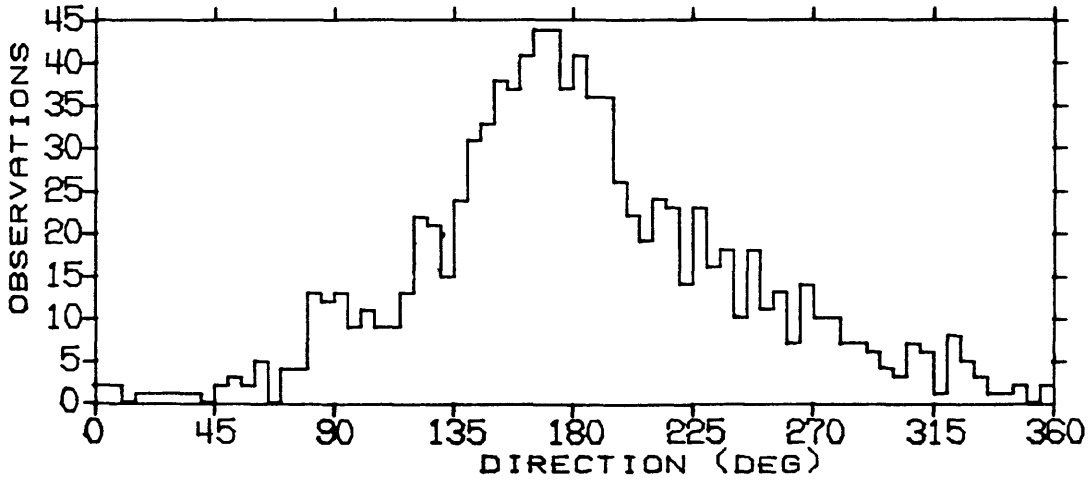

TIME SERIES OF VECTOR AVERAGED CURRENTS AT CM1 - SPEX G2 1978
LOCATION = LAT 33 35N, LONG 118 12W, DEPTH = 60 METERS
OBSERVATION PERIOD = 0000 20 APR 78 TO 2300 9 MAY 78 (20.0 DAYS)
AVERAGING INTERVAL = 1.0 HOURS (1 POINTS)

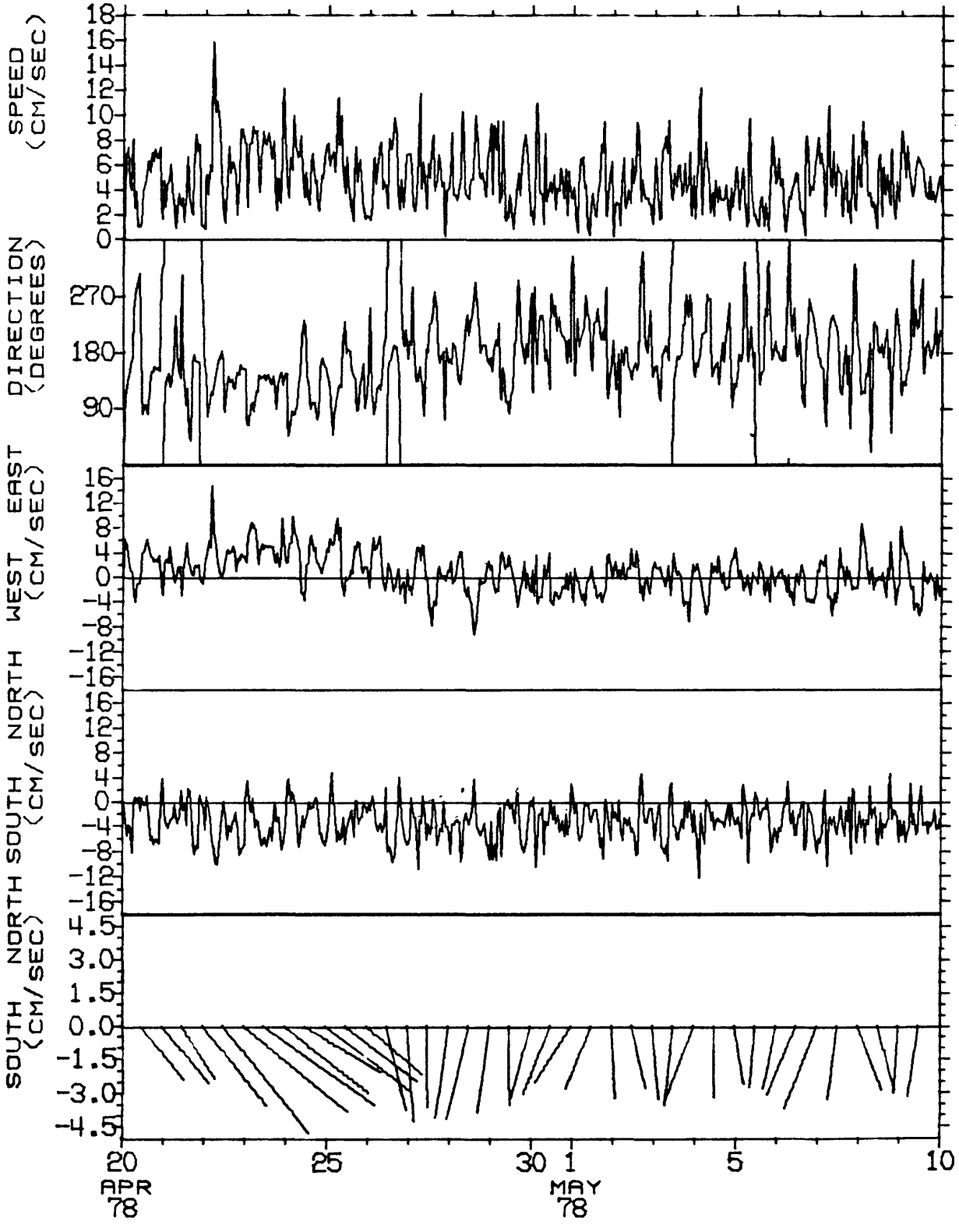

TIME SERIES OF VECTOR AVERAGED CURRENTS AT CM1 - SPEX G2 1978
LOCATION = LAT 33 35N, LONG 118 12W, DEPTH = 60 METERS
OBSERVATION PERIOD = 0000 10 MAY 78 TO 2300 29 MAY 78 (20.0 DAYS)
AVERAGING INTERVAL = 1.0 HOURS (1 POINTS)

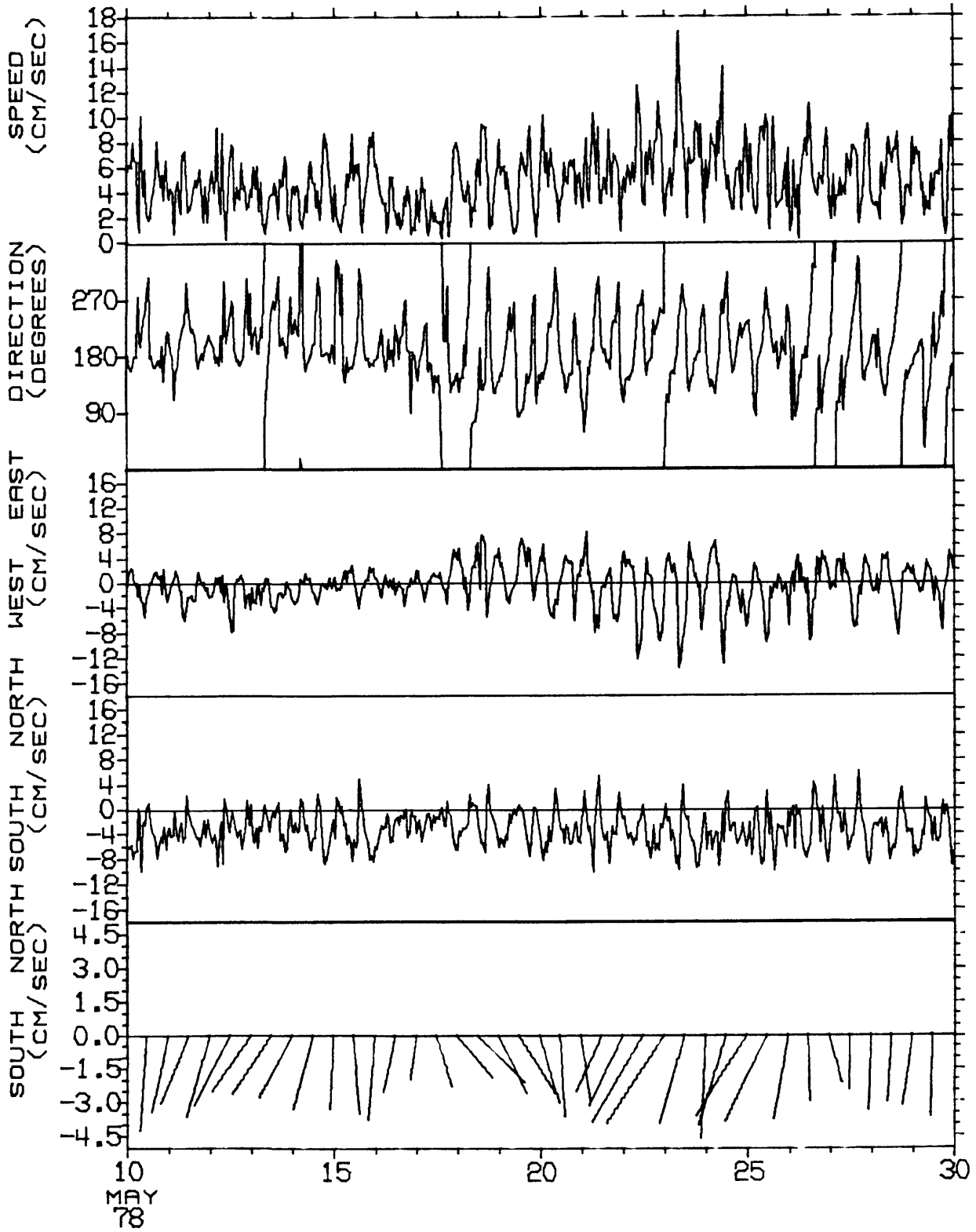

PROGRESSIVE VECTOR DIAGRAM OF CURRENTS AT CM1 - SPEX G2 1978
LOCATION = LAT 33 35N, LONG 118 12W, DEPTH = 60 METERS
OBSERVATION PERIOD = 0000 20 APR 78 TO 2300 29 MAY 78 (40.0 DAYS)
* EVERY 1.0 DAYS BEGINNING AT 0000 20 APR 78

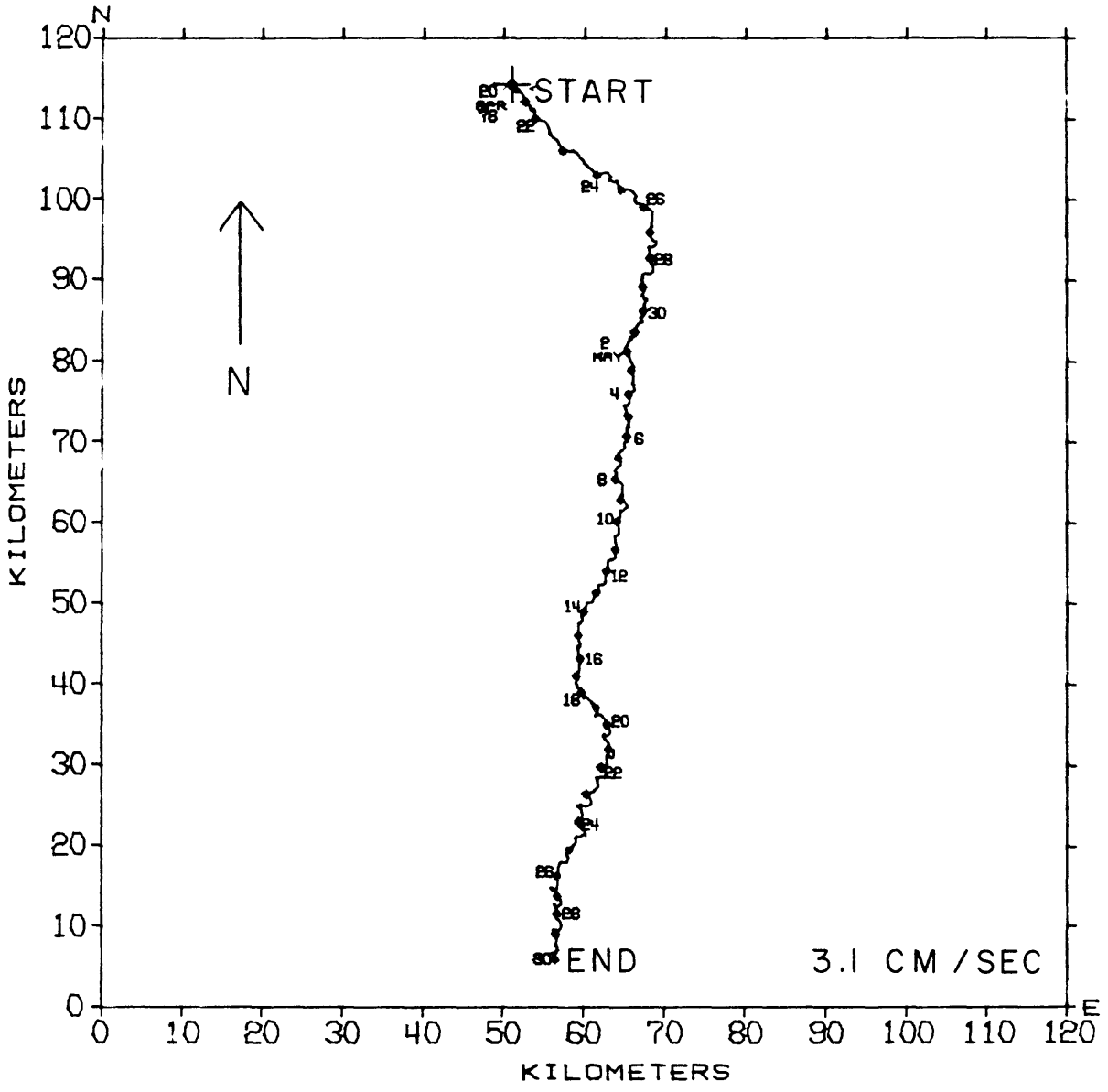

KINETIC ENERGY SPECTRUM OF CURRENTS AT CM1 - SPEX G2 1978
LOCATION = LAT 33 35N, LONG 118 12W, DEPTH = 60 METERS
OBSERVATION PERIOD = 0000 20 APR 78 TO 2300 29 MAY 78 (40.0 DAYS)
N = 960, DT = 1.0 HOURS, SMOOTHING - DANIELL WINDOW

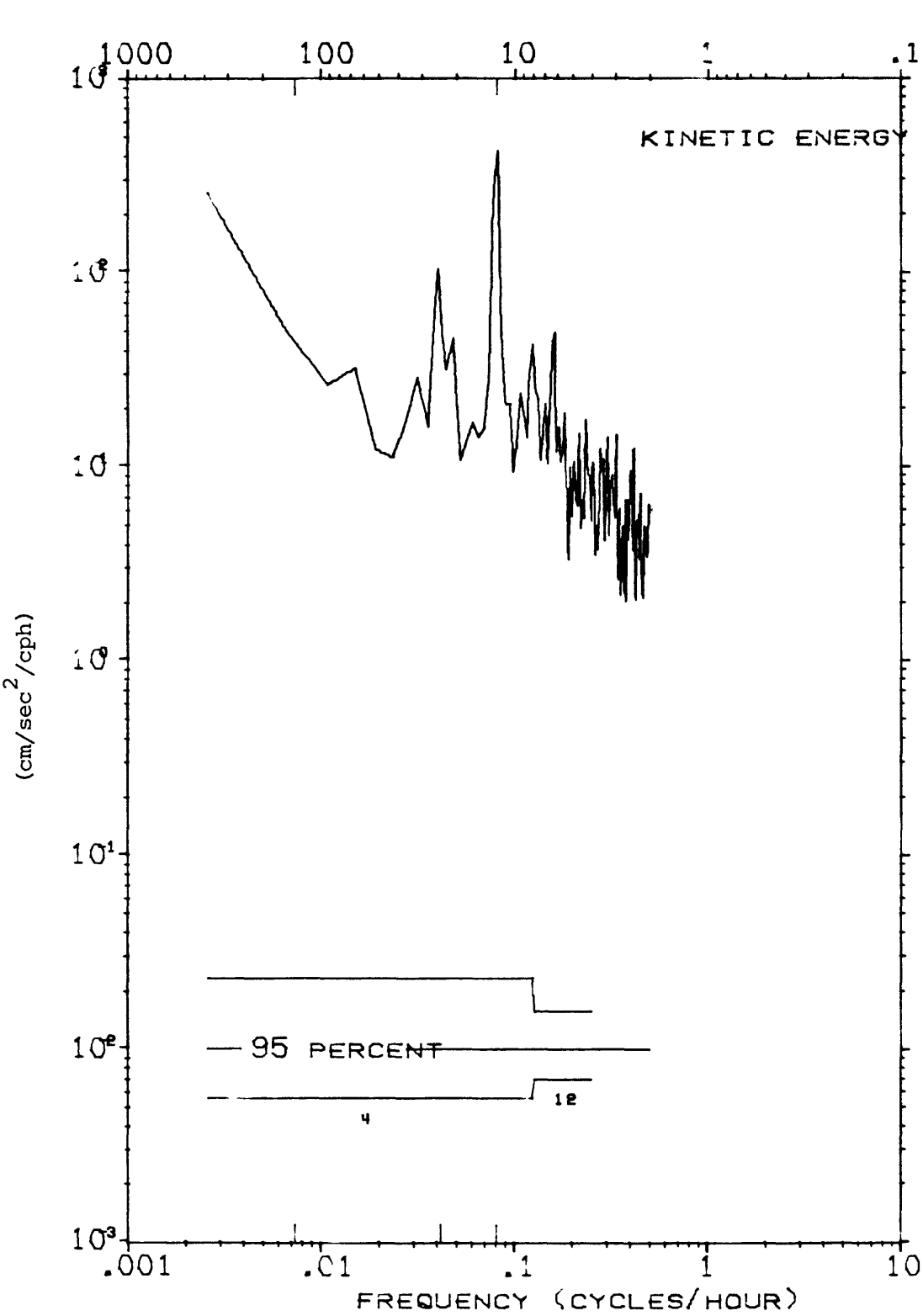

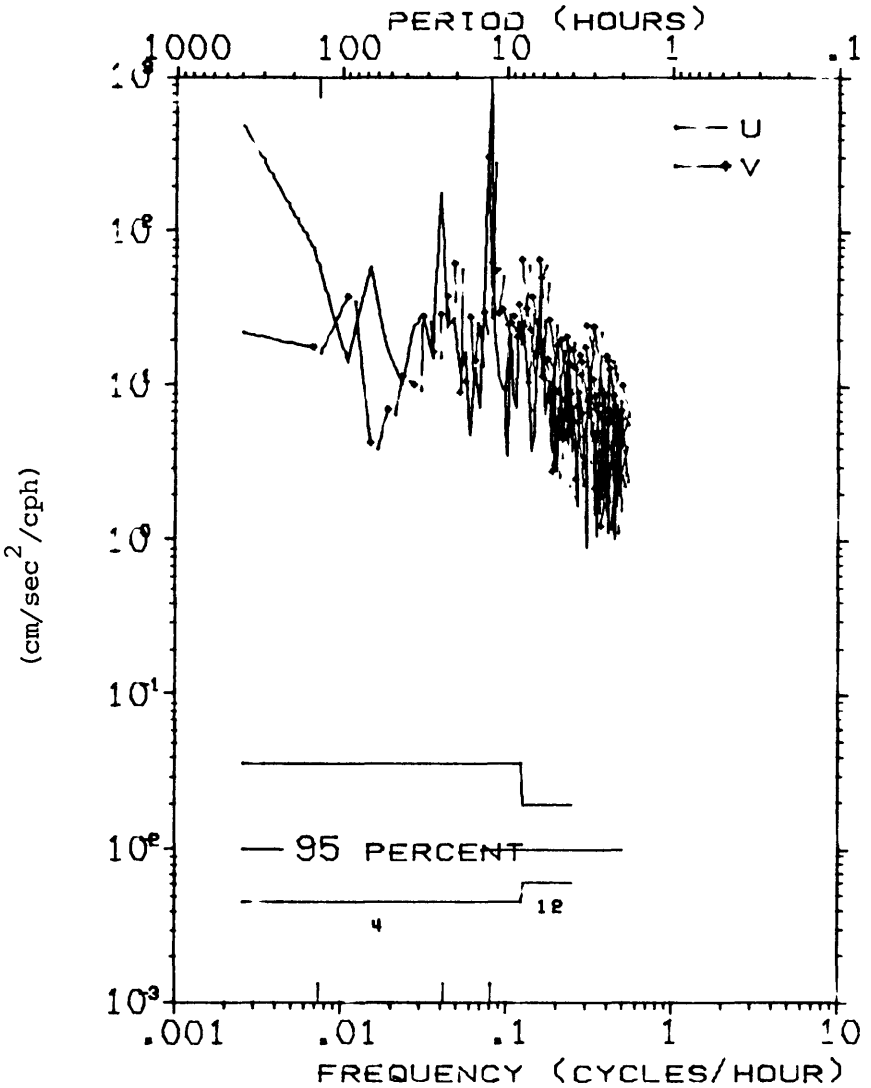

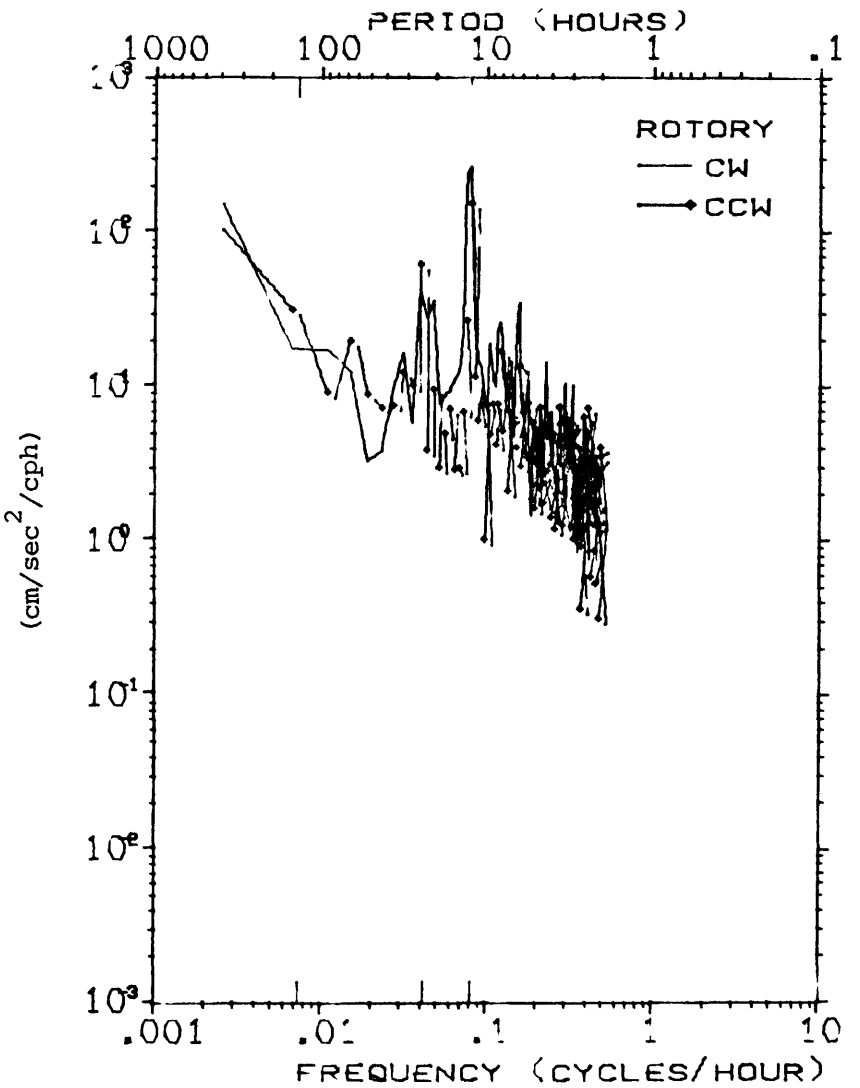

U, V AND ROTORY SPECTRA OF CURRENTS AT CM1 - SPEX G2 1978
LOCATION = LAT 33 35N, LONG 118 12W, DEPTH = 60 METERS
OBSERVATION PERIOD = 0000 20 APR 78 TO\ 2300 29 MAY 78 (40.0 DAYS)
N = 960, DT = 1.0 HOURS, SMOOTHING - DANIELL WINDOW

STATISTICS AND HISTOGRAMS OF CURRENTS AT CM4 - SPEX 1A 1978
LOCATION = LAT 33 40N, LONG 118 12W, DEPTH = 21 METERS
OBSERVATION PERIOD = 1200 17 APR 78 TO 2352 23 APR 78 (6.5 DAYS)
N = 1248. DT = 7.50 MINUTES, UNITS = (CM/SEC)

	MEAN	VARIANCE	ST-DEV	SKEW	KURT	MAX	MIN
S	6.44	12.22	3.50	0.8[illegible]	[illegible]	[illegible]	[illegible]
U	1.66	33.10	5.75	0.3[illegible]	[illegible]	[illegible]	-12.89
V	-0.67	17.40	4.17	0.018	2.582	12.42	-11.91

S = SPEED
U = EAST-WEST COMPONENT OF VELOCITY, EAST =POSITIVE U
V = NORTH-SOUTH COMPONENT OF VELOCITY, NORTH = POSITIVE V

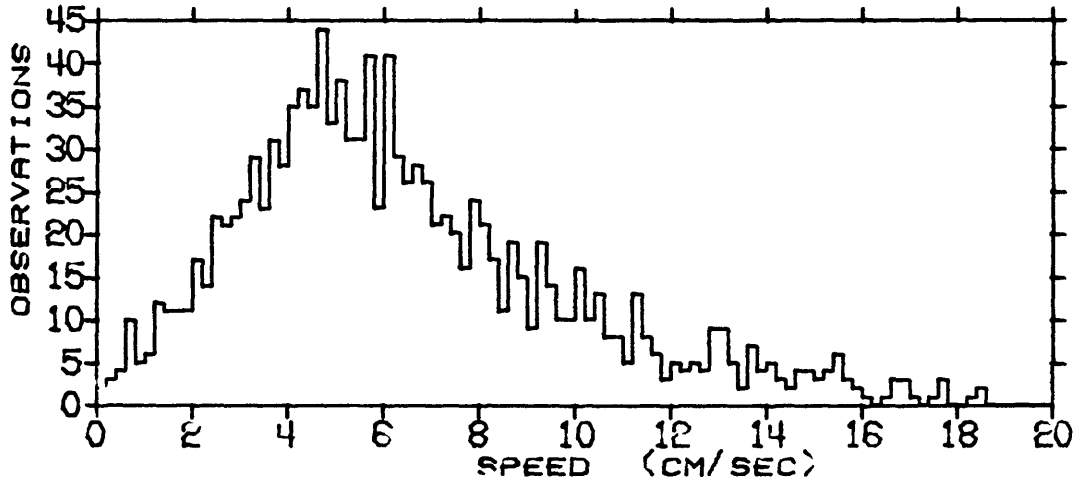

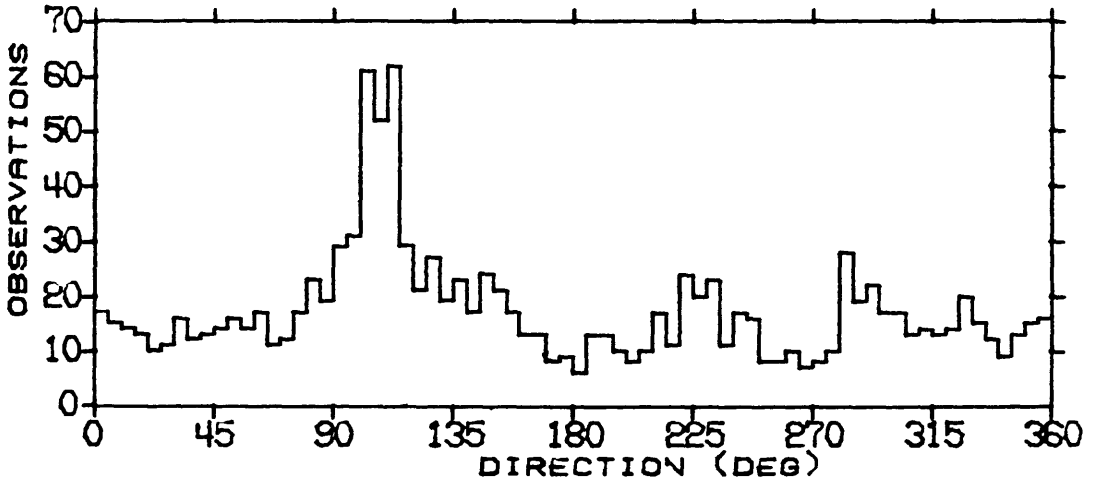

TIME SERIES OF VECTOR AVERAGED CURRENTS AT CM4 - SPEX 19 1978
LOCATION = LAT 33 40N, LONG 118 12W, DEPTH = 21 METERS
OBSERVATION PERIOD = 1200 17 APR 78 TO 2352 23 APR 78 (6.5 DAYS)
AVERAGING INTERVAL = 7.5 MINUTES (1 POINTS)

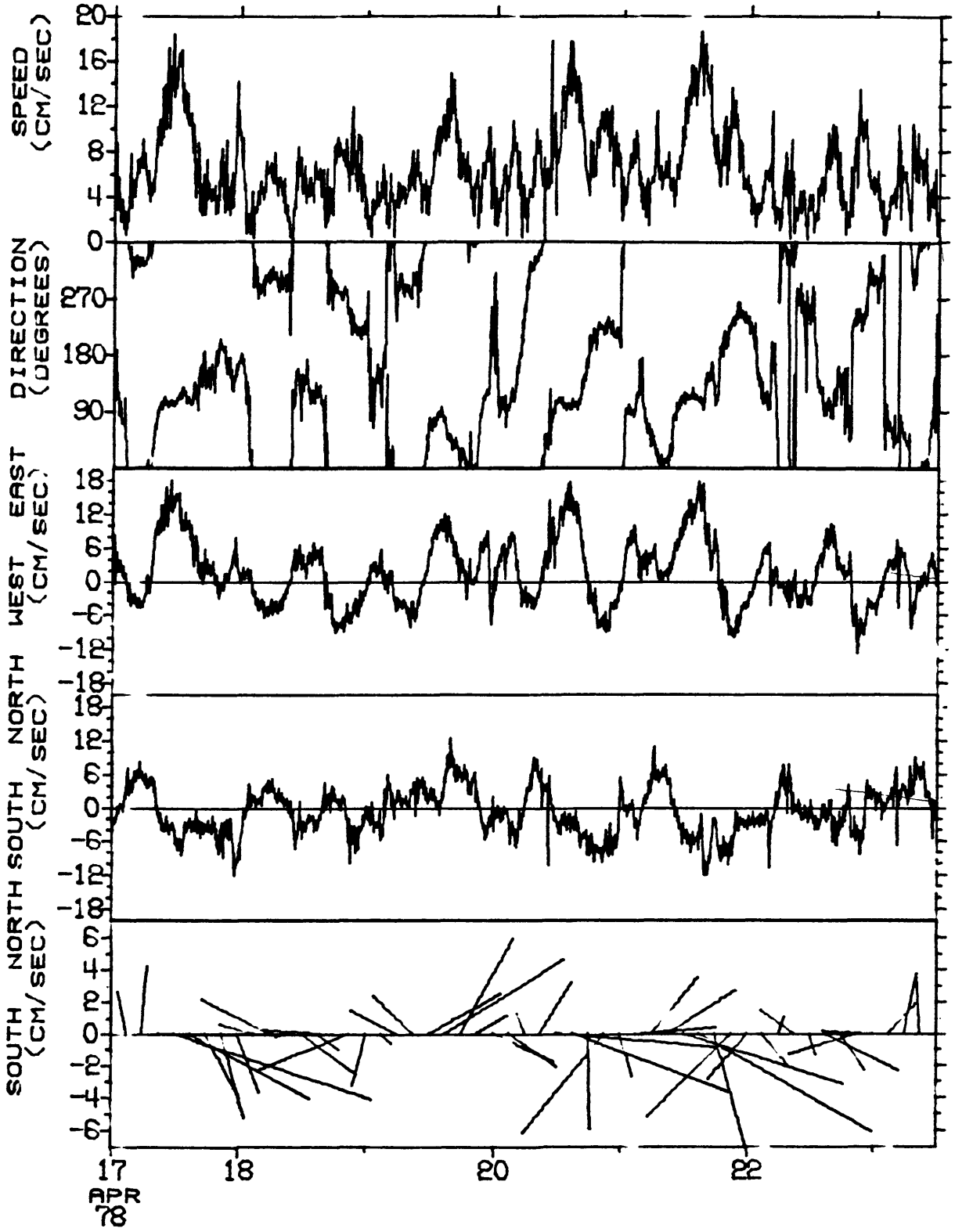

PROGRESSIVE VECTOR DIAGRAM OF CURRENTS AT CM4 - SPEX 1A 1978
LOCATION = LAT 33 40N, LONG 118 12W, DEPTH = 21 METERS
OBSERVATION PERIOD = 1200 17 APR 78 TO 2352 23 APR 78 (6.5 DAYS)
* EVERY 0.3 DAYS BEGINNING AT 0000 18 APR 78

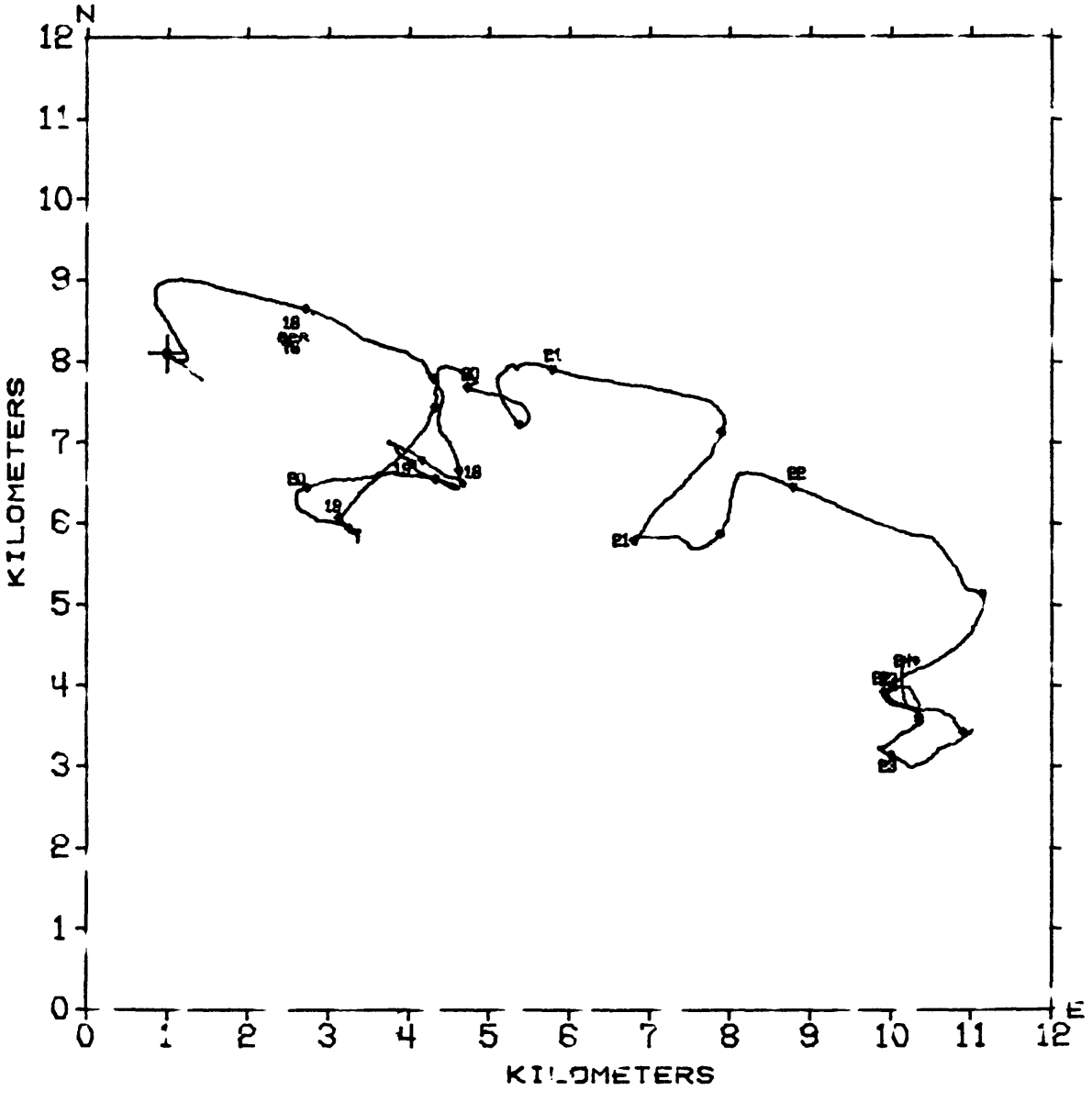

KINETIC ENERGY SPECTRUM OF CURRENTS AT CM4 - SPEX 1A 1978
LOCATION = LAT 33 40N, LONG 118 12W, DEPTH = 21 METERS
OBSERVATION PERIOD = 1200 17 APR 78 TO 2352 23 APR 78 (6.5 DAYS)
N = 1248. DT = 7.50 MINUTES, SMOOTHING - DANIELL WINDOW

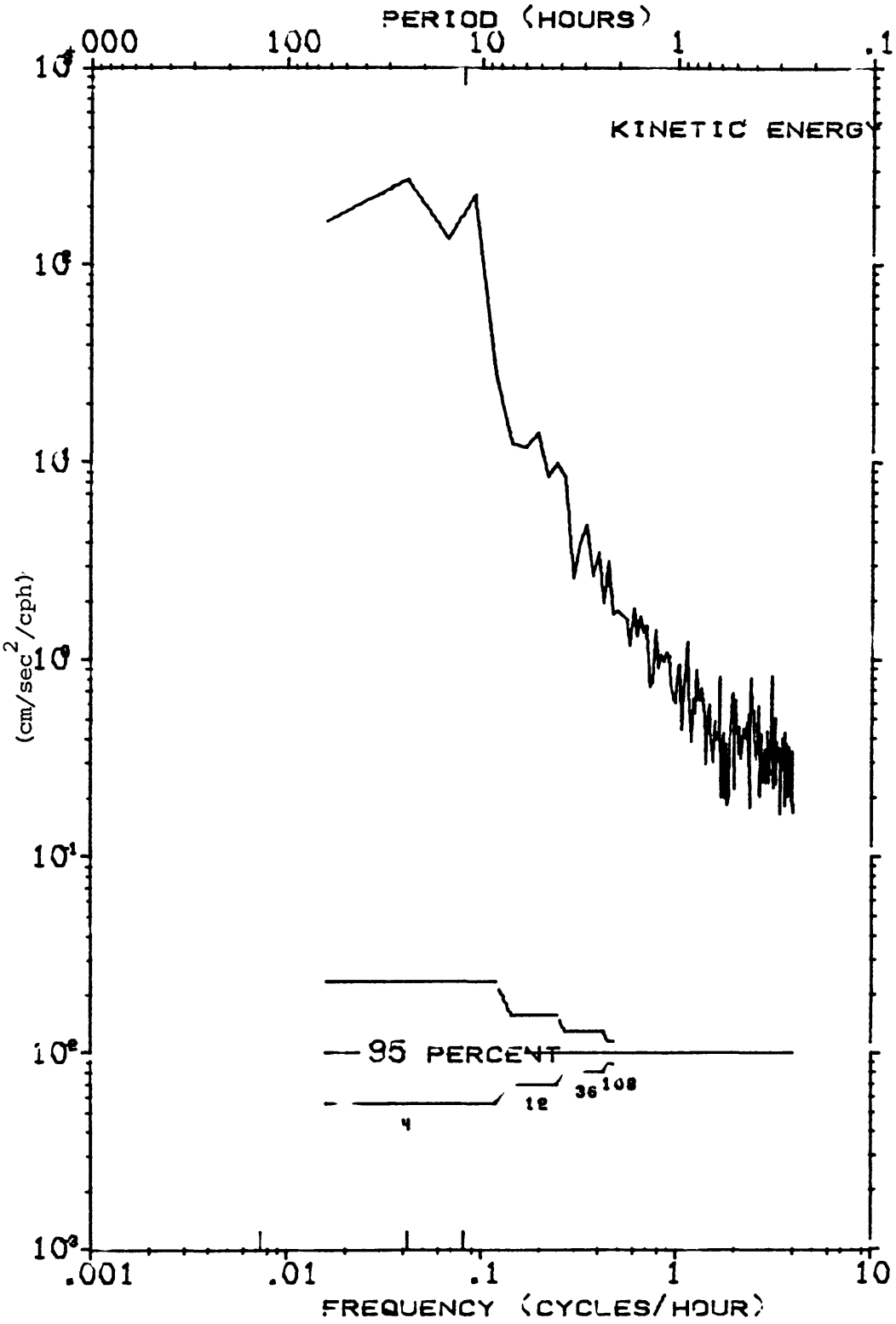

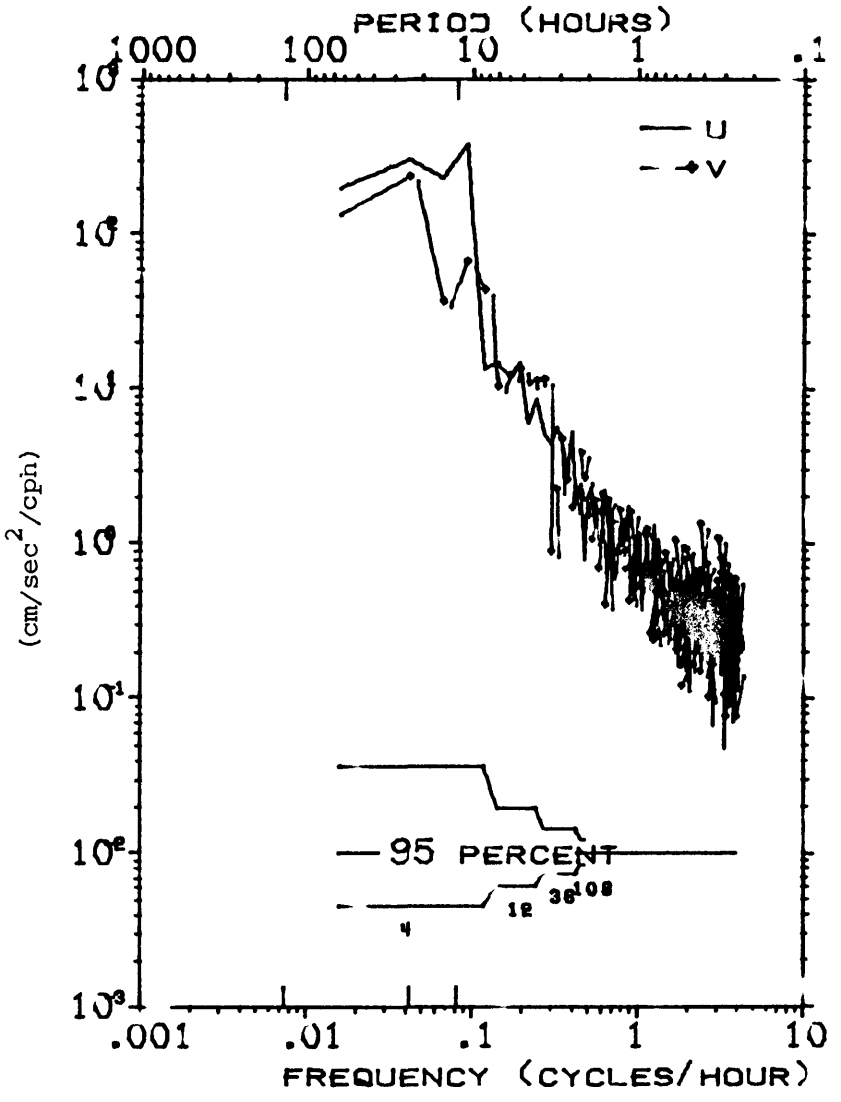

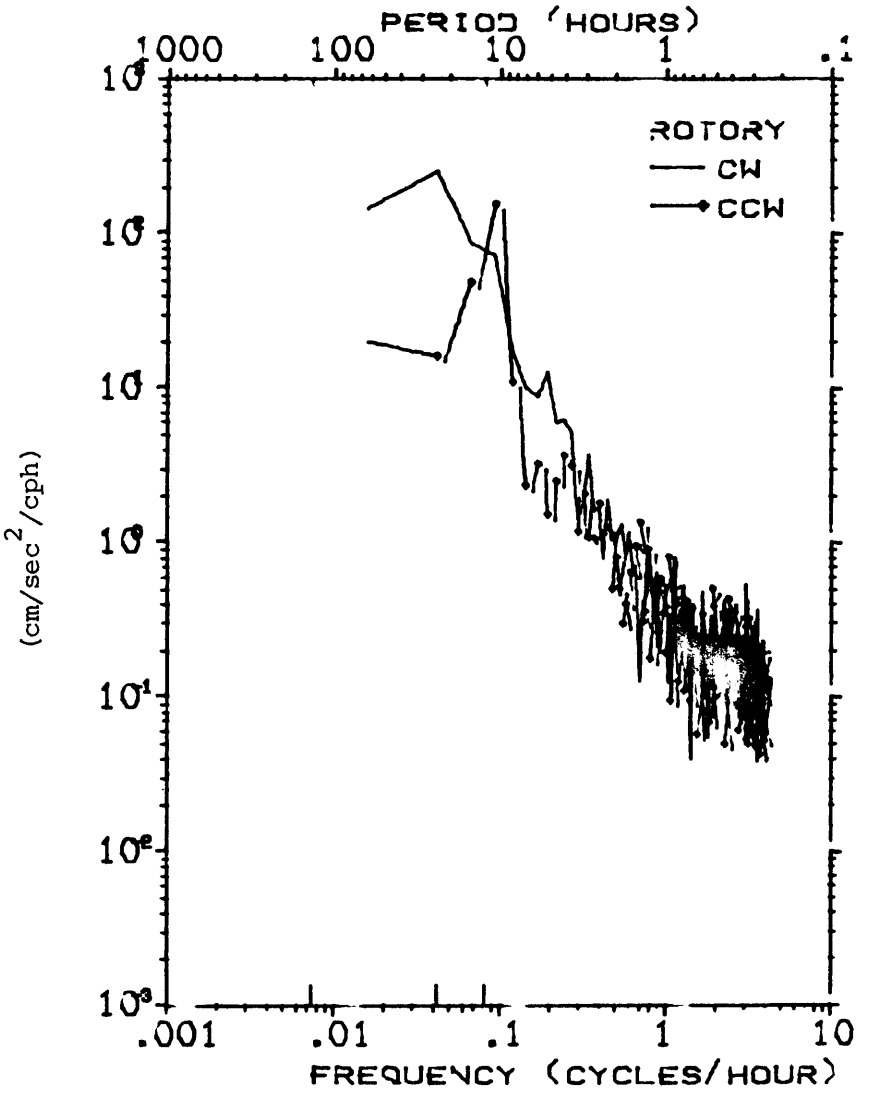

U, V AND ROTORY SPECTRA OF CURRENTS AT CM4 - SPEX 1A 1978
LOCATION = LAT 33 40N, LONG 118 12W, DEPTH = 21 METERS
OBSERVATION PERIOD = 1200 17 APR 78 TO 2352 23 APR 78 (6.5 DAYS)
N = 1248, DT = 7.50 MINUTES, SMOOTHING - DANIELL WINDOW

APPENDIX B

Plots contain "burst" speed data taken with electromagnetic current sensors at 20 cm (CM1), 50 cm (CM2), 70 cm (CM3), and 100 cm (CM4) above seafloor. Pressure data (PRS) is given in meters of water. Note: G1B is the Geoprobe in a mean depth of 24 meters; G2 is in a depth of about 67 meters.

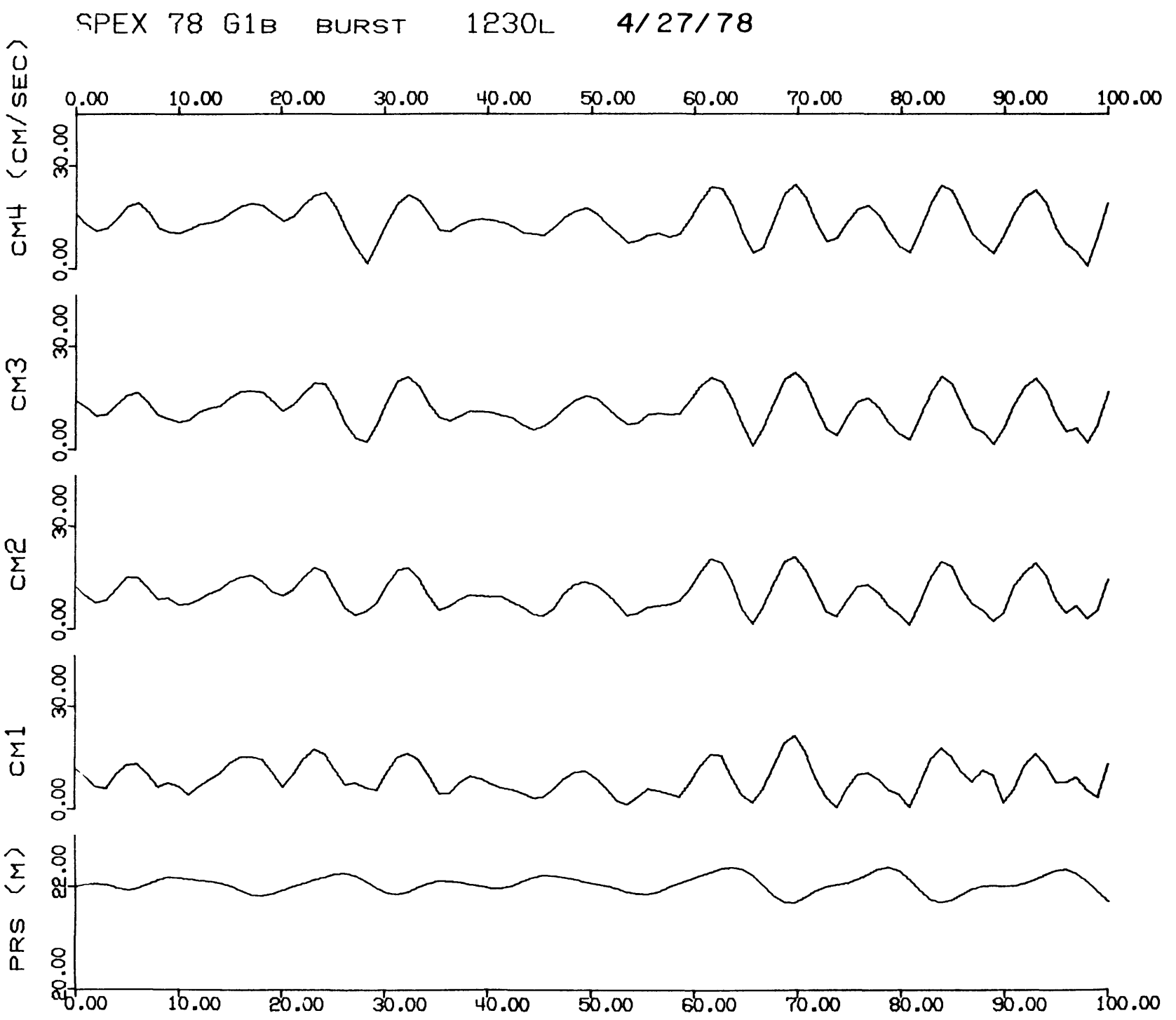
SPEX 78 G1B BURST 1230L 4/27/78
CM4 (CM/SEC)
CM3
CM2
CM1
PRS (M)
0.00
10.00
20.00
30.00
40.00
50.00
60.00
70.00
80.00
90.00
100.00
30.00
0.00
22.00
20.00

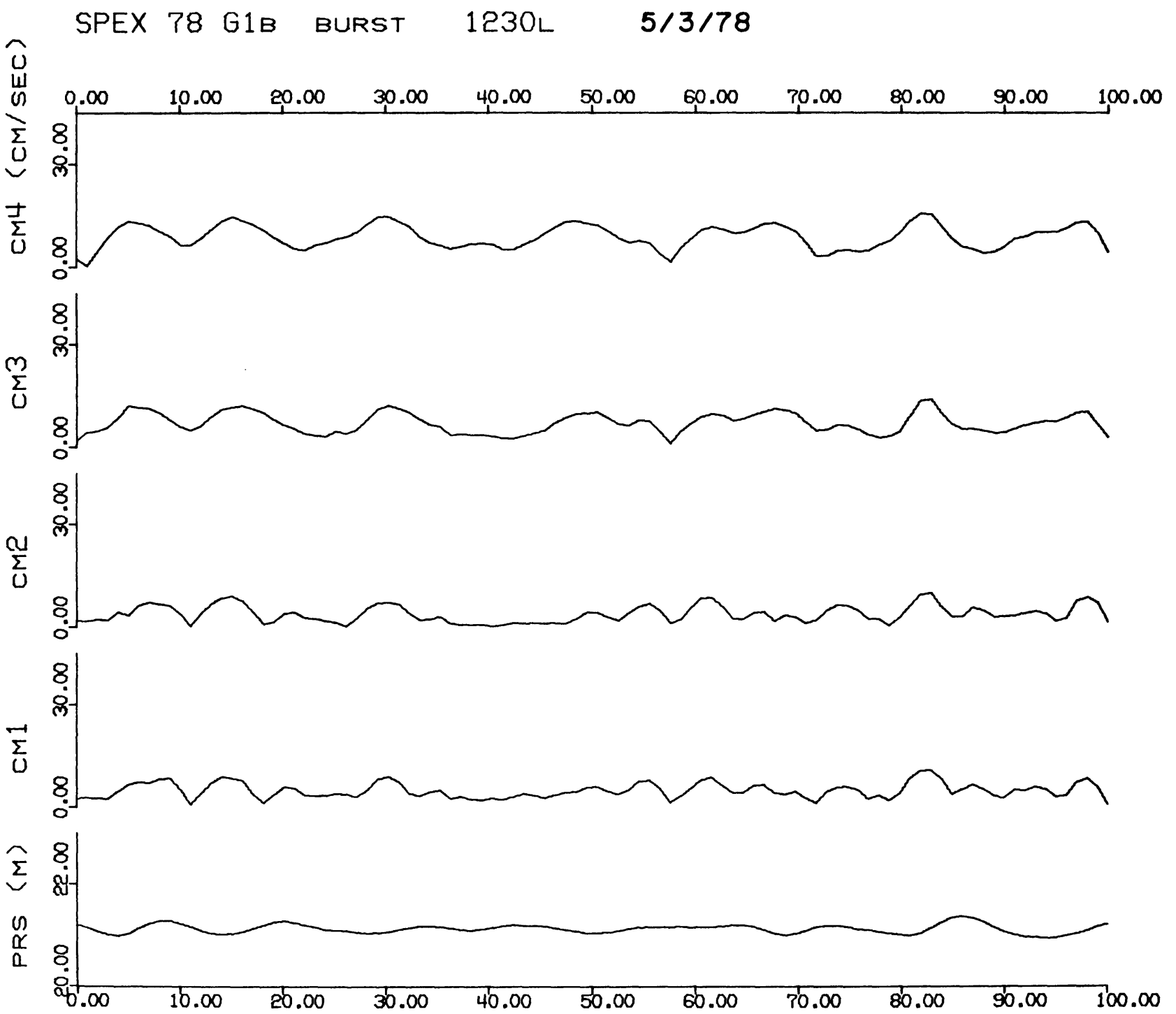
SPEX 78 G1B BURST 1230L 5/3/78
CM4 (CM/SEC)
CM3
CM2
CM1
PRS (M)
0.00
10.00
20.00
30.00
40.00
50.00
60.00
70.00
80.00
90.00
100.00
30.00
0.00
22.00
20.00

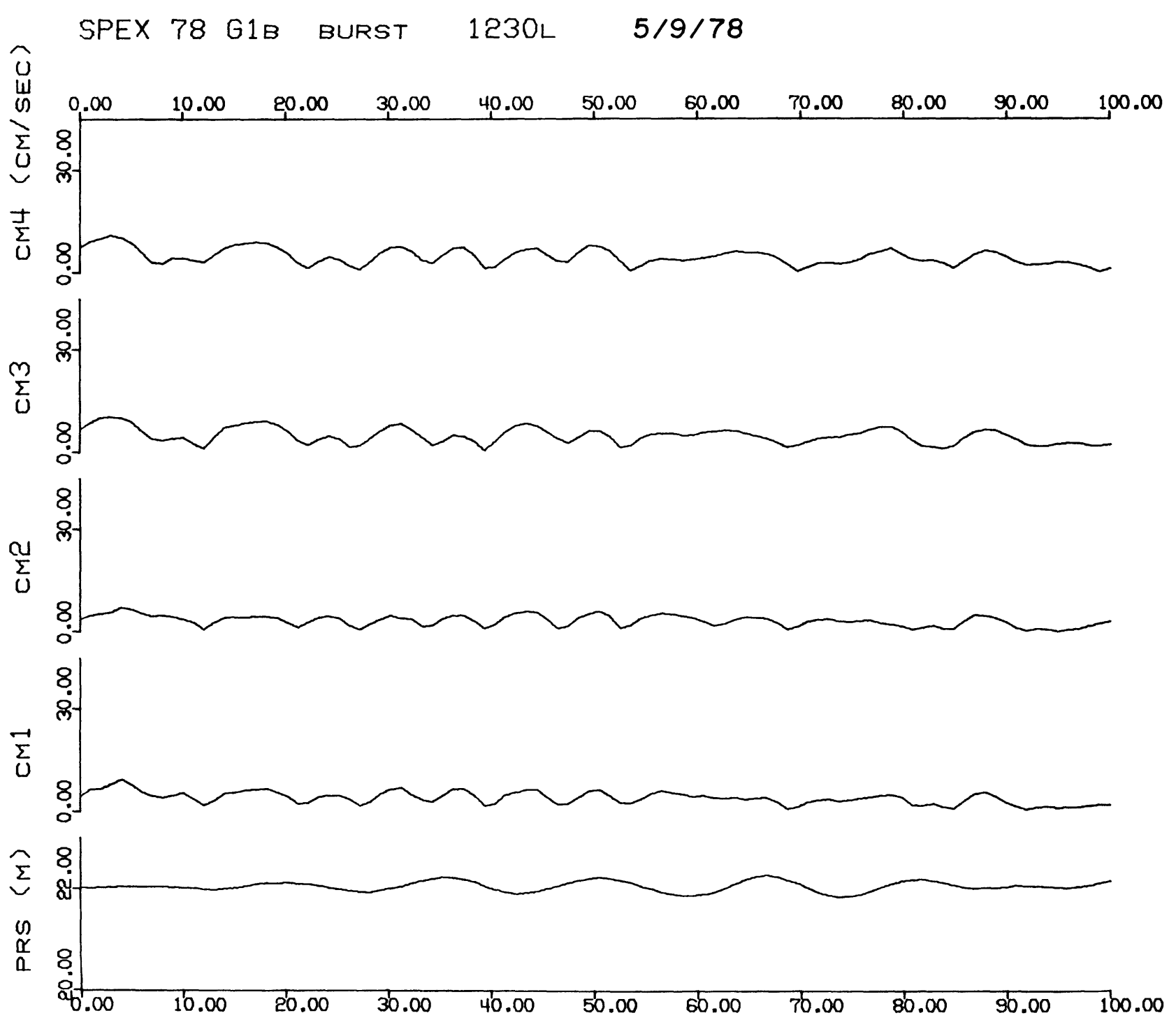
SPEX 78 G1B BURST 1230L 5/9/78
CM4 (CM/SEC)
CM3
CM2
CM1
PRS (M)
0.00
10.00
20.00
30.00
40.00
50.00
60.00
70.00
80.00
90.00
100.00
30.00
0.00
22.00
20.00

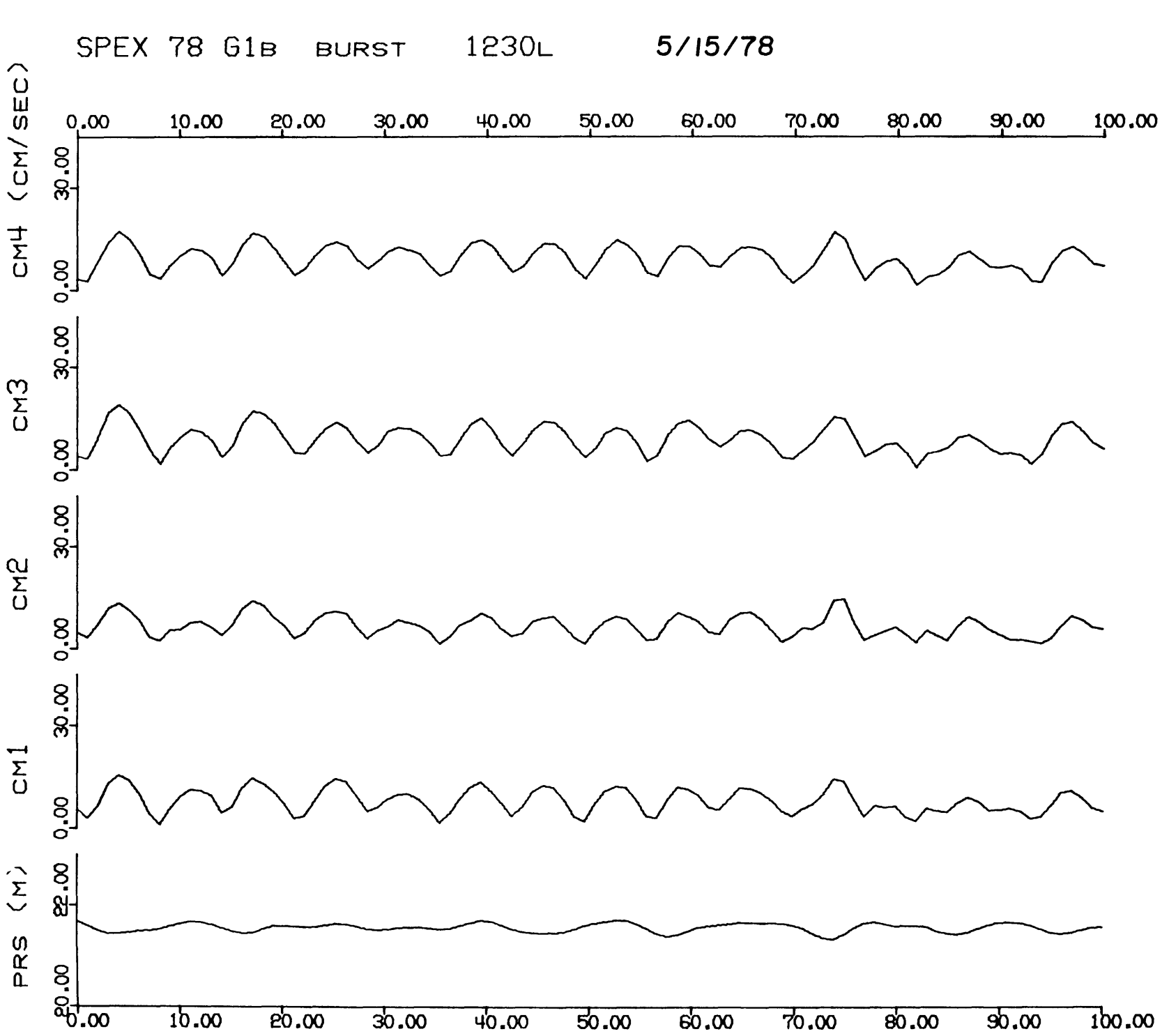
SPEX 78 G1B BURST 1230L 5/15/78
CM4 (CM/SEC)
CM3
CM2
CM1
PRS (M)
0.00
10.00
20.00
30.00
40.00
50.00
60.00
70.00
80.00
90.00
100.00
30.00
0.00
22.00
20.00

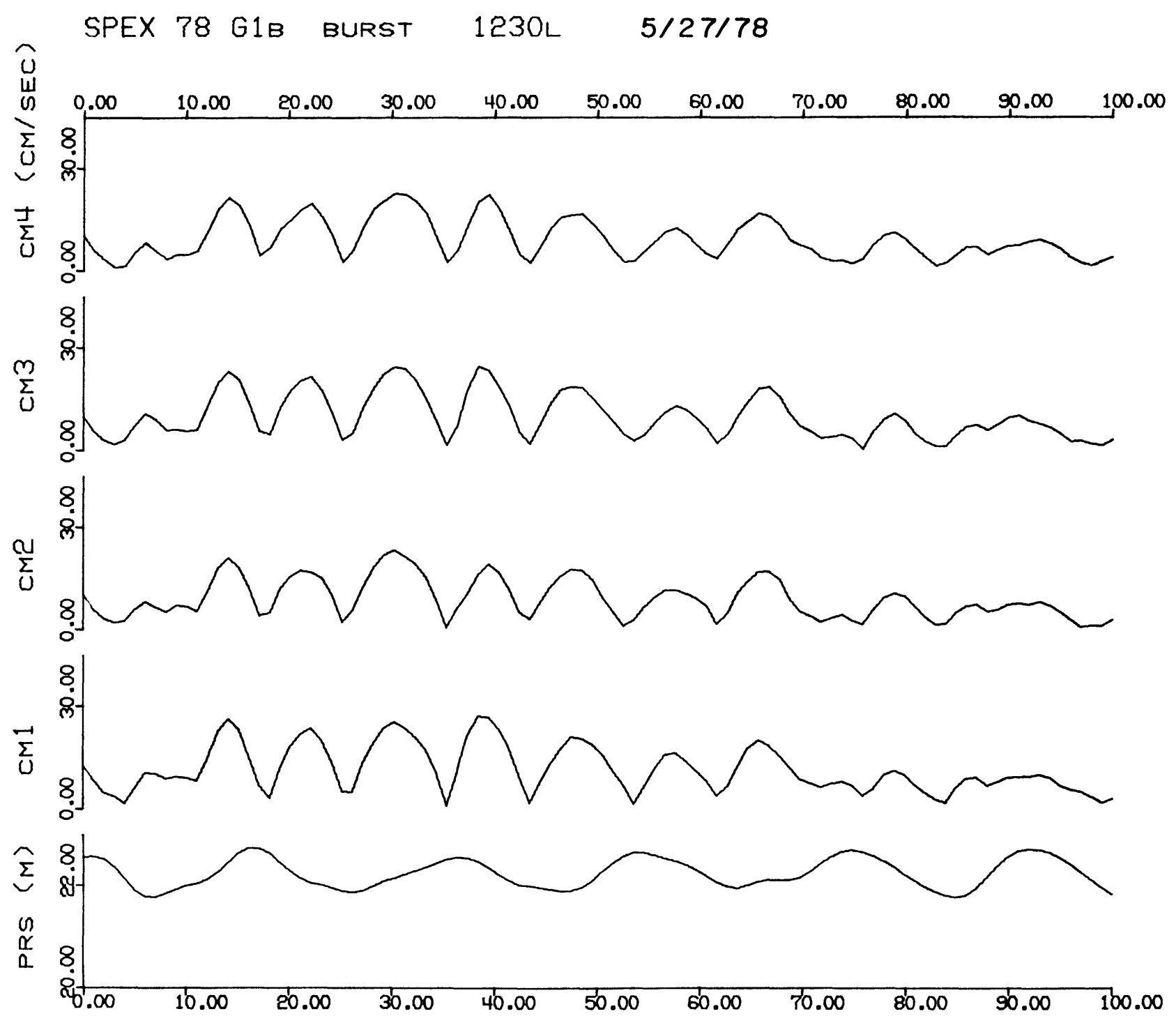
SPEX 78 G1B BURST 1230L 5/27/78
CM4 (CM/SEC)
CM3
CM2
CM1
PRS (M)
0.00
10.00
20.00
30.00
40.00
50.00
60.00
70.00
80.00
90.00
100.00
30.00
0.00
22.00
20.00

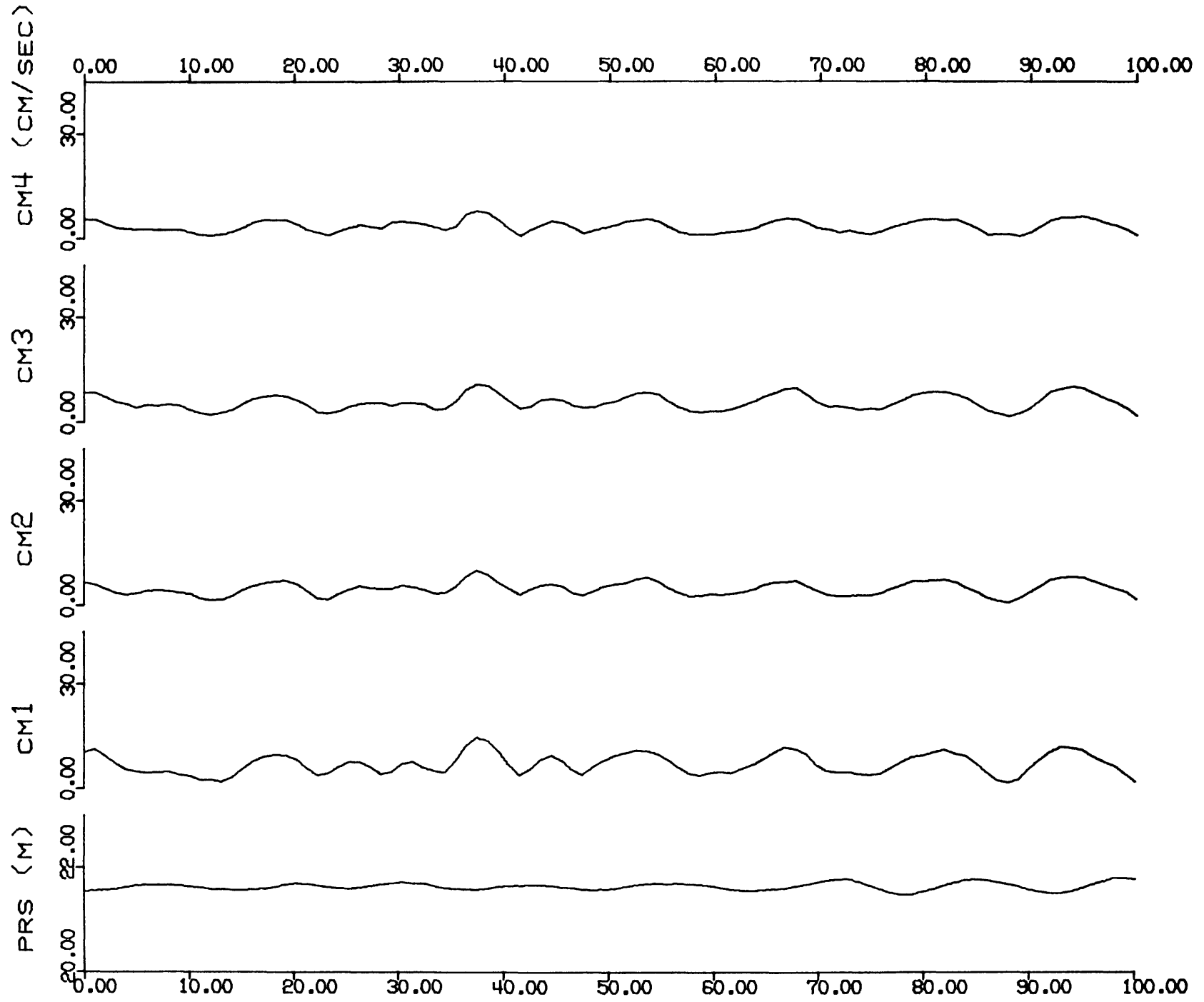
SPEX 78 G1B BURST 1230L 6/2/78
CM4 (CM/SEC)
CM3
CM2
CM1
PRS (M)
0.00
10.00
20.00
30.00
40.00
50.00
60.00
70.00
80.00
90.00
100.00
30.00
0.00
22.00
20.00

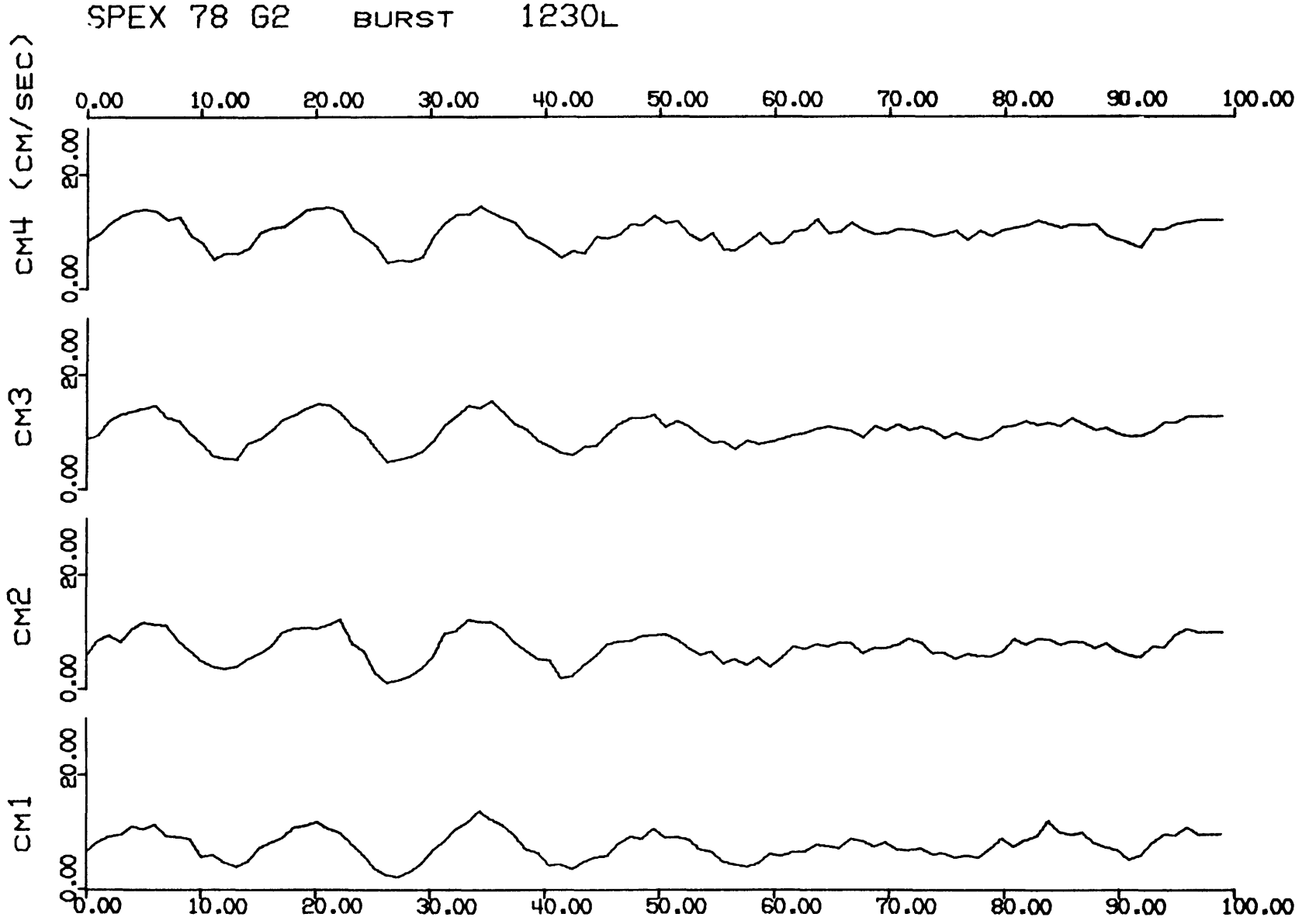
SPEX 78 G2 BURST 1230L
CM4 (CM/SEC)
CM3
CM2
CM1
0.00
10.00
20.00
30.00
40.00
50.00
60.00
70.00
80.00
90.00
100.00
20.00
0.00

4/22/78

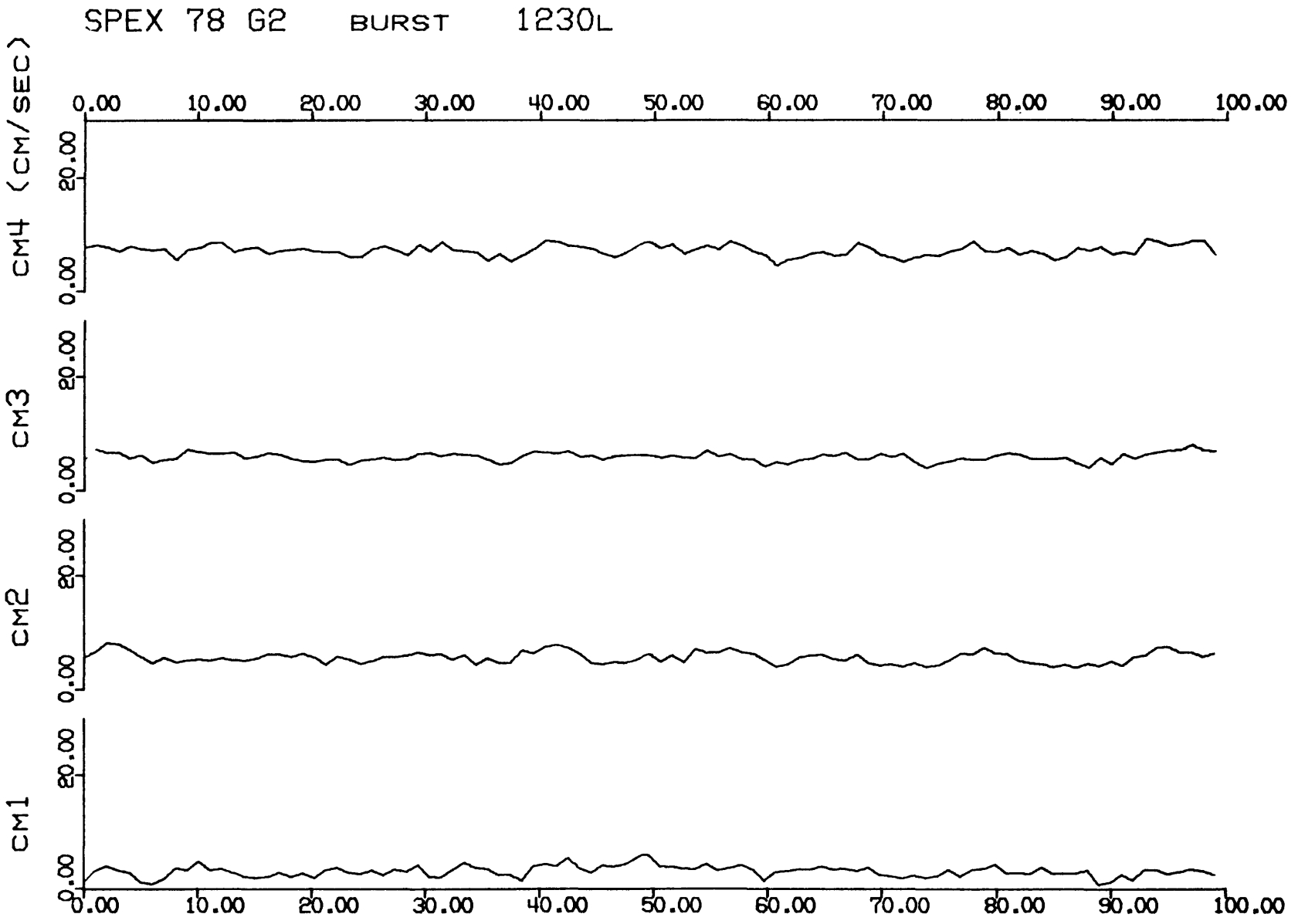
SPEX 78 G2 BURST 1230L
CM4 (CM/SEC)
CM3
CM2
CM1
0.00
10.00
20.00
30.00
40.00
50.00
60.00
70.00
80.00
90.00
100.00
20.00
0.00
4/24/78